Magnetometry of high temperature superconducting micro-disks and single crystals

Connolly, Malcolm

Award date:
2008

Awarding institution:
University of Bath

MAGNETOMETRY OF HIGH TEMPERATURE SUPERCONDUCTING MICRO-DISKS AND SINGLE CRYSTALS

Malcolm Richard Connolly

A thesis submitted for the degree of Doctor of Philosophy

University of Bath

Department of Physics

May 2008

Abstract

Local Hall probe measurements and differential magneto-optical imaging with high spatial resolution have been used to investigate the magnetic state of high temperature superconducting $Bi_2Sr_2CaCu_2O_{8+\delta}$ (BSCCO) micro-disks and platelet single crystals. The results obtained by magneto-optical imaging demonstrate that the field at which flux quantised vortices enter the disks decays exponentially with increasing temperature and the measured data agree well with analytic models for the thermal excitation of individual pancake vortices over Bean-Livingston surface barriers. Scanning Hall probe microscopy images are used to directly map the magnetic induction profiles of individual micro-disks at different applied fields and the results can be quite successfully fitted to analytic models which assume a continuous distribution of flux in the sample. At low fields, however, the characteristic mesoscopic compression of vortex clusters in increasing magnetic fields has been observed. Even at higher fields, where single vortex resolution is lost, it is still possible to track configurational changes in the vortex patterns, since competing vortex orders impose unmistakable signatures on local magnetisation curves as a function of the applied field. These observations are in excellent agreement with molecular dynamics numerical simulations which lead to a natural definition of the lengthscale for the crossover between discrete and continuum behaviours in this system. In closely related experiments, Hall magnetometry is used to probe the out-of-plane local magnetisation of platelet BSCCO single crystals. The magnetisation is found to depend on the strength and direction of an in-plane magnetic field in the crossing vortex lattices regime. The remanent magnetisation in zero out-of-plane field is found to exhibit a pronounced anisotropy, being largest with the in-plane field parallel to the crystalline a-axis, and smallest when it is parallel to the orthogonal b-axis. This behaviour is attributed to the presence of underlying linear disorder. Finally, spectral analysis of the local magnetisation data is used to estimate a lower cutoff for the characteristic frequency of thermal fluctuations of vortex positions.

Acknowledgements

I would like to express my thanks to my supervisor, Prof. Simon Bending, for giving me the opportunity to undertake this research and for his constant support and enthusiasm throughout all its stages.

The BSCCO single crystals investigated in this thesis were provided by Prof. Tsuyoshi Tamegai (The University of Tokyo), who also provided the facilities for performing the magneto-optical imaging work. A number of the problems encountered during the microfabrication work were solved with the help of the technicians from the University of Bath, and I would like to thank Dr Spartaco Landi, Wendy Lambson, and Bob Draper in particular for their assistance. Further thanks go to Dr Frederica Causa and Lu-min Tsei (University of Bath) for providing access to the Argon ion beam miller, to Peter Sykes for frequently giving good advice on high frequency electronics, and to Dr Steve Davies and the TeraHertz Group for lending their spectrum analyser.

Prof. John R. Clem (Iowa State University) provided valuable insight into the underlying physics of our system and Dr Milorad Milosevic (University of Bath) was largely responsible for developing the theoretical molecular dynamics simulations used to gain a deeper insight into the experimental images. My thanks go to the members of the Nanosciences Group, particularly John Neal, Nick Lambert, and Miles Engbarth for many useful discussions.

My family have been tremendous and I cannot thank them enough for all their support and encouragement.

Contents

Chapter 1

Overview

1.1 Motivation

One of the defining features of a type II superconductor in a magnetic field is the complete expulsion of magnetic flux up to the lower critical field, H_{c1}. Above this field the perfect diamagnetism is partially destroyed by the flux enclosed by mutually repelling microscopic vortices, which nucleate at the sample edges and penetrate to the centre where they form a triangular lattice structure. It is now well established that the applied field and temperature conditions which drive a superconductor from the perfectly diamagnetic to the vortex state depend strongly on its size and shape. A particularly rich source of information relating to the influence of these two factors has been obtained from thin platelets and micro-disks, i.e., disks with micron sized diameters, especially those made from high temperature (high-T_c) superconductors [1, 2, 3, 4, 5, 6]. High-T_c materials are excellent candidates for studying the influence of shape and surfaces due to their low levels of disorder and high operating temperatures ($T_c \approx 90$ K), both of which combine to ensure that the transition to the vortex state is less affected by bulk disorder.

In comparison to "bulk" samples, whose properties are generally *not* dominated by their free surfaces, platelets and micro-disks have been found to exhibit unexpected, or at least not completely understood, behaviours in a magnetic field [7, 8]. In millimetre sized platelets with thicknesses of the order of ten microns,

for instance, the applied field at the transition to the vortex state, H_p, is found to be considerably lower than H_{c1}; at intermediate temperatures H_p exhibits an exponential rather than parabolic decay with increasing temperature [9, 10]; and the magnetisation exhibits hysteresis, i.e., its value depends on whether the field is increasing or decreasing, even at temperatures close to T_c. The origins of these unique features have long been questioned. It is now generally recognised that the large enhancement of the fields at the edge of samples with aspect ratios is responsible for the transition occuring in weak applied fields. However, neither the measured temperature dependence nor the absolute value of H_p, upon correction for this enhancement, correspond to that of H_{c1} [9], so platelets continue to receive a great deal of attention.

The scientific interest associated with superconducting micro-disks, on the other hand, stems more from the strong interaction between the nucleating vortices and the surfaces *after* the transition to the vortex state. Both simulations [11] and magnetic imaging techniques [12, 13, 14] have shown, for instance, that at low fields, when there are only a few vortices in the disk, vortex clusters, or regular polygons with one vortex at each vertex, are formed. As more vortices enter the disk, they start to form concentric shell structures with each new shell forming at critical or "magic" numbers of vortices. However, it is still unclear how this behaviour, which is typically associated with mesoscopic superconductors, is replaced by continuum behaviour as the size of the disk approaches macroscopic dimensions, where the sheer density of vortices lessens the importance of each individual one.

It is the primary objective of this thesis to address these and other questions surrounding the penetration and distribution of vortices. This objective is accomplished by means of evidence obtained using high spatial resolution scanning Hall probe microscopy (SHPM) and magneto-optical imaging (MOI) to observe the stray diamagnetic and vortex fields at the surface of arrays of high temperature superconducting $Bi_2Sr_2CaCu_2O_{8+\delta}$ (BSCCO) micro-disks and platelet single crystals.

1.2 Structure

The thesis is structured in the following way. The basic electromagnetic and thermodynamic phenomenology of superconductivity is described in chapter (2). The key concept presented in this chapter will be the distinction between type I and type II superconductors and the origin of vortex matter. Chapter (3) presents the key features of the continuum and discrete descriptions of vortex matter in platelets and micro-disks. The basic operating principles of Hall magnetometry and MOI are discussed in chapter (4).

In chapter (5), we discuss the results of differential MOI used to investigate the superconducting state of arrays of BSCCO micro-disks fabricated on the surface of a single crystal sample. MOI difference images of the stray surface field distribution over a range of out-of-plane fields clearly allow one to distinguish between flux that is penetrating the disks and that entering the underlying BSCCO platelet. The flux preferentially flows into the interstitial platelet regions along linear defects up to the characteristic field, H_p, above which the disks also become penetrated with flux. We identify this as the field of first penetration of individual pancake vortices over the so-called Bean-Livingston surface barrier around the disks. The temperature dependence of this process, $H_p(T)$, at intermediate temperatures (30 K $< T <$ 80 K) is well described by an exponentially decaying function with a characteristic temperature T_0 = 19-25 K. We also find that a minority of the disks exhibit a lower penetration field at a given temperature and are able to correlate the location of these disks with the presence of linear defects (LDs) in the underlying platelet.

In chapter (6), Hall magnetometry results are used to investigate how the out-of-plane local magnetisation of a BSCCO single crystal depends on the strength and direction of an in-plane magnetic field, $H_{||}$. The remanent magnetisation in zero out-of-plane field is found to exhibit a pronounced anisotropy, being largest with $H_{||}$ parallel to the crystalline a-axis, and smallest when it is parallel to the orthogonal b-axis. This behaviour is attributed to the presence of the strongly pinning linear defects (LDs). With $H_{||}$ parallel to the a-axis Josephson vortex (JV) stacks become indirectly pinned along LDs, and channel pancake vortices (PVs) into these regions of high disorder, increasing the measured irreversibility. With $H_{||}$ along the b-axis PVs are efficiently channeled into the sample centre, readily cutting across LDs, and the irreversibility is low. At high temperatures

the remanent magnetisation as a function of the in-plane field angle exhibits a pronounced shoulder which appears to be related to the critical accommodation angle for the indirect trapping of JVs by LDs, above which JVs snap free. At low temperatures random bulk pinning is increasingly in competition with LDs, and the measured anisotropy becomes much weaker.

In chapter (7), SHPM and local Hall measurements are used to analyse the distribution of flux in individual BSCCO micro-disks. The radius of a central "dome" of vortices is mapped as a function of the applied field and the result is fitted to analytic models assuming a continuous spatial distribution of magnetic flux within the disk. At low fields in the smaller diameter (10 μm) disks, the compression of vortex clusters is observed in increasing field, resulting in an alternating expansion and contraction of the vortex dome as the vorticity changes. This "breathing" mode of the vortex dome is typically associated with mesoscopic superconductors and demonstrates that the size of the disks places them at the crossover point between the bulk and the mesoscopic regime. Additionally, for high fields when single vortex resolution is lost, configurational changes in the vortex patterns can still be tracked, as competing vortex orders leave clear signatures on magnetisation curves as a function of applied field. The results are fully corroborated by molecular dynamics simulations[1] which lead us to a natural definition of the lengthscale for the crossover between discrete and continuum behaviours in this system.

In chapter (8), the results of Hall magnetometry are used to explore the spectral distribution of the flux noise at the surface of a BSCCO platelet single crystal at both low (1-100 Hz), intermediate (100 Hz-50 kHz), and high (1-100 MHz) frequencies over a range of fields above and below the vortex lattice melting field. No correlation is identified between the applied magnetic field and the flux noise spectrum, nor any change in the spectral content of the noise at the melting field. It was not possible to establish whether the lack of any correlation implies that the characteristic frequency of vortex fluctuations is beyond the measurement range, or whether the separation between the Hall sensor and the surface effectively "smears" out the time dependence below the detection threshold. In the former scenario, a lower cutoff of the characteristic frequency for vortex fluctuations can be estimated as $\approx$ 100 MHz.

[1]Performed in collaboration with Milorad Milosevic.

Finally, chapter (9) concludes the thesis and discusses some future prospects for extending this work. Full details of the method used to fabricate the arrays of micro-disks from BSCCO single crystals are provided in appendix A.

Chapter 2

Introduction to Superconductivity

In 1911, Kamerlingh Onnes [15] discovered that the electrical resistance of pure mercury vanished abruptly to zero below a very low critical temperature (T_c), giving birth to the investigation, science and application of superconductors. In combination with this ability to conduct electricity without resistance, superconductors are able to expel flux from an externally applied magnetic field [16], a phenomenon known as the "Meissner" effect. The Meissner state is produced by magnetisation currents which flow in response to the applied field and have the effect of diverting the lines of magnetic flux away from sample's interior. Fig. 2.1(a) depicts how their field (M inside and H_M outside) combines with the applied field, H_a, to screen the lines of magnetic flux [dotted lines in Fig. 2.1(a).] The ideal magnetisation curve of a superconductor is shown in Fig. 2.1(b). The Meissner state, defined by the relation $M = -H_a$, survives up to a critical value of the applied field, H_c, which is found to decay strongly with increasing temperature. The temperature dependence of H_c is illustrated schematically by the curve in Fig. 2.1(c) and can be well represented by a parabolic relation [17]:

$$H_c = H_c(0)\left[1 - \left(\frac{T}{T_c}\right)^2\right]$$

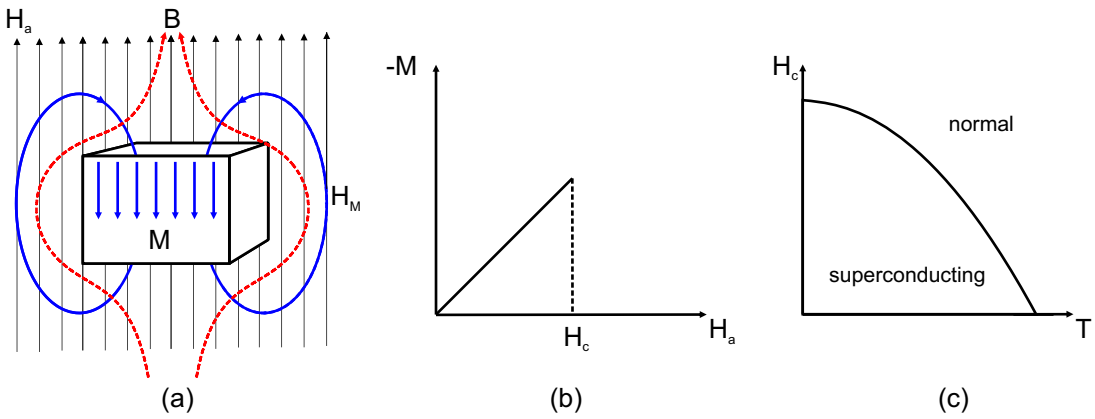

Figure 2.1: (a) The Meissner effect is the expulsion of flux (red) from the interior of a superconductor due to the magnetic field (blue) produced by surface currents in a static applied magnetic field (black). (b) The magnetisation curve of a superconductor as a function of the applied field. (c) Temperature dependence of the critical field.

2.1 London Theory

The screening currents responsible for the Meissner effect do not result from any known solution of Maxwell's equations, suggesting that additional equations are required for describing and predicting phenomena associated with superconductivity. On the basis of X-ray diffraction experiments which demonstrated that the structure of the underlying lattice of a superconductor remains constant during the transition [18], H. London and F. London postulated two equations for describing superconductivity which derive from the dynamics of a non-viscous "superelectron" sea, whose inviscid flow automatically accounts for the absence of resistivity [19]. The idea which forms the backbone of the London theory is that the superelectrons responsible for the resistanceless state only appear below T_c. Above T_c, the superelectron density, n_s, is zero and rises gradually until the transition is completed at absolute zero, when n_s is some fraction of the total electron density.

In order to incorporate the formation and presence of superelectrons into Maxwell's equations, the total current through a superconducting specimen is divided into a normal current density $\mathbf{J}_n$ and a temperature dependent super current density $\mathbf{J}_s$. While the normal current is proportional to the electric field through the constitutive relation $\mathbf{J}_n = \sigma\mathbf{E}$, a current composed of superelectrons cannot be generated by an electric field because the absence of viscosity would lead to an infinite acceleration. The spontaneous appearance of the supercurrent which

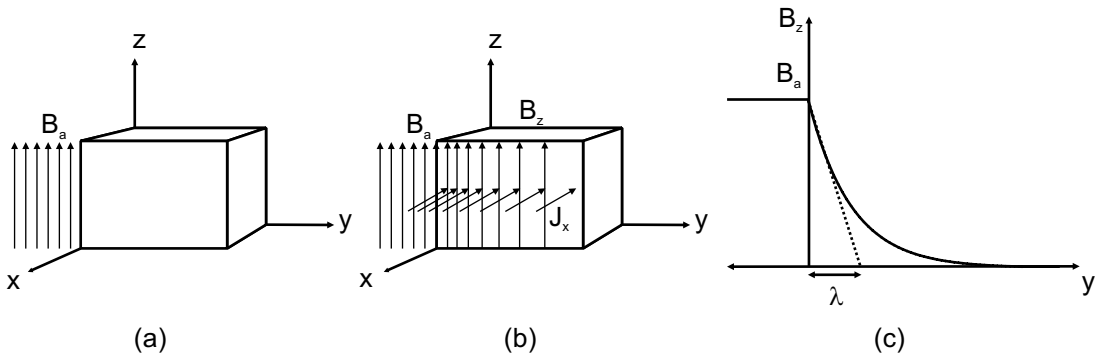

Figure 2.2: (a) Geometry of the superconducting half plane. (b) Illustration of the solution to the London equation for the current J_x and field B_z inside the superconductor. (c) Exponential decay of the flux density inside the superconductor over a characteristic length λ.

is responsible for the Meissner state in a magnetic field suggests instead that the force on the superelectron derives from the vector potential associated with the applied magnetic field [19]. This dependence is expressed concisely by the following two equations:

$$\begin{aligned} \nabla \times \mu_0 \Lambda \mathbf{J}_s &= -\mathbf{B} \\ \dot{\mathbf{J}}_s &= \frac{\mathbf{E}}{\mu_0 \Lambda}, \end{aligned} \tag{2.1}$$

where Λ is a characteristic parameter of the superconductor that depends on its temperature and material properties. The immediate consequences of these equations are found by substituting the first London equation into Maxwell's equation for Ampere's law $\nabla \times \mathbf{B} = \mu_0 \mathbf{J}_s$. The magnetic field is found to satisfy

$$\nabla^2 \mathbf{B} = \frac{\mathbf{B}}{\Lambda}. \tag{2.2}$$

To examine the solution to this equation, we consider the geometry shown in Fig 2.2(a) of a superconductor extending infinitely in the x and z directions. Everywhere to the left of the $y = 0$ line is a non-superconducting region in an applied field with flux density $\mathbf{B}_a = B_a \hat{z}$, and the problem is to find the supercurrent and magnetic field distribution for $y > 0$. Equation (2.2) only applies inside the superconductor and, since there is only a z-component of the applied field, only one term of the laplacian on the left hand side needs to be included. This yields

$$\frac{\partial^2 B_z}{\partial y^2} = \frac{B_z}{\Lambda},$$

which has the solution

$$B_z = B_a e^{-\frac{y}{\lambda}},$$

where we have ensured that the boundary condition $B_a = B_z$ is satisfied at $y = 0$. Fig. 2.2(b)-(c) shows how this solution decays rapidly to zero beyond a distance $\lambda = \sqrt{\Lambda}$ from the interface and the magnetic flux density inside the superconductor is negligible. The Meissner state therefore arises naturally from the London equation. This is not surprising, however, because the first London equation was postulated to yield this result [19]. The length scale λ over which the field varies in a superconductor is called the *penetration depth*.

As mentioned before, the motivation for postulating the first London equation is the similarity it shows to an equation derived from the classical picture of a sea of charged particles in a perfect conductor. We can derive this equation by considering a perfect conductor in an increasing magnetic field. According to Faraday's law of electromagnetic induction, the conductor will respond by creating persistent currents. If its initial state is not free from currents, then these induced currents will be superimposed on the original unknown distribution, and the net field inside will take on some unknown value. If, however, its initial state is free from currents, then the induced currents will balance the applied field exactly. Such currents will then be indistinguishable from those belonging to a perfect diamagnet, and hence from those in a superconductor. Therefore, by calculating the current distribution in a perfect conductor subject to the initial condition that $\mathbf{J}_s = 0$, the current distribution in a superconductor in a static magnetic field can be obtained indirectly.

In the absence of viscosity, the dynamics of a superelectron with charge q in a perfect conductor subjected to an electromagnetic field are governed by

$$m\frac{d\mathbf{v}_s}{dt} = q\left(\mathbf{E} + \mathbf{v}_s \times \mathbf{B}\right).$$

It can be shown [19] that if the initial conditions $\mathbf{v}_s = 0$ and $\mathbf{B} = 0$ are satisfied, then the superelectron's velocity will always satisfy the condition

$$\nabla \times \mathbf{v}_s = -\frac{q}{m}\mathbf{B}.$$

Furthermore, if this is assumed to hold true for the all the superelectrons that

make up the supercurrent, $\mathbf{J}_s = n_s q \mathbf{v}_s$, then

$$\nabla \times \mathbf{J}_s = -\frac{n_s q^2}{m}\mathbf{B}.$$

Comparing this with Eq. (2.2), we find that the constant Λ, and thus the penetration depth λ, is given by

$$\lambda = \sqrt{\Lambda} = \sqrt{\frac{m}{\mu_0 n_s q^2}}. \tag{2.3}$$

Since the penetration depth can be measured, the temperature dependence of the superelectron density n_s, which depends on the electronic structure of the material, can be determined using this expression. The inverse proportionality between the two parameters implies that an applied field penetrates deeper into the superconducting state as the temperature approaches T_c, when the superelectron density reduces to zero.

2.2 Ginsburg Landau Theory

It is evident that the temperature dependence of n_s cannot be derived from the London equations, which thus represent only one part of the theoretical description of superconductivity. Another part of the description is based on the observation that the transition of a body to the superconducting state is a phase transition. However, unlike the majority of phase transitions, the superconducting transition does not normally exhibit the characteristic signs of a first order transition, such as a release of latent heat or a discontinuous change in density, suggesting that it is usually of second order. An approach to describe such transitions was developed by L. Landau [20], who defined a transition to be second order if the state of the body changes discontinuously, the derivative of the specific heat is discontinuous at T_c, and the change in structure can be quantitatively described by defining an order parameter in such a way that it is positive below and zero above T_c. The first two statements are satisfied by the superconducting transition in zero field and Landau's theory is an implementation of the third statement using a complex order parameter, ψ, which characterises the transition in the same way as the superelectron density n_s in London theory.

The first step of the Ginsburg-Landau (GL) theory is to construct the Helmholtz free energy, F, as a function of ψ. The function $\psi(T)$, and hence $n_s(T)$, is then determined from the condition that $F(\psi(T))$ should have a minimum at a given temperature. The premise of GL theory is that the search for a suitable form of the functional $F(\psi(T))$ should be guided by the principle that ψ, and therefore the presence of superconductivity, *lowers* the free energy of the system. Letting the order parameter at the critical temperature take a value $\psi(T_c) = \psi_0$, the free energy at T_c can be expanded in a Taylor series about ψ_0:

$$F(\psi) = F(\psi_0) + \frac{dF(\psi_0)}{d\psi}(\psi - \psi_0) + \frac{1}{2!}\frac{d^2F(\psi_0)}{d\psi^2}(\psi - \psi_0)^2 + ... \tag{2.4}$$

This expression can be simplified by noting that the value of the free energy at T_c is the free energy of the normal phase, so $F(\psi_0) = F_n$. Also at T_c, when the normal and superconducting phases are in equilibrium, $\psi_0 = 0$ in order to make their free energies equal. Whence Eq. (2.4) becomes

$$F(\psi) = F_n + \frac{dF(0)}{d\psi}\psi + \frac{d^2F(0)}{d\psi^2}\psi^2 + ..., \tag{2.5}$$

and by defining

$$\alpha(T) = \frac{d^2F(0)}{d\psi^2},$$

and

$$\beta(T) = \frac{d^4F(0)}{d\psi^4},$$

the final form of the expansion is written in truncated form as

$$F_s = F_n + \alpha(T)\left|\psi\right|^2 + \frac{1}{2}\beta(T)\left|\psi\right|^4, \tag{2.6}$$

where only even exponents have been included so that the free energy is real. The condition for equilibrium is a minimum of F_s with respect to ψ. Thus

$$\frac{dF_s}{d\psi} = \alpha(T) + \beta(T)\left|\psi\right|^2 = 0,$$

and

$$\left|\psi\right|^2 = -\frac{\alpha(T)}{\beta(T)}. \tag{2.7}$$

To make $\left|\psi\right|^2$ positive, α is chosen to be negative below T_c, which ensures that $F_s(\psi)$ possesses a minimum value. The order parameter can be used to decribe the state of an inhomogeneous superconducting specimen by letting $\psi(T)$ vary

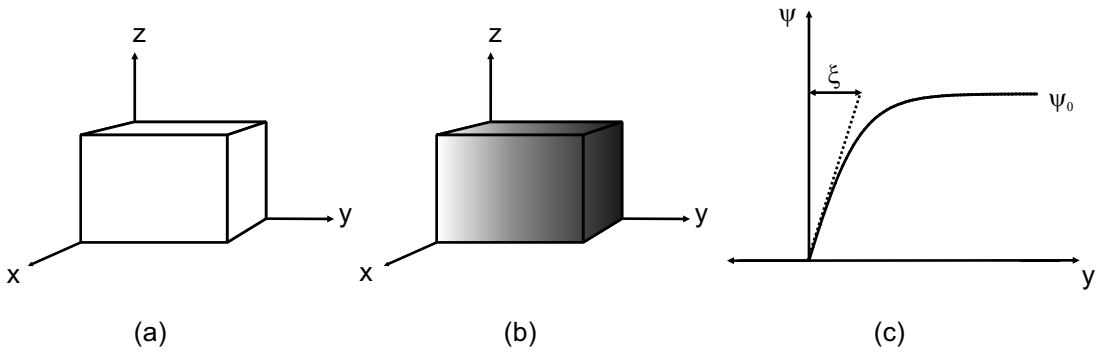

Figure 2.3: (a) Geometry of the superconducting half space. (b) Representation of the solution to Eq. (2.11) with the grayscale corresponding to the magnitude of the order parameter (c) The order parameter achieves its maximum value ψ_0 inside the superconductor over a characteristic length ξ.

as a function of space. The problem then becomes that of finding the scalar field $\psi(\mathbf{r}, T)$, again limited to temperatures around T_c, which minimises the Helmholtz free energy integrated over the sample volume. However, without some picture of the physical meaning of the order parameter, it is not obvious how any particular spatial distribution contributes to the free energy. Landau's idea was that $\psi(\mathbf{r})$ is equivalent to a macroscopic wavefunction, normalised such that $|\psi(\mathbf{r})|^2$ is proportional n_s. In this analogy, the kinetic energy term of the ordinary Schrödinger wave equation, $(\hbar^2/2m)\nabla^2\psi(\mathbf{r})$, can be used to express the additional energy due to spatial variations. By adding this contribution to the expression for the free energy the following expression is obtained

$$F_s = F_n + \int\int\int \left(\alpha(T)\,|\psi(\mathbf{r})|^2 + \frac{1}{2}\beta(T)\,|\psi(\mathbf{r})|^4 + \frac{\hbar^2}{2m}|\nabla\psi(\mathbf{r})|^2 \right) d^3\mathbf{r}, \qquad (2.8)$$

which, using the Euler-Lagrange equation, is stationary if ψ satisfies

$$\frac{\hbar^2}{2m}\nabla^2|\psi(\mathbf{r})| + \alpha(T)|\psi(\mathbf{r})| + \beta(T)\,|\psi(\mathbf{r})|^3 = 0. \qquad (2.9)$$

This equation illustrates an important feature of the GL theory. The specific distribution $\psi(\mathbf{r})$ which minimises the free energy now depends on the *geometry* of the sample through the boundary conditions used to find the particular solution to Eq. (2.9). As a result, there is an intimate link between the geometrical constraints imposed, for instance, by the sample's free surfaces, and the spatial variation of the superelectron density.

The geometry which illustrates this most clearly is the infinite superconducting half space. Let us consider the cross section of a slab of superconductor bounded by a normal region at $y = 0$, as depicted in Fig. 2.3(a). Since there can be no variation of the order parameter in the z or x direction, then $d\psi/dz = d\psi/dx = 0$, and Eq. (2.9) reduces to

$$\frac{\hbar^2}{2m}\frac{d^2\psi}{dy^2} + \alpha\psi + \beta\psi^3 = 0. \tag{2.10}$$

The solution $\psi(y)$ to Eq. (2.10) must also satisfy the condition that $\psi(0) = 0$. The function

$$\psi = \psi_0 \tanh(\frac{y}{\xi\sqrt{2}}) \tag{2.11}$$

satisfies both these conditions and is shown schematically in Fig. 2.3(b)-(c). The "bulk" value of the order parameter deep inside the superconductor is given by $\psi_0 = \sqrt{\frac{|\alpha|}{\beta}}$ and the parameter ξ is called the *coherence length*. The coherence length characterises the spatial variation of the order parameter in the same way that the penetration depth characterises the lengthscale for variations in the magnetic field. Its temperature dependence is given by

$$\xi(T) = \sqrt{\frac{\hbar^2}{2m|\alpha|}}. \tag{2.12}$$

Since within the GL theory the superelectron density is given by

$$n_s = |\psi|^2 = -\frac{\alpha(T)}{\beta(T)},$$

the penetration depth has the same dependence on the phenomenological parameter α as the coherence length,

$$\lambda(T) = \sqrt{\frac{m\beta}{\mu_0 e^2|\alpha|}},$$

Therefore the ratio of the two lengthscales defined by $\kappa = \lambda/\xi$, is approximately constant with temperature and κ is called the *Ginsburg-Landau parameter* of the material. Finally, the expression for the free energy of a superconductor is completed by adding a term to include any magnetic interactions between the order parameter and a magnetic field $\mathbf{B}$. Appealing once again to the picture of the order parameter as a complex wavefunction, the free energy is modified by the vector potential $\mathbf{A}$, which is related to the field by $\mathbf{B} = \nabla \times \mathbf{A}$ and enters

the free energy expression through the canonical momentum [21]:

$$\frac{\hbar}{i}\nabla\psi(\mathbf{r}) \rightarrow (\frac{\hbar}{i}\nabla - q\mathbf{A}(r))\psi(\mathbf{r}). \tag{2.13}$$

Whence Eq. (2.8) becomes

$$F_s = F_n + \int\int\int \left(\alpha(T)\left|\psi(\mathbf{r})\right|^2 + \frac{1}{2}\beta(T)\left|\psi(\mathbf{r})\right|^4 + \frac{\hbar^2}{2m}|\frac{\hbar}{i}\nabla - q\mathbf{A}(\mathbf{r})\psi(\mathbf{r})|^2\right) d^3\mathbf{r}. \tag{2.14}$$
$$+\frac{1}{2\mu_0}\int\int\int \mathbf{B}(\mathbf{r})^2 d^3\mathbf{r}$$

where the last term represents the total electromagnetic energy of the field. For the same reason as before, the spatial distribution of the order parameter must satisfy the following equation to minimise the free energy:

$$-\frac{\hbar^2}{2m}(\nabla - \frac{qi}{\hbar}\mathbf{A}(\mathbf{r}))^2\psi\mathbf{r}) + (\beta|\psi(\mathbf{r})|^2) - \alpha)\psi(\mathbf{r}) = 0. \tag{2.15}$$

2.3 The Intermediate State

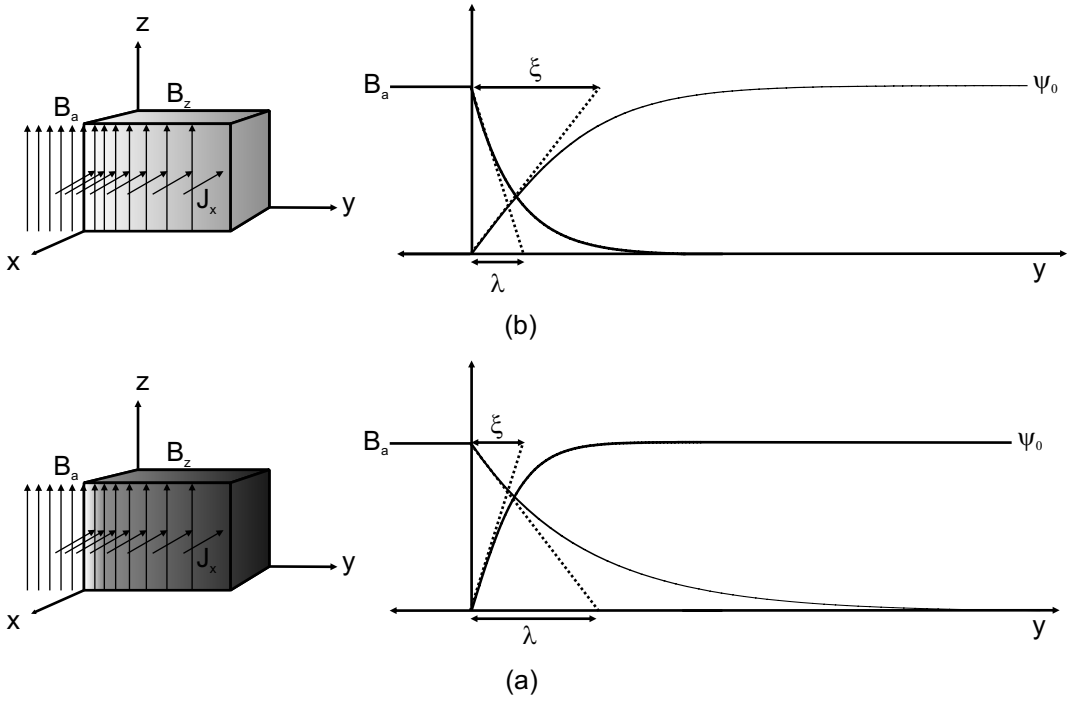

Figure 2.4: Relation between the spatial distribution of the fields and the order parameter (superelectron density) in a (a) Type II (b) Type I superconductor. Grayscale in the cartoons on the left is proportional to the order parameter.

Eq. (2.15) is a particularly important tool for describing superconductivity because the homogeneous (constant n_s and ψ) and perfectly diamagnetic ($B = 0$) state of a specimen in an external magnetic field is difficult to observe in practice. When subjected to a magnetic field, superconductors often break up into a mixture of non-superconducting and superconducting regions, like domains with opposite polarisation in a ferromagnet, a situation which is known as the *intermediate state*. The exact way in which a specimen will enter the intermediate state depends on the energy cost of forming interfaces between the normal (non-superconducting) regions, where ψ is zero, and the superconducting regions where ψ is finite. If the interface energy is costly, a specimen will prefer to nucleate large connected domains, so as to minimise the surface energy. Conversely, if it is advantageous, the superconductor will form small isolated pockets, so as to maximise the surface energy. It is possible to derive an approximate expression for the dependence of the surface energy on the properties of the material using the following argument from Ref. [22].

Since the uniform superconducting state lowers the total energy of the system

when its temperature is brought below T_c, any reduction in the amount of superconductivity due to the presence of a normal region must increase the overall system energy. Because this normal interface extends over a length ξ, an estimate of the increase in free energy per unit area, or condensation energy, is $[f_n(0) - f_s(0)] \times \xi$, where f is the specific Helmholtz free energy density. From thermodynamics [21], the condensation energy is found equal to $\frac{1}{2}\mu_0 H_c^2$. In addition to the gain in energy due to the *loss* in superconductivity, there is a loss in field energy due to the screening of the magnetic field over the length λ in the superconducting region. In the region where the field diminishes, the field energy is lowered by the superconducting state by an amount approximately equal to $\frac{1}{2}\mu_0 H_c^2 \lambda$. Therefore the total surface energy is given by

$$\sigma = \frac{1}{2}\mu_0 H_c^2 (\xi - \lambda).$$

The fact that σ can be positive or negative depending on the relative values of ξ and λ implies that there are two regimes of behaviour. If $\xi > \lambda$, as is illustrated in Fig. 2.4(b), then a superconductor will try to avoid the intermediate state and is called a superconductor of the first category, or *type I*. Since they favour the pure state, type I materials only enter the intermediate state if it is imposed by the geometry or disorder of the specimen. The typical type I intermediate state consists of large connected domains containing large amounts of flux from the applied field. In the opposite regime, where a material satisfies $\lambda > \xi$, a distribution of normal-superconducting interfaces is an *intrinsically* lower energy state in a magnetic field and the material is of the second category, or *type II* [Fig. 2.4(a)]. A large number of isolated normal regions is therefore expected to form when this type of superconductor is subjected to a magnetic field.

2.4 Flux Quantisation

The normal-superconducting interfaces which spread throughout the bulk of both types of superconductor in the intermediate state are conceptually no different to the free surfaces treated by London theory. Hence the fields and currents must also be related through the London equations. We consider the situation represented schematically in Fig. 2.5, where a total flux Φ threads an isolated non-superconducting region surrounded by a uniform superconducting region.

Rather than linear surface currents, here the flux now gives rise to a vortical screening current distribution which satisfies

$$\nabla \times \mu_0 \lambda^2 \mathbf{J}_s + \mathbf{B} = 0.$$

The solutions to this equation will obviously depend on the geometry of the normal region, as well as the amount of flux trapped in it. Nonetheless, it is possible to gain an important insight into the consequences of this equation by considering the mathematical properties which must be true of all valid solutions. Integrating the fields and currents over the surface S bounded by the path C enclosing the normal region [indicated by the red line in Fig. 2.5],

$$\int\int (\nabla \times \mu_0 \lambda^2 \mathbf{J}_s) \cdot d\mathbf{S} + \int\int \mathbf{B} \cdot d\mathbf{S} = \Phi',$$

where Φ' is a constant called the *fluxoid* associated with the path C. Time variations in an applied field will lead to a time variation of the fluxoid given by

$$\frac{d\Phi'}{dt} = \int\int (\nabla \times \mu_0 \lambda^2 \dot{\mathbf{J}}_s) \cdot d\mathbf{S} + \int\int \dot{\mathbf{B}} \cdot d\mathbf{S}.$$

Maxwell's equation implies that electric fields satisfying $\dot{\mathbf{B}} = -\nabla \times \mathbf{E}$ will be generated by a time varying magnetic field. At the same time, the second London equation $\dot{\mathbf{J}}_s = \mathbf{E}/\mu_0 \lambda^2$ also implies that this electric field will alter the currents in the superconducting region. Substituting the equations describing these complementary effects into the above integral results in

$$\begin{aligned} \frac{d\Phi'}{dt} &= \int\int (\nabla \times \mu_0 \lambda^2 \dot{\mathbf{J}}_s) \cdot d\mathbf{S} + \int\int \dot{\mathbf{B}} \cdot d\mathbf{S} && (2.16) \\ &= \int\int (\nabla \times \mathbf{E}) \cdot d\mathbf{S} - \int\int (\nabla \times \mathbf{E}) \cdot d\mathbf{S} \\ &= 0. && (2.17) \end{aligned}$$

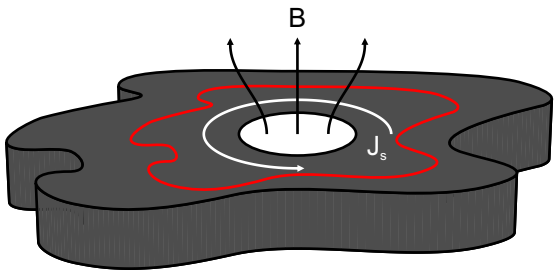

Figure 2.5: Field threading a normal region (white) surrounded by superconductivity (gray). Red line is an arbitrary path for integrating the supercurrent J_s.

The fluxoid is thus conserved during changes of the magnetic field. Using the well known identity between the curl and the line integral of a function,

$$\int\int(\nabla \times \mathbf{X}) \cdot d\mathbf{S} = \oint \mathbf{X} \cdot d\mathbf{s},$$

the fluxoid Φ' can be expressed as the following sum

$$\Phi' = \oint (\mu_0 \lambda^2 \mathbf{J}_s) \cdot d\mathbf{s} + \int\int \mathbf{B} \cdot d\mathbf{S}.$$

The second term in this sum is the total flux Φ through the normal hole. It can also be written in terms of a line integral of the vector potential by using

$$\int\int \mathbf{B} \cdot d\mathbf{S} = \oint \mathbf{A} \cdot d\mathbf{s}.$$

Hence

$$\begin{aligned} \Phi' &= \oint (\mu_0 \lambda^2 \mathbf{J}_s) \cdot d\mathbf{s} + \oint \mathbf{A} \cdot d\mathbf{s} \\ &= \frac{1}{q} \oint (m\mathbf{v}_s + q\mathbf{A}) \cdot d\mathbf{s}. \end{aligned} \tag{2.18}$$

This equation relates the value of the fluxoid and the canonical momentum distribution $\mathbf{p}(\mathbf{r}) = m\mathbf{v}_s(\mathbf{r}) + q\mathbf{A}(\mathbf{r})$. (The first term $m\mathbf{v}_s$ represents the kinetic momentum of the superelectrons and the second term $q\mathbf{A}$ is the momentum associated with the field [23].) At first sight it seems that the two components are independent, i.e., that any combination is possible, resulting in a continuum of values for the flux through a normal region in a superconductor. However, the cause for the supercurrent distribution around the hole is the Lorentz force, which derives from the field threading the normal region, so the two cannot be independent. Moreover, their dependence on one another is formalised under the Bohr-Sommerfeld postulate of early quantum theory, which states that the line integral of the canonical momentum around a closed path takes integer values:

$$\oint \mathbf{p} \cdot d\mathbf{s} = nh.$$

Consequently the fluxoid is quantised,

$$\begin{aligned} \Phi' &= \frac{1}{q} \oint \mathbf{p} \cdot d\mathbf{s} = \frac{nh}{q} \\ &= n\Phi_0, \end{aligned} \tag{2.19}$$

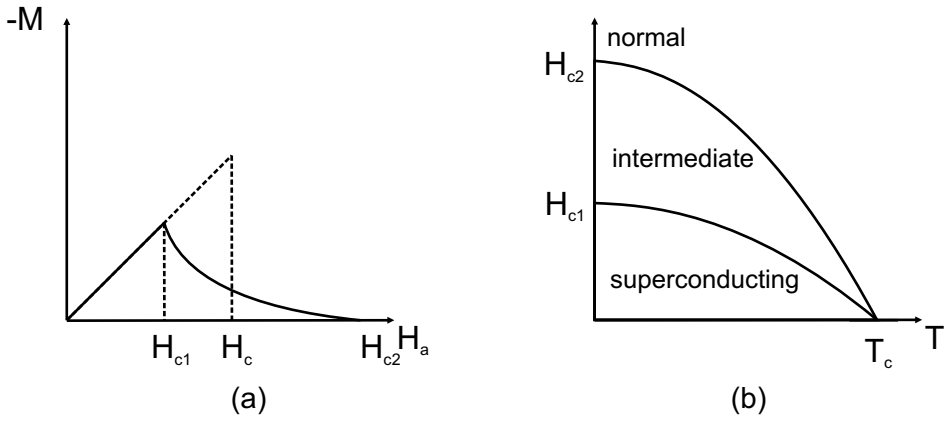

Figure 2.6: (a) Magnetisation curve of a type II superconductor (solid line.) The dotted line indicates the magnetisation of a type I superconductor. (b) Temperature dependence of the lower and upper critical fields.

where the *flux quantum* is defined as $\Phi_0 = h/q$.[1] Contrary to our intitial expectation, therefore, a type II superconductor *does not* enter the intermediate state as soon as a field is applied, but only when the applied field can supply a quantum of flux over an area $\approx \pi\lambda^2$. The field at which this occurs is called the *first critical field*, H_{c1}, which is given by the following approximate expression

$$H_{c1} \approx \frac{\Phi_0}{\pi\lambda^2}. \tag{2.20}$$

The magnetisation curve of a type II superconductor is depicted schematically in Fig. 2.6(a). Instead of the sharp drop in magnetisation associated with a type I transition, the magnetisation of a type II sample falls gradually when $H_a > H_{c1}$. In addition, $H_{c1}(T)$ follows the same temperature dependence as H_c [c.f. Fig. 2.1(c),] and an upper critical field, H_{c2}, corresponds to the field when superconductivity is completely destroyed.

2.5 Vortex Matter

It was A. A. Abrikosov who discovered that the transition to the intermediate state of a type II superconductor subjected to a field exceeding H_{c1} can be formally analysed in greater detail using GL theory. The resemblance between the magnetic properties of type I thin films and type II bulk specimens motivated

[1] It is now well established that superelectrons consist of paired electrons, making $q = 2e$.

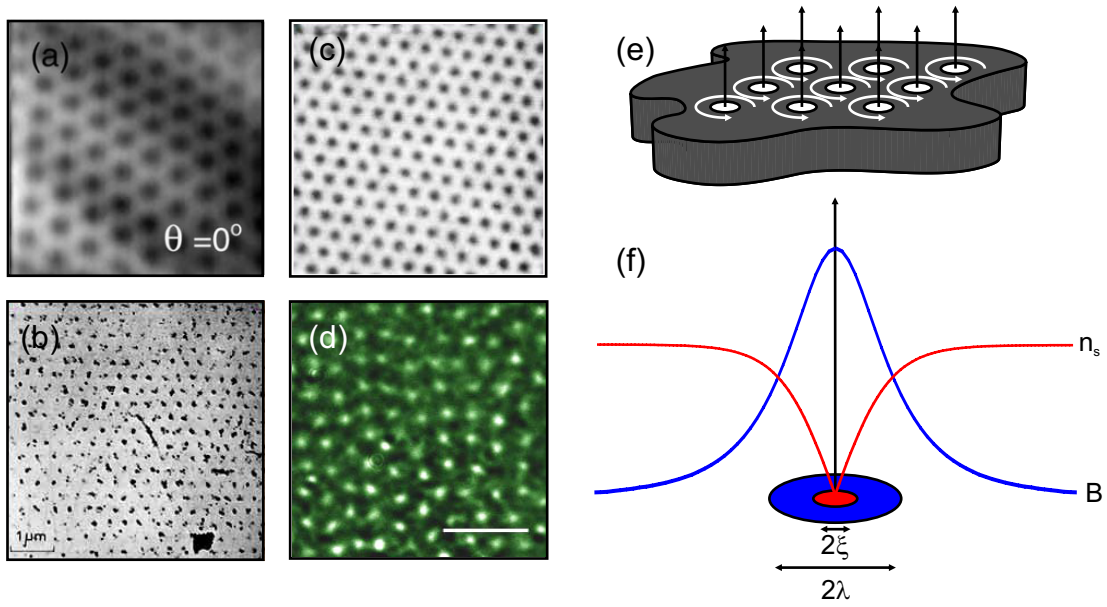

Figure 2.7: Images of the Abrikosov state of type II superconductors with different GL parameters. (a) BSCCO (12 Oe, 81 K), κ= 100. (Reproduced from Ref. [25].) (b) Lead alloy (3000 Oe, 1.1 K), κ= 75. (Reproduced from Ref. [26]) (c) $NbSe_2$ (1000 Oe, 1.2 K), κ=9. (Reproduced from Ref. [27].) (d) Disordered lattice in $NbSe_2$. (Reproduced from Ref. [28].) (e) Cartoon of the Abrikosov state. Each vortex is represented by a line of flux surrounded by a circulating current.(f) The field (blue) of a vortex drops off over a length λ, whilst the superelectron density (red) falls to zero at the non-superconducting core.

him to propose and examine the solutions to the complete GL equation[2] in the regime where κ is large [24], a regime which had hitherto been ignored because most superconductors at the time were type I. He found that the lowest energy solution of a type II superconductor in a magnetic field $H > H_{c1}$ consists of a large number of non-superconducting nodes arranged in a periodic triangular lattice containing one flux quantum at each lattice site, formally confirming the argument for isolated normal regions that was based on surface energy considerations. Wherever a normal region forms, circulating supercurrents extending over a lengthscale approximately equal to λ divert the flux away from the surrounding superconductivity (Fig. 2.5), and these regions of persistent circulating supercurrents, together with the normal cores they enclose, are refered to as superconducting vortices. The triangular lattice of vortices has since been frequently observed using a number of techniques and is a well accepted picture of the intermediate state in highly ordered type II superconductors at the microscopic scale [25]. Fig. 2.7(a)-(d) shows a selection of images obtained by local probes specially designed to detect the micron sized variations in the vortex exit fields at the surface of type II specimens. The triangular lattice is clearly vis-

[2]C.f. Eq. (2.15).

ible in each material and is depicted schematically in Fig. 2.7(e) as an array of flux lines circulated by supercurrents. There is evidently a wide variation in the size of the vortices due to differences in the underlying superelectron density, which determines λ through Eq. (2.3). The intuitive reason for why the lattice is triangular is because the vortical supercurrents surrounding adjacent vortices flow in opposite directions, resulting in a repulsive interaction, and it is only in this configuration that the resultant force on each vortex core is balanced. It is worth noting, however, that the vortices are not completely free from the underlying material and the ground state is often a disordered lattice, as shown in Fig. 2.7(d). Randomly distributed defects and impurities attract vortices, preventing them from leaving the material, even when the field is below H_{c1}, a phenomenon which is known as vortex "pinning".

2.6 The High-T_c Cuprate Superconductors

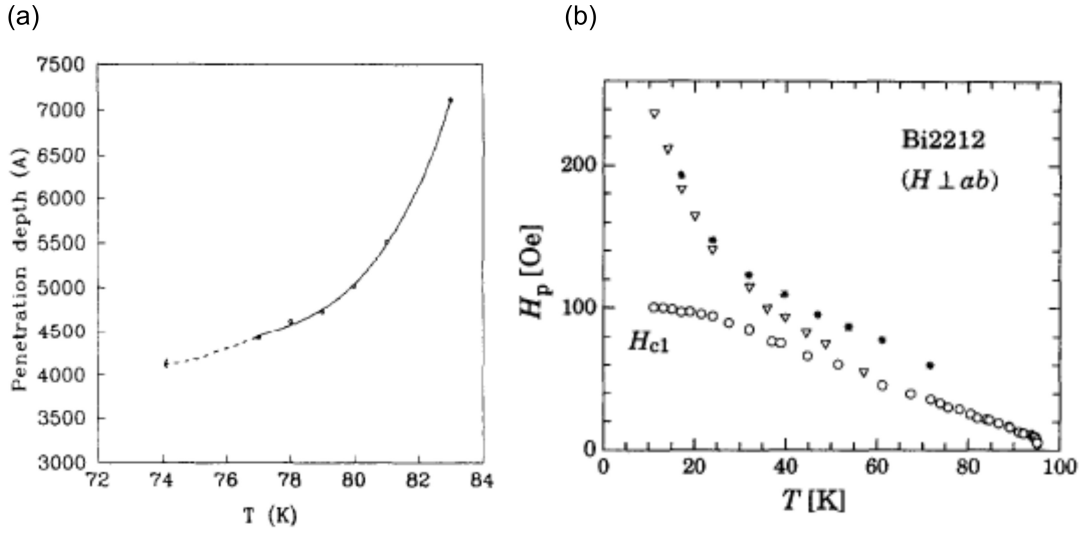

Figure 2.8: (a) Penetration depth of BSCCO as a function of temperature. (Reproduced from [29].) (b) First critical field H_{c1} (○) as a function of temperature. (Reproduced from [30].)

Over the last few decades, a large number of experiments sensitive to the behaviour of flux quantised vortices in a family of extreme type II (κ=100) copper-oxide based superconductors have yielded a great deal of valuable information about the vortex state over a wide range of fields and temperatures. The first cuprate discovered in 1986 was polycrystalline LaBaCuO with a critical temperature of 35 K. The discovery of other cuprates followed rapidly afterwards; the $YBa_2Cu_3O_7$ (YBCO) and $Bi_2Sr_2CaCu_2O_{8+\delta}$ (BSCCO) compounds pushed the record as high

as 120 K and as a result they are considered to be the first of the "high-T_c" superconductors (HTSs). The coherence length in the cuprates is very short (1-2 nm) while the penetration depth is of the order of 100-200 nm, making $\kappa \approx 100$. Although the mechanism of superconductivity in the cuprates is still unknown, a great deal of data characterising their phenomenological behaviour is available in the literature. The data in Fig. 2.8 show the temperature dependence of the penetration depth and the lower critical field (H_{c1}) for BSCCO ($T_c \approx 90$ K), in which the magnetic size (λ) of the vortices is therefore around 1 μm and the transition to the vortex state occurs within the range 1-100 Oe. The crystalline structure of the cuprates has been examined in great detail, largely because it may contain the secret to their ability to superconduct at high temperatures [31]. The structure and the definitions of the lattice vectors of the BSCCO system are shown in Fig. 2.9. Particular attention should be paid to two lengthscales of the crystal lattice along the c-axis: the size of the unit cell (≈ 3 nm) and the thickness of the bilayers of copper oxide (CuO_2), which is an order of magnitude less at only ≈ 0.3 nm. These dimensions turn out to be very important because the CuO_2 planes are widely thought to be where the superconductivity resides; the amount of the other components in the spaces between the superconducting layers, whose electrons are donated to the CuO_2 planes, plays only a secondary role in controlling the critical temperature. In BSCCO, T_c varies between 70 - 90 K depending on the oxygen doping level. Hence BSCCO single crystals can be seen as a stack of quasi two dimensional superconductors separated by insulating layers of dopants.

Although crystalline anisotropy is characteristic of all cuprate superconductors, it is particularly pronounced in BSCCO because the spacing between the superconducting layers is an order of magnitude larger than the superconducting layers themselves ($\approx \xi$), as shown in Fig. 2.9(b). A novel consequence of this is the formation of "crossing" vortex lattices for applied fields tilted more than a few degrees from the high symmetry c-axis. In this regime, orthogonal sublattices of 'pancake' vortex (PV) stacks and Josephson vortices (JVs) coexist. The PV currents contain flux directed along the crystalline c-axis and are confined to flow within the CuO_2 planes. The JVs lie in the $a-b$ plane and possess highly anisotropic circulating currents derived from the superconducting planes. The anisotropic current distribution associated with the in-plane JVs leads to strongly anisotropic JV-JV interactions and a rhombic vortex lattice whose unit cell is greatly stretched out in the $a-b$ plane. The JV supercurrents also induce

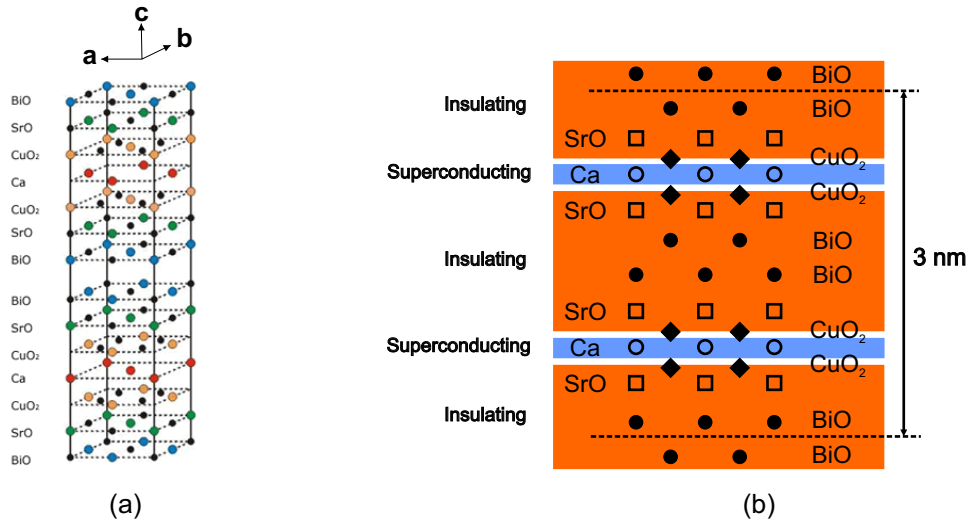

Figure 2.9: (a) 3-D representation of the crystal lattice of BSCCO. The CuO_2 planes consist of a 'checkerboard' of Cu atoms, each with 4 Oxygen atoms (b) Illustration showing the locations of the alternating superconducting-insulating layers relative to the crystal structure. Adjacent planes are separated by half the unit cell.

a restructuring of PV stacks which leads to an attractive interaction between the crossing lattices [32], as was clearly demonstrated in recent JV "decoration" experiments [25, 33, 34, 35]. The crossing lattice system is illustrated schematically in Fig. 2.10 accompanied by a scanning Hall probe microsocopy (SHPM) image of the state, where a mixture of lattice vortices and meandering vortex chains in the direction of the in-plane field in BSCCO is clearly visible. Indeed, this 'chain + lattice' state [region (IV) of Fig. 2.10(a),] first reported in Bolle *et al* [**?**, 36], is the archetypal image which lead to the discovery of the crossing lattice.

The formal analysis of crossing lattices is based on the theory developed by Lawrence and Doniach for describing a superstructure of alternating superconducting-insulating layers, which is much like the intrinsic layering seen in the cuprates. In this theory, the ordinary GL free energy is modified to incorporate the weak currents between adjacent layers. Unlike superconductors with moderate anisotropy, whose vortices tilt with the applied field [32], the free energy penalty of tilting PV stacks in BSCCO turns out to be large due to the *magnetic* coupling between PVs in adjacent layers. As a consequence, in the ground state the system prefers to align PV stacks with the c-axis, at least at low fields and temperatures, with currents between the planes. The extent of the JV-PV interaction can vary considerably depending on the ratio of the out-of-plane (H_z) to in-plane ($H_{||}$) field strengths. For instance, the dilute JV lattice at low in-plane fields will have little re-ordering effect on a dense lattice of PVs in a strong out-of-plane field. (See

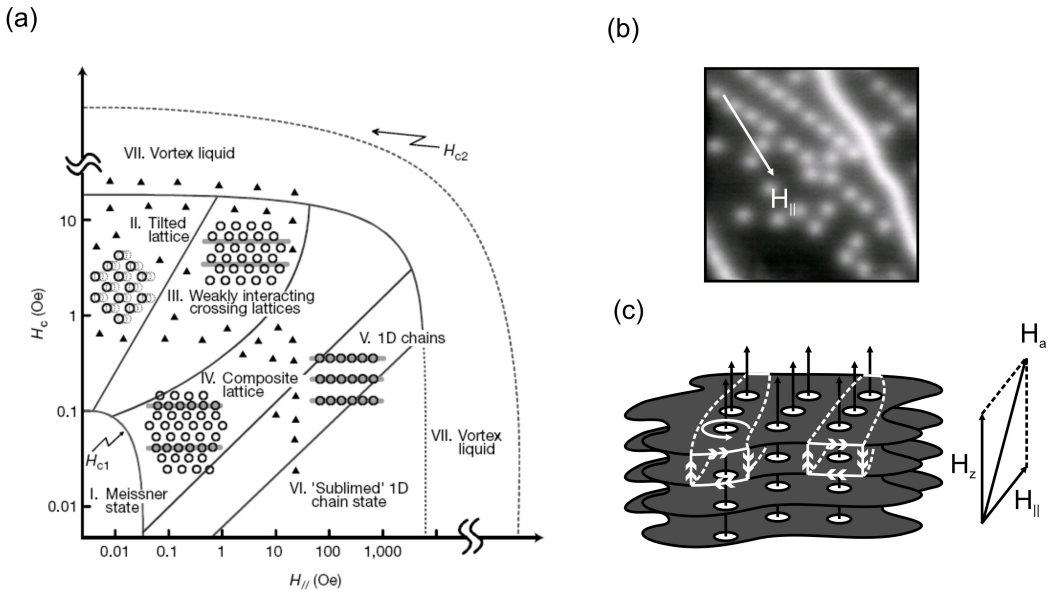

Figure 2.10: (a) Tentative phase diagram for the crossing lattice (Reproduced from [25].) (b) The composite lattice regime (region (IV) of the phase diagram) revealed in an (archive) SHPM image of a BSCCO single crystal in a tilted field. (c) Cartoon illustrating the BSCCO system of quasi 2-D pancake vortices and in-plane Josephson vortex currents.

Fig. 2.10(a) for examples of other phases.)

2.7 Summary

To summarise, the core concepts of the electromagnetic and thermodynamic phenomenology of superconductors have been introduced. The London theory of superconductivity was shown to describe the flux-free Meissner state using the concept of a penetration depth λ over which magnetic fields decay into the bulk of a superconductor. The formation of superelectrons below the critical temperature was described and the origin of the Meissner screening currents was shown to follow from the force on the superelectrons due to the magnetic vector potential of an applied field. The Ginzburg-Landau equation describing the variation of the order parameter was derived and solved in a simple geometry to find an expression for the temperature dependence of the coherence length ξ, leading to the definition of the temperature independent GL parameter κ as the ratio of the penetration depth and the coherence length. Using an argument based on the surface energy at a normal-superconducting interface, the two lengthscales of superconductivity were shown to govern whether a superconductor is type I

or type II, and the difference between the intermediate state in the two types was discussed. The properties of the vortical supercurrents around the normal regions in a type II superconductor were derived and the application of the quantum Bohr-Sommerfeld condition to the canonical momentum of the supercurrent established the flux quantisation condition and the idea of the first critical field H_{c1}. Examples of the triangular Abrikosov vortex lattice in type II superconductors having a range of Ginsburg-Landau parameters were presented and finally the "crossing" vortex lattice in the highly anisotropic high temperature superconductor was introduced. Before proceeding to address the questions outlined in the previous chapter, we will draw on these concepts in the next chapter to explore the background theories behind vortex penetration and distribution in superconducting disks and platelet single crystals.

Chapter 3

Background Theory

3.1 The Bean-Livingston Surface Barrier

We can gain a rudimentary insight into the effect of the surface of a type II superconductor on vortex penetration by considering the infinite superconducting half-space in a local magnetic field H_L, which decays exponentially from its surface. The strength of H_L in order for a single vortex line to enter determines the critical field for the transition to the vortex state. This "target" vortex, whose currents flow with a sense which produces a field in the same direction as H_L, penetrates the surface and reaches a point y inside the superconductor. The vortical currents will have a highly distorted form near the surface because they cannot flow perpendicular to it. Conceptually, the resulting current distribution can be found by placing its "antivortex" mirror image, whose currents flow in the opposite sense, at a distance $-y$ from the surface [37], as is illustrated in Fig. 3.1(a). Since currents with opposite senses attract, there is an attraction between the two vortices, and the vortex is pulled to the surface. Work must be done against this attractive force for a vortex to escape the surface attraction and move into the bulk of the sample. The amount of work required is equal to the interaction energy between two flux threads, which is given by the expression [37]

$$E_1(y) = \epsilon - \left(\frac{\Phi_0^2}{4\pi\mu_0\lambda^2}\right) K_0\left(\frac{2y}{\lambda}\right),$$

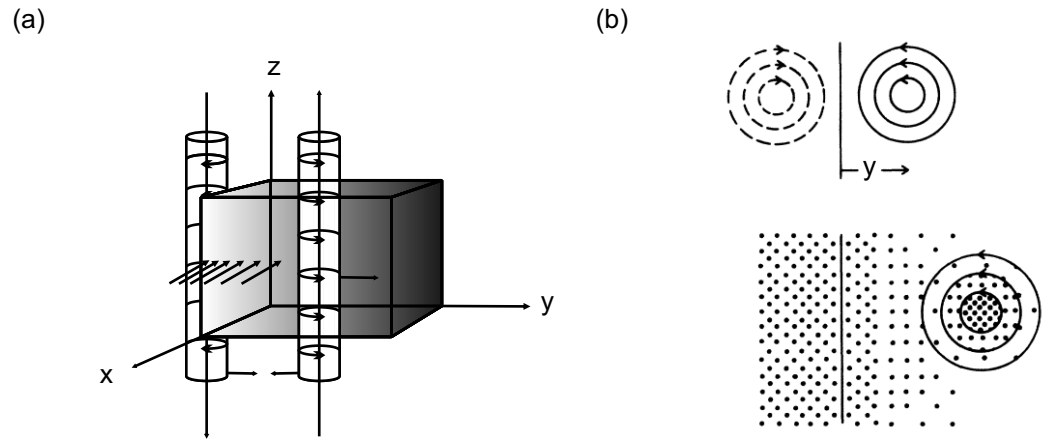

Figure 3.1: (a) A vortex line inside and its image outside the superconducting infinite half-plane in the Meissner state. (b) Two forces act on a vortex at a distance y from the edge. The image force (top) is attractive and the Meissner force is repulsive (bottom.) (Adapted from [37].)

where

$$\epsilon = \left(\frac{\Phi_0^2}{4\pi\mu_0\lambda^2}\right)\ln(\kappa)$$

is the line energy of an isolated vortex [17], and K_0 is the zero-order Bessel function. At the same time, the vortex experiences a repulsive force from the decaying field [Fig. 3.1(b)] and the dipole-like expression obtained for the energy of the vortex is

$$E_2(y) = \Phi_0 H_L e^{-\frac{y}{\lambda}}.$$

Hence the total potential energy E_T gained by the target vortex is given by the sum of $E_1 + E_2$,

$$E_T(y) = \epsilon - \left(\frac{\Phi_0}{4\pi\mu_0\lambda^2}\right)K_0\left(\frac{2y}{\lambda}\right) + \Phi_0 H_L e^{-\frac{y}{\lambda}}. \tag{3.1}$$

The form of E_T is shown in Fig. 3.2(a) as a function of position for three local field strengths $H_L = 0$, $H_L = H_{c1}$, and $H_L = H_s$. These plots are constructed using a value of $\kappa = 100$ and a penetration depth of $\lambda = 0.5\ \mu m$, which are of the correct order for BSCCO at 77 K. Evidently the potential energy of a vortex depends strongly on the local field at the surface. At low fields, when the minimum energy of the vortex is located outside the specimen [solid line, Fig. 3.2(a),] the vortex does not enter and the superconductor persists in the Meissner state. At a higher field, the repulsion from the surface due to the Meissner field begins to dominate

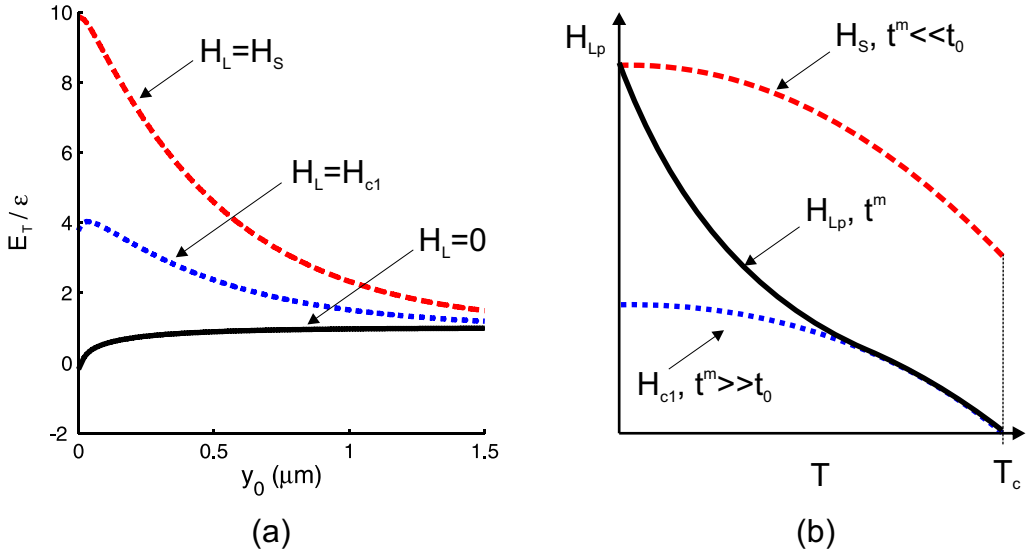

Figure 3.2: (a) Potential energy in units of the line tension as a function of distance from the edge. (b) Temperature dependence of the local field at penetration. For measurement times less than t_0 (red curve), thermal activation over the barrier is unlikely and the transition does not occur until H_S, when the barrier disappears. For measurement times much longer than t_0 (blue curve), the transition will be measured at H_{c1} [c.f., Fig. 2.8.]. At intermediate times and temperatures the measured penetration field will fall between these extremes, and the black solid line depicts the expected variation.

and the vortex energy at the centre is lower in comparison to the edge [dotted line, Fig. 3.2(a).] However, close to the edge, where the image and Meissner forces are comparable, there is a potential barrier preventing the vortex from moving to the centre. This barrier, which is called the Bean Livingston surface barrier (BLB) [37], only disappears when H_L reaches H_S [dashed line, Fig. 3.2(a),] which is actually higher than H_{c1}. In order to estimate H_S as a function of temperature explicitly, we assume that the BLB does not disappear until the maximum in E_T is within a coherence length of the surface [22]. In other words, $H_L = H_S$ when

$$\left(\frac{\partial E_T}{\partial y}\right)_{y=\xi} = 0.$$

Applying this condition to E_T, the following is obtained [17]

$$H_S = \frac{\Phi_0}{4\pi\mu_0\lambda\xi} = H_{c1}\frac{\kappa}{\ln(\kappa)}. \tag{3.2}$$

Hence, assuming that κ is temperature independent, H_S is larger than H_{c1} by a factor of $\kappa/\ln(\kappa)$ and follows the same approximately parabolic temperature dependence.[1] Since the BLB separates two local potential minima, it has a subtle

[1] C.f. Fig. 2.8.

effect on the conditions for the transition to the vortex state. At finite temperatures, a vortex will eventually attain enough thermal energy to enter the sample even when $H_L < H_S$. Hence, given a sufficiently long time after the application of the field H_L, the transition to the vortex state is ultimately unaffected by the BLB. This fact has been exploited in Nideröst *et al.* [30] to measure the temperature dependence of H_{c1} shown earlier in Fig. 2.8.

However, at absolute zero, when the vortex energy is limited to $\Phi_0 H_{c1}(0)$, the transition will genuinely be thermodynamically impossible until $H_L = H_S$. This is also true even at finite temperatures when the observation time is less than t_0, the minimimum time required for vortex energy fluctuations. By definition, the vortex has no time to acquire an energy greater than $\Phi_0 H_{c1}(0)$ within t_0. The reciprocal of t_0 is called the attempt [38, 39] or characteristic [17, 40] frequency ν_0 of the vortex vibration. It is unknown in detail, but assumed to lie in the range from 10^5 to 10^{11} Hz. By considering the flux lattice as a ensemble of harmonic oscillators, Brandt [40] derives a value for ν_0 as a function of field and temperature. (The reader is refered to chapter 8 for a discussion of vortex fluctutations.) The temperature dependence of the penetration field $H_{Lp}(T)$ in the two limits $t^m >> t_0$ and $t^m << t_0$ of the observation time are illustrated by two curves in Fig. 3.2(b). It is possible to gain a qualitative insight into $H_{Lp}(T)$ for a realistic measurement interval, say of $t^m \approx 100$ s, at low and high temperatures. At low temperature, there is insufficient thermal energy available to the vortex to reduce the time required for noticeable thermal activation over the BLB to 100 s, so the observed penetration field will be close to $H_S(T)$. At high temperatures, there is sufficient thermal energy to cause almost instantaneous thermal activation over the BLB at H_{c1}, so here the temperature dependence should follow $H_{c1}(T)$. To determine the exact form of $H_{Lp}(T)$ in BSCCO over the intermediate regime of temperature and time scales, we must consider the following analysis based on the ideas of Burlachkov *et al.* [7] and Kopylov *et al.* [39]. A consequence of the strong layering in BSCCO is the high possibility that an individual pancake vortex surmounts the BLB independently of the rest of the stack [39, 7]. This reduces the effective height of the BLB for an entire PV stack to that of a single PV, making thermal activation a particularly important mechanism for penetration in BSCCO. In addition, the large GL parameter makes H_S an order of magnitude larger than H_{c1}, so the BLB is particularly high in this material. The analogous expression to Eq. (3.1) for the total energy of a single pancake interacting with

its image and the Meissner current j is given by [38]

$$U(y) = \epsilon s \ln\left(\frac{2.94y}{\xi}\right) - \Phi_0 s j y, \tag{3.3}$$

where $s \approx 1.5$ nm is the spacing between the copper-oxide bilayers. The distance of the barrier from the surface is found using the same criterion as before and is given by

$$y_0 = \frac{\epsilon}{\Phi_0 j},$$

and the resulting barrier height at y_0 is [39, 38]

$$U_0 = \epsilon s \ln\left(\frac{H_c}{H_L}\right), \tag{3.4}$$

where H_c is the thermodynamic critical field. We consider a field H_L at the surface of a layered high κ superconductor. In a time dt, the total number of times a single PV stack attempts to overcome the barrier U_0 is $p_0 = dt/t_0$. The number of these attempts, $p(U)$, possessing energy U obeys the Boltzmann distribution, which is approximately given by

$$p(U) = p_0 e^{\left(\frac{-U}{kT}\right)}. \tag{3.5}$$

Since a PV will only surmount the BLB when $U = U_0$, then the number of successful entrances is $p(U_0)$. As a result of the PVs which successfully enter the sample, the local field within a coherence length ξ of the specimen surface will increase by

$$dH_i = \frac{dB}{\mu_0} = \frac{p(U_0)\Phi_0}{\mu_0 W \xi}, \tag{3.6}$$

where W is a length of the order of the sample width [39]. Substituting Eq. (3.5) into Eq. (3.6) yields

$$dH_i = \frac{\Phi_0}{W\mu_0\xi} \times \frac{1}{t_0} \times e^{\left(\frac{-U_0}{kT}\right)} dt. \tag{3.7}$$

Integrating this expression between the $t = 0$ and $t = t^*$, the time elapsed since the application of the applied field, the internal field H_i is found to reach a fraction of H_L at

$$t^* \approx t_0 e^{\left(\frac{U_0}{kT}\right)}. \tag{3.8}$$

Substituting the expression for U_0 given in Eq. (3.4), the local field H_{Lp} required to reduce the barrier to a size over which a noticeable amount of flux is thermally

activated in a time $t^* = t^m$ is given by

$$H_{Lp}(T) = H_c e^{-\frac{T}{T_0}} \tag{3.9}$$

where

$$T_0 = \epsilon s \ln(t^m/t_0) \tag{3.10}$$

is the characteristic temperature associated with the time t^m.

Despite the simplicity of Eq. (3.9), a problem arises when comparing its absolute value with measurements of penetration fields because it is not expressed in terms of experimentally controllable quantities. In an experiment, it is not the local but the applied field which is controlled, usually by passing a known current through a coil wound around a sample. The field due to this current at the position where the sample will sit is calculated using the calibration constant of the coil and is thereafter refered to as the "applied field" H_a. In practice, the effective field H_L when the sample is in place will not equal H_a [41]. Hence, in order to test the relation expressed in Eq. (3.9), a model for scaling the known value of the applied field H_p to the value of the local field H_{Lp} is required.

3.2 Demagnetising Fields

The most efficient method for scaling H_p to H_{Lp} is to derive governing equations for the magnetic field in and around a general ellipsoid. When the ratio of its dimensions are taken in the various limits shown in Fig. 3.3(b), the ellipsoid can be used to model practically realisable specimens like wires, platelets, planar strips, and disks. We consider the ellipsoid shown in Fig. 3.3(a), whose magnetisation is induced by an applied field $\mathbf{H}_a$. The problem is that of finding the local field $\mathbf{H}_L$ at its surface in terms of the given applied field $\mathbf{H}_a$. The strength of the internal magnetisation vector $\mathbf{M}$ is a function of the total internal "magnetising" field $\mathbf{H}_i$. In the special case where $\mathbf{M} \propto \mathbf{H}_i$, the function $\mathbf{M}(\mathbf{H}_i)$ takes the simple form

$$\mathbf{M} = \chi \mathbf{H}_i, \tag{3.11}$$

where χ is the susceptibility. The total magnetising field inside the ellipsoid, however, has a component from both the applied field and a component, which

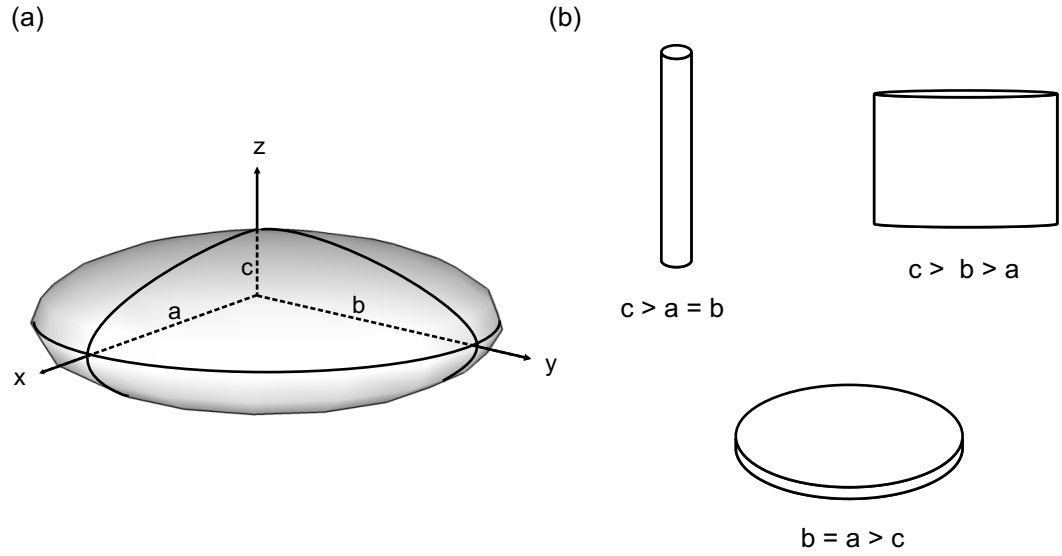

Figure 3.3: (a) Definition of the semi-axes a, b, and c of an ellipsoid (b) Wire, strip, and disk.

is called the demagnetising field, from the ellipsoid itself:

$$\mathbf{H}_i = \mathbf{H}_a - n^{(u)}\mathbf{M}, \tag{3.12}$$

where $u = x, y, z$ and $n^{(u)}$ depends on the dimensions a, b, c and the direction of the applied field. Only cases when the applied field is in the z-direction will be analysed in this work, so from now on $n = n^{(z)}$. Substituting (3.11) into (3.12) leads to the conclusion that the internal field at a point (x,y,z) inside the ellipsoid is

$$\mathbf{H}_i = \frac{\mathbf{H}_a}{1 + \chi n}, \tag{3.13}$$

which implies that, if n and χ are positive scalars, the direction of the internal field is the same as the applied field and its magnitude is scaled by a factor $1+\chi n$. The flux density $\mathbf{B}$ is defined as

$$\mathbf{B} = \mu_0(\mathbf{H}_i + \mathbf{M}). \tag{3.14}$$

By rearranging Eq. (3.14) to find $\mathbf{M}$ and substituting this into Eq. (3.12), the following relation between the fields is obtained

$$(1 - n)\mathbf{H}_i + \frac{n\mathbf{B}}{\mu_0} = \mathbf{H}_a, \tag{3.15}$$

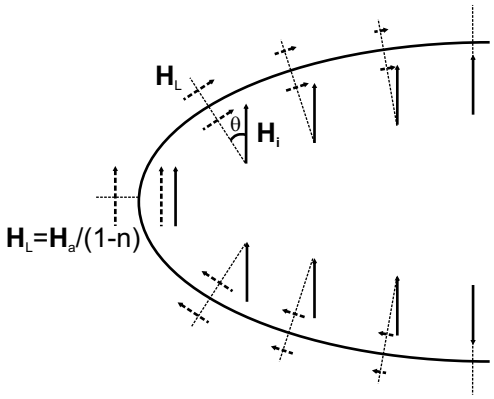

Figure 3.4: The local field at the surface of an ellipse in an applied field is the conserved tangential component of the internal field, which reaches its maximum value of $H_a/(1-n)$ at the equator.

which applies to any magnetic ellipsoid in an applied field. The ellipsoid can be made superconducting by using the defining statements that inside $\mathbf{B} = 0$. Hence from Eq. (3.15)

$$\mathbf{H}_i = \frac{\mathbf{H}_a}{(1-n)}. \tag{3.16}$$

Fig. 3.4 shows the zx plane of the ellipsoid whose internal field is given by Eq. (3.16). The appropriate boundary condition for determining the local field H_L just outside the ellipsoid is that the tangential component of the **H**-fields are conserved across its surface [42]. The tangential component of the local field is

$$H_{tL} = \frac{H_z \sin\theta}{(1-n)},$$

where θ is the angle between the surface normal and the z-axis (defined in Fig. 3.4), and H_z is the z-component of the applied field. Also, because the normal component of **B** is conserved across the surface, and internally $\mathbf{B} = 0$, then, by Eq. (3.14), the normal component $H_{nL} = 0$. Hence

$$\mathbf{H}_L = \frac{H_a \sin\theta}{(1-n)}\hat{t}, \tag{3.17}$$

where $\hat{t}$ is the unit vector tangential to the surface. An important implication of Eq. (3.17) is that, if a field H_a is applied to an ellipsoid, the local field $\mathbf{H}_L$ is tangential to the surface and exceeds H_a by a factor depending on the value of n. The value of n as the ellipsoid approaches a platelet disk with thickness d and

radius W is found by letting $a = b$ and $c \to 0$ [c.f., Fig. 3.3(b)] to obtain [41]

$$n = 1 - \frac{d}{2W}. \tag{3.18}$$

Substituting this expression into Eq. (3.17) yields $H_L = \frac{2W}{d} H_a \sin\theta$. The thermal activation of PVs will obviously initiate where H_L reaches its maximum value, which Eq. (3.17) implies will happen at the equator, where $\theta = \pi/2$. The maximum value at the edge is therefore

$$H_{edge} = \frac{2W}{d} H_a.$$

When $H_a = H_p$, the field at the edge will satisfy $H_{edge} = H_{Lp}$, and hence the final expression relating the applied field to the local field at the onset of penetration is

$$H_p = \frac{d}{2W} H_{Lp}. \tag{3.19}$$

This relation can be used to understand why the transition to the vortex state of BSCCO platelets occurs in applied fields much weaker than H_{c1}. BSCCO platelets usually have dimensions $W \approx 1000\ \mu m$ and $d \approx 10\ \mu m$, which make the aspect ratio $d/2W$ as low as 10^{-2}. Hence the local field at the equator is always much greater than the applied field, and the applied field at the transition peak is much weaker than H_{c1}, even in the presence of a BLB. By substituting the exponential dependence of H_{Lp} from Eq. 3.9 into 3.19, the following is obtained

$$H_p(T) = \frac{d}{2W} H_c e^{-\frac{T}{T_0}}. \tag{3.20}$$

which can be compared directly with values of the applied field at the penetration peak.

3.3 The Geometric Barrier

The next problem we shall consider is the distribution of flux in an ellipsoid subsequent to penetration over the BLB. Fig. 3.5 shows a flux line inside the ellipsoid, where it experiences an inward force from the local field and an outward force from the line tension. Since the local field is the force per unit magnetic "charge", the force on the vortex due to the local field is $F_{Lx} = 2\Phi_0 H_{Lx}$. The line tension

force in the opposite direction is equal to $\Phi_0 H_{c1x}$. Consequently, the flux line enters when Eq. (3.19) is satisfied, moves to a position (x, z), where these two forces balance, and gradually shifts to the centre with increasing applied field, i.e., the flux distribution is determined solely by the value of the applied field and does not depend on the magnetic history of the state. In decreasing field the relaxation of the force from the local field gives the outwardly directed line tension the advantage, and the flux line exits the sample reversibly.

Since the normal domains in the intermediate state of a type I ellipsoidal disk are subject to the same forces as quantised flux lines, they should also move in the manner just described. However, the magnetisation curves and magneto optical images obtained from experiments on thin *nearly* ellipsoidal type I disks contradicted this description of the entrance and exit of a normal domain [43, 44]. Provost *et al.* (1973) conducted an in-depth study of the intermediate state of thin lead rectangular and nearly-ellipsoidal disks and reported four major differences in the way a rectangular disk behaves in comparison to an ellipsoidal disk. Firstly, the normal domains do not cross the rectangular disk gradually, but move immediately and irreversibly to its centre at the penetration field H_p. Secondly, the field at which the normal domains move to the centre of the disk is given by $H_p = \sqrt{d/2W} H_{Lp}$, rather than $H_p = (d/2W) H_{Lp}$, where $H_{Lp} = H_C$ in type I disks because the BLB is absent [45]. Thirdly, the edge region was found to enter an intermediate state consisting of alternating superconducting/normal laminae, even before the applied field reaches H_p, which therefore does not correspond to the field of first penetration. Lastly, the magnetisation curves of type I rectangular disks exhibit hysteresis, which implies that normal domains are trapped

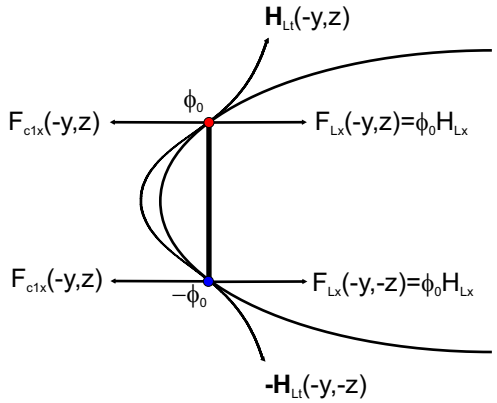

Figure 3.5: A flux line connecting magnetic poles with "charge" ϕ_0 moves to a position where the force from the local field balances the line tension.

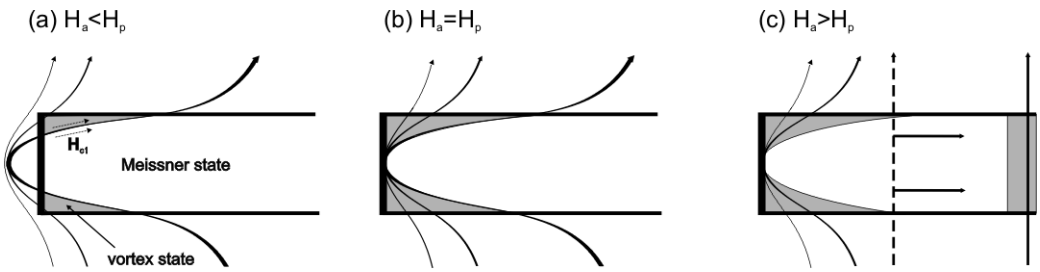

Figure 3.6: Vortex segments cuts across the corners of a disk with rectangular cross section in (a), meet at the equator in (b), and (c) moves irreversibly to the centre under the Lorentz force from the Meissner currents, forming a central core of vortices with a dome shaped field profile.

within the disk when the field is reversed.

Hysteresis in magnetisation curves shows that the entrance and exit of PV stacks in a BSCCO platelet is dominated by essentially the same irreversible behaviour [2]. A natural explanation for the irreversibility observed in both types was found by analysing the differences between the forces on a flux line in a rectangular disk in comparison to those in an ellipsoidal disk. In the rectangular disk, the highest field occurs not at the equator but at the sharp corners, where the radius of curvature is highest [41]. Hence flux lines will cut across them in short segments when the local field there is H_{Lp}, as shown in Fig. 3.6(a). When H_{Lp} is reached at the equator (i.e. when $H_a = H_p$ [Fig. 3.6(b)]), the flux lines snap free from the edge. In this scenario, therefore, H_p is still the applied field when the local field reaches H_{Lp} at the equator, where the last segment of the PV is thermally activated across the BLB. However, it no longer signals the onset of the vortex state, because it is technically present at the sharp corners. In addition, because the top and bottom surfaces of the disk are flat, there is no horizontal component of the line tension to oppose the Lorentz force. Hence at the onset field the flux line moves to the centre . As a result, flux accumulates at the centre, and the field profile across the surface exhibits a central "dome" profile Fig. 3.6(c). Upon decreasing the applied field, flux lines remain trapped within the dome at the centre until the Meissner currents reverse direction, resulting in hysteretic magnetisation. It is apparent, therefore, that when the development of the intermediate state in thin rectangular disks is compared to the ellipsoid, the extra material at the edge acts like a barrier to the entrance and exit of flux. This second barrier is therefore called the macroscopic, edge shape, or *geometric barrier* (GB).

There have been a number of theoretical studies of the GB in pin-free disks, rings [46] and strips [47, 2, 48, 4] with non-ellipsoidal cross-sections, all of which provide two major predictions. The first is an alternative to Eq. (3.19), which scales H_p to H_{Lp}. The peculiarity of the GB problem is that the development of the vortex state at the sharp corners is effectively altering the cross-section. This makes a precise calculation of the field at the equator difficult and strongly dependent on the choice of shape at the edge. For instance, Benkraouda and Clem [47] consider a rectangular strip with rounded edges and obtain

$$H_p = \left(1 + \sqrt{\frac{d}{2W}}\right) H_{Lp}. \tag{3.21}$$

Kuznetzov *et al.* [4], on the other hand, consider a straight edge which becomes progressively rounder with the field and find

$$H_p = \frac{\sqrt{\eta}}{N}\sqrt{\frac{d}{2W}} H_{Lp}, \tag{3.22}$$

where η is a dimensionless parameter and N is the enhancement factor of an ellipsoid [41]. In addition to these relations, a second prediction which can be derived from GB models involves the domelike accumulation of flux at the centre of the sample. The width and field profile of the central dome region is found to exhibit a natural dependence on the applied field and to our knowledge there have been up to five very similar predictions in various shapes and materials, for strips [47, 2], disks [46, 5] and slabs [48]. To convey the essential features of these models, we will now discuss the model presented in Benkraouda and Clem [47] for the flux dome in a pin-free strip [Fig. 3.7(b)]. In this model, the total field (H_{edge}) at the edge of the superconducting strip is enhanced by the Meissner self field induced by an applied field. In addition to this field, the flux from the central dome produces a field H_V which *subtracts* from the applied field at the edge, as is illustrated in Fig. 3.7(a). The total edge field is thus given by

$$H_{edge} = H_a + H_M + H_V. \tag{3.23}$$

It follows that when $H_{edge} = H_{Lp}$, a flux line will enter the sample. In order to calculate the exact value of the Meissner field H_M just outside the strip, it is necessary to know the precise curvature at the edge. However, it can be shown that

$$H_{Mz}(W, 0) \approx H_a R$$

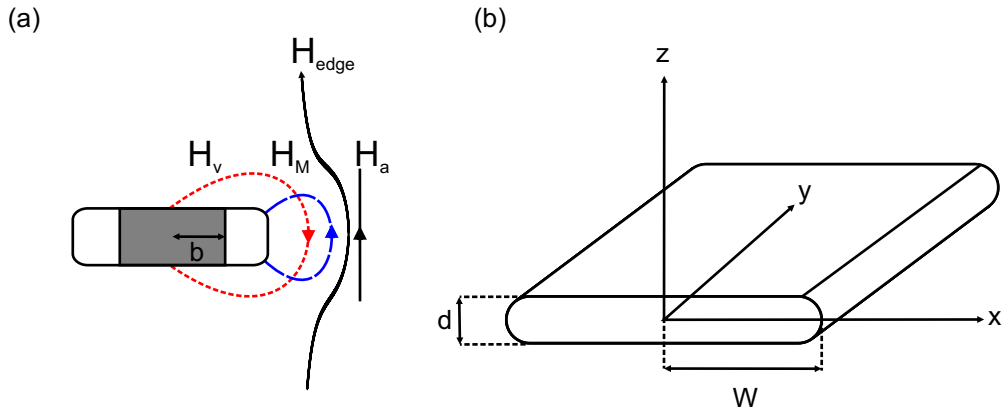

Figure 3.7: (a) The total field at the edge (H_{edge}) in the presence of vortices is given by the sum of the vortex return flux (H_V) from the dome (half-width b), the Meissner field (H_M), and the applied field (H_a). The condition which must be satisfied for a vortex to enter the strip is then that $H_{edge} = H_{Lp}$. (b) The geometry of the infinite strip used by ref. [47] to calculate the radius of the central flux dome.

is a good approximation of the Meissner field at the edge, where $R = \sqrt{2W/d}$. The second term, H_V, due to the flux dome is given by [47]

$$H_{Vz}(W,0) = -\frac{R}{\pi\mu_0 W}\int_{-W}^{+W} dx' B_z(x')\sqrt{\frac{W+x'}{W-x'}},$$

where $B_z dx'$ is the flux density per unit length in the dome and in a strip is given by the function

$$B_z(x) = \mu_0 H_a \sqrt{\frac{b^2 - x^2}{W^2 - x^2}}, \tag{3.24}$$

where b is the half-width of the flux dome. Collecting terms together, the condition for the entrance of a vortex is given by

$$H_{edge} = H_a + H_a R - \frac{R}{\pi\mu_0 W}\int_{-W}^{+W} dx' \mu_0 H_a \sqrt{\frac{b^2 - x'^2}{W^2 - x'^2}}\sqrt{\frac{W+x'}{W-x'}} H_V = H_{Lp}.$$

This condition is only satisfied if the width b and the applied field H_a are related by

$$H_a = \frac{H_{Lp}}{1 + R\sqrt{1-(b/W)^2}}. \tag{3.25}$$

Figure 3.8(a) illustrates the flux density field profile given by Eq. (3.24) for several values of the applied field above the penetration field. The value of b used at each field is calculated using Eq. (3.25). It can be shown [47, 2] that the magnetisation of the strip after penetration is inversely proportional to the

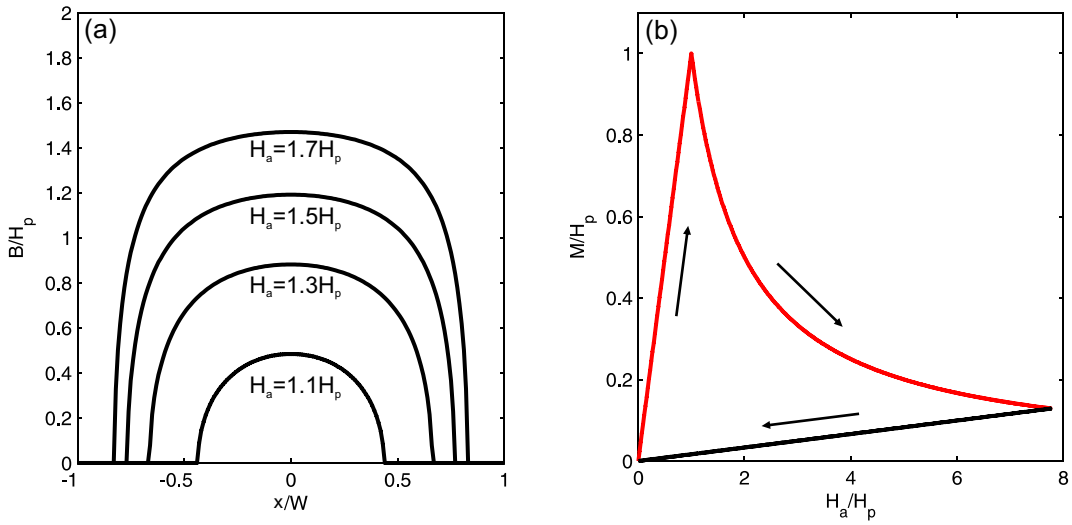

Figure 3.8: (a) Normalised flux density profile across a strip for several applied fields after penetration. The half-width b of the dome shaped profile is given by Eq. (3.25). (b) The magnetisation of the strip as a function of the applied field in increasing (red) and decreasing (black). Arrows indicate the direction in which the applied field is changing.

applied field $M \approx -H_p^2/H_a$, as shown by the red curve in Fig. 3.8(b). When the field direction is reversed and the field reduced, however, the magnetisation traces the black curve in Fig. 3.8(b). This irreversibility is a direct consequence of the screening currents at the edge, which continue to circulate in the same direction and thus prevent vortices from exiting the disk. Although the number of vortices within the dome remains approximately constant, the size of the dome increases, leading to a reduction in the vortex density. As a result, the magnetisation is a relatively weak linear function of decreasing field. It is not until the field reverses direction that the vortices are able to exit [2].

Although the BLB and GB are both surface barriers, it is important to emphasise some of their differences. Firstly, with regards to the delay of flux entry, the GB could equally be called an "enhancement factor reduction" effect because it reduces the field at the edge in comparison to an ellipsoid, as can be seen from Eqs. (3.21) and (3.22). If, for example, a local field of 100 Oe is required to surmount the BLB at a given temperature, then a field of 1 Oe applied to an ellipsoid with an aspect ratio of 100 will be enhanced by a factor of 100, and 1 Oe will consequently be the observed penetration field. By constrast, if a field of 1 Oe is applied to a rectangular disk, then only the corners will be penetrated and it is not until a much higher field of $100/\sqrt{100} \approx 30$ Oe is applied that the local field at the equator reaches 100 Oe and a flux line is able to surmount the

BLB. Hence it is only in *comparison* to an ellipsoid that an applied field of 30 Oe is "high", the cause of which is therefore said to be a "barrier". While both the GB and BLB require the applied field to be higher in an arbitrary geometry than in a barrier free ellipsoid, they thus do so for very different reasons. The BLB requires a higher field in order to enhance the field locally, whereas the GB requires a higher field simply to compensate for the loss of enhancement factor. Another important distinction between the two models is that GB models predict a relation between the *applied* field at penetration (H_p) and the first critical field H_{c1}, while the BLB model predicts a relation between the *local* field at penetration (H_{Lp}) and H_{c1}. Hence predictions for the GB model in the absence of the BLB are straightforward to investigate as they can be compared to experimental values of the applied field directly. The BLB on the other hand always requires a choice of geometry to scale H_{Lp} to H_p.

For vortex lines in an isotropic superconductor, the GB and the BLB are geniunely separable phenomena and the predictions for H_p at different temperatures can be compared to determine the dominant barrier. Wang *et al.* [9] recently conducted a study of the penetration field for BSCCO disks with rectangular cross section and concluded that the theoretical predictions of GB models severely underestimate the penetration fields at intermediate temperatures. This falsification of the GB models means that, even when the field is sufficient to compensate the lower non-ellipsoidal enhancement factor due to the GB, the BLB dominates and prevents PVs from entering until a higher field. However, it is far from obvious whether in BSCCO the BLB and GB are separable phenomena for the case of PVs entering the sharp corners of a platelet exhibiting the strong anisotropy seen in BSCCO. The BLB models presented in Burlachkov *et al.* and Kopylov *et al.* are predicated on the assumption that single PVs initiate the entrance of an entire stack [39]. Hence the idea that a segment of PVs penetrates at the corners, without avalanching the remaining pancakes, appears to contradict this fundamental requirement of the BLB theory.

3.4 Mesoscopic superconducting disks

In a superconducting micro-disk with dimensions comparable to a single vortex, the screening currents interact so strongly with the vortex currents that it is invalid to assume that the stable vortex configuration within the dome at the centre is a symmetrical triangular lattice. Both simulations [11] and magnetic imaging techniques [12] have shown that at low fields, when there are only a few vortices present, vortex clusters (regular polygons with one vortex at each vertex) are favoured over the regular triangular ordering. As the number of vortices grows, they arrange in concentric rings with each new ring forming at critical or "magic" vortex numbers, the first few of which are depicted in Fig. 3.9(a). Bitter decoration, scanning SQUID magnetometry, and SHPM images of vortex shells have been obtained in Nb and YBCO polygons patterned from thin films [12, 13, 14]. One striking consequence of these configurational changes is a discontinuous evolution of the magnetisation [49] with the applied field. These discontinuities arise because, unlike the closely spaced continuum of magnetisation states observed in macroscopic samples, the relative positions of vortices at vorticity L produces a characteristic value of the magnetisation that can be very different from the next $(L+1)$ configuration. As a result, an addition (subtraction) of a vortex causes abrupt increases (decreases) in the magnetisation, such as those illustrated in Fig. 3.9(b). Since these features cannot be derived from continuum models such as the geometric barrier, in the mesoscopic regime it is necessary to obtain the magnetisation and flux distribution using methods which directly account for the spatial discretisation and topological confinement of magnetic flux.

A method which is commonly used to determine the vortex configuration in a given applied field is to solve the GL equations subject to appropriate boundary conditions on the superconducting wavefunction, ψ, at the edge of the disk. Besides the locations of the vortex cores, which are found from the points where ψ is zero, important quantities such as the current distribution and local magnetisation can also be derived [11, 50]. However, since the characteristic lengthscale ($\xi \approx 10$ nm) of the grid on which variations in ψ must be discretised is two orders of magnitude smaller than a large mesoscopic BSCCO disk (≈ 5 μm), the numerical solution of the complete GL equations in 3-D is computationally very expensive. To remedy this, vortex configurations can instead be calculated in the so-called London limit [51, 6, 52], where $\psi = 1$, except at the singularities of the vortex cores where it falls to zero. In that case, vortex cores can then be approx-

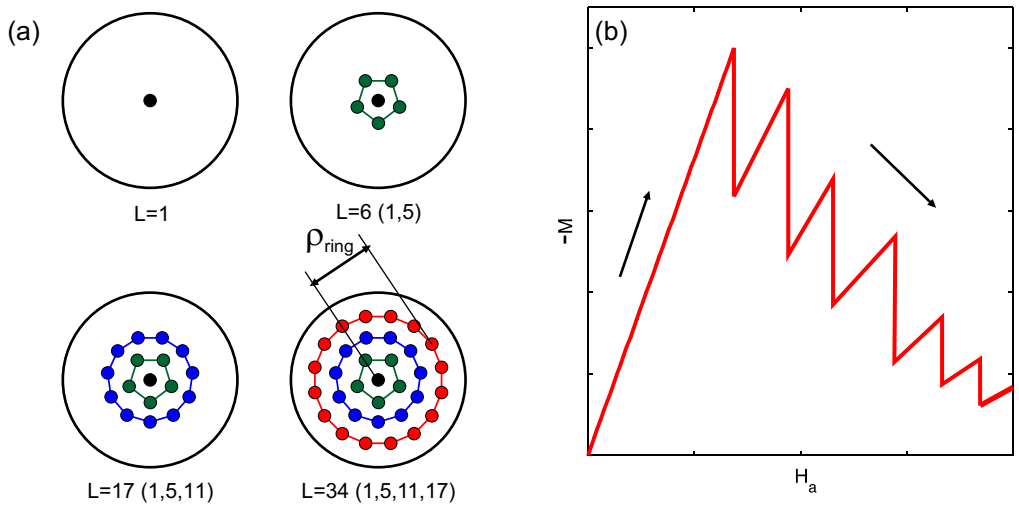

Figure 3.9: (a) Vortices in a mesoscopic superconducting disk form concentric shell structures, with each new shell forming at the "magic" numbers L = 1,6,17,34. The numbers in brackets below each structure indicate the occupancy of each shell at the transition point. ρ_{ring} refers to the discrete radius of the ring encircling the outermost shell. (b) Schematic representation of the magnetisation of a mesoscopic disk in increasing field. Vertical transitions correspond to the entrance of a vortex.

imated by mutually repelling point particles, whose dynamics can be simulated using molecular dynamics simulations. In this work, the method presented by Cabral *et al.* [6] is used to arrive at the London expressions for the total force on vortices within a large mesoscopic disk. We start with the total free energy of a superconducting disk containing L vortices in the limit of large κ [6]

$$G_L = \sum_{i=1}^{L} \left(\epsilon_i^S + \sum_{j=1}^{i-1} \epsilon_{ij} \right) + \epsilon^{core} + \epsilon^{field}. \tag{3.26}$$

Each term ϵ of this expression represents an energy contribution of different origin and the index i refers to the i-th vortex within the disk. The first term represents the total potential energy of the confined vortices and is divided into two further contributions:

$$\epsilon_i^s = \epsilon_i^{self} + \epsilon_i^{shield},$$

where ϵ_i^{self} is the interaction energy between the vortex with its image and ϵ_i^{shield} is the interaction with the edge current. It can be seen that these two quantities are equivalent to those derived earlier in the context of the Bean-Livingston barrier at the infinite half-plane [section (3.1).] In the present case, where the finite size has a defining influence on the vortex behaviour, the two energies are given

instead by

$$\epsilon_i^{self} = \left(\frac{2}{W}\right)^2 \ln(1 - r_i^2)$$

$$\epsilon_i^{shield} = -2H_0(1 - r_i^2),$$

where W is the radius of the disk, $r_i = \rho_i/W$ is the distance of the vortex core normalised to the disk radius, and $H_0 = H_z/H_{c2}$ is the applied magnetic field normalised to the second critical field ($H_{c2} = \Phi_0/2\pi\xi^2$). The second term in the summation of Eq. (3.26) accounts for the dipole-dipole interaction energy between the i-th and j-th vortex and is given by

$$\epsilon_i^{self} = \left(\frac{2}{W}\right)^2 \ln\left[\frac{(r_i r_j)^2 - 2\mathbf{r}_i \cdot \mathbf{r}_j + 1}{r_i^2 - 2\mathbf{r}_i \cdot \mathbf{r}_j + r_j^2}\right].$$

The final two terms of Eq. (3.26) account for the energy of the vortex core,

$$\epsilon^{core} = \left(\frac{2}{W}\right)^2 L \ln(R/a),$$

and the energy of the field

$$\epsilon^{field} = W^2 H_0^2/4.$$

We obtain the total force on the k-th vortex by taking the spatial gradient of the energy

$$\mathbf{F}_i = -\nabla_k G_L(\rho_i, \rho_j),$$

where ∇_k is the gradient with respect to the coordinate ρ_k. The force per unit length can then be expressed in units of $H_c^2\xi/8\pi$ as the sum of two terms

$$\mathbf{F}_i = \mathbf{F}_i^s + \sum_{k=1}^{L} \mathbf{F}_{i,k}^{int}. \tag{3.27}$$

The first term is the total force on the i-th vortex arising from the repulsion from the edge currents and the attraction to the image antivortices, and is given by

$$\mathbf{F}_i = \left(\frac{2}{W}\right)^3 \left(\frac{1}{1 - r_i^2} - \frac{H_0 W^2}{2}\right) \mathbf{r}_i, \tag{3.28}$$

whilst the second term represents the total intervortex repulsion, and can be expressed as

$$\mathbf{F}_{i,k}^{int} = \left(\frac{2}{W}\right)^3 \left(\frac{\mathbf{r}_i - \mathbf{r}_k}{|\mathbf{r}_i - \mathbf{r}_k|^2} - r_k^2 \frac{r_k^2 \mathbf{r}_i - \mathbf{r}_k}{|r_k^2 \mathbf{r}_i - \mathbf{r}_k|^2}\right). \tag{3.29}$$

The conventional routine for calculating the vortex configuration at a given applied field involves initialising a large number of vortices at random positions within the disk, calculating the force on each vortex using Eqs. (3.27-3.29), and calculating their new positions from $\eta d\rho_i/dt = \mathbf{F}_i$, where the viscous drag coefficient, η, is obtained using the field-dependent Bardeen-Stephen expression [53]. Vortices within a coherence length of the disk boundary are removed in order to avoid energy contributions which diverge when a vortex is at the edge, and the simulation is terminated either when the difference in energy between two consecutive configurations is below a threshold value, or 2×10^6 time steps have been performed. The routine is then repeated for each applied field and the final configuration is chosen to be the ground state for that field. The key modification implemented in the present work is to use the previous configuration as the initial configuration for each successive value of the applied field. This modification is obviously not suitable when the applied field is increasing, since it is not possible for vortices to enter the disk, but accurately imitates the situation where vortices exit in decreasing field.

In order to relate the vortex configurations to a measurable quantity, vortex fields can be integrated at a height of z through a square area above the disk. The local surface field or "local" magnetisation calculated in this manner closely corresponds to the field that would be measured by a local magnetic probe. The combined field from all vortices is calculated by approximating the field distribution of each vortex by a point monopole placed $z + \lambda_{eff}$ below the probe. The vertical component of the field from the i-th vortex is given by

$$B_i(r, z) = \frac{\phi_0}{2\pi} \frac{z + \lambda_{eff}}{[\rho_i^2 + (z + \lambda_{eff})^2]^{3/2}},$$

where the ρ_i are obtained from the MD simulations.

Chapter 4

Experimental Techniques

There are a number of techniques for measuring the stray magnetic fields at surfaces, namely electron microscopy, magnetic force microscopy (MFM), Bitter decoration, Scanning Hall probe microscopy (SHPM), magneto-optical imaging (MOI) and scanning superconducting quantum interference device (SQUID) microscopy. For a review of the main techniques for magnetic imaging of flux structures in superconductors, the reader is referred to [54]. Here the exposition is restricted to an overview of Hall probe magnetometry and microscopy (SHPM) and MOI, as the conclusions in this thesis are primarily based on results from these two techniques.

4.1 Hall Probe Magnetometry

The Hall effect is the name given to the transverse voltage which develops across a current carrying specimen when placed in a perpendicular magnetic field. This voltage, first observed in 1879 in a strip of Gold leaf by its discoverer Edwin Hall [55], is found to be proportional to the product of the magnetic flux density B and the longitudinal transport current:

$$V_H \propto I_H B \tag{4.1}$$

where the directions of B, V_H, and I_H are related as in Fig. 4.1. V_H results from

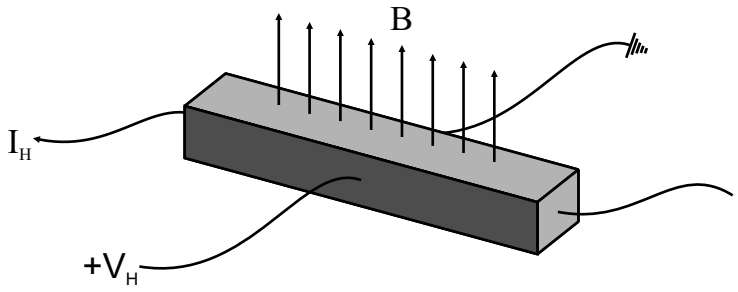

Figure 4.1: The Hall effect. A transverse voltage V_H is induced in a conductor carrying a current I_H in a magnetic field B.

the electric field between the charge carriers forced to one side of the specimen by the Lorentz force. Of relevance to the present work is the proportionality between the Hall voltage and the magnetic field. This relation allows one to use the Hall effect as the operating principle of a field to voltage transducer, or *Hall probe* (HP), which can be fabricated with sub-micron dimensions to measure the surface fields of individual vortices in superconductors.

Since the intensity and characteristic lengthscale for spatial variation of the magnetic fields of vortices is small, a theoretical analysis of the Hall effect is important for understanding the factors which control the choice of material and geometry for a suitable HP. Hence we now relate the parameters associated with the material, such as the concentration and sign of its charges, to the sensitivity of the HP in an ideal "cross" shape, illustrated in Fig. 4.2(a). The horizontal bar will be refered to as the Hall current lead and the vertical bar as the Hall voltage lead. We consider a current with density J_y flowing from left to right and a magnetic field directed out of the plane. A magnetic field in the vicinity of the leads causes a voltage to develop across the voltage leads. The force on the charges in the Hall cross due to a field $\mathbf{B} = \hat{z}B_z$ and electric field $\mathbf{E} = \hat{y}E_y$ is given by

$$\begin{aligned} \mathbf{F} &= q(\mathbf{E} + \mathbf{v} \times \mathbf{B}) \\ &= q[\hat{x}(E_x + v_y B_z) + \hat{y}(E_y)], \end{aligned} \tag{4.2}$$

where v_y is the drift velocity of the charge carriers with charge q. The charge carriers will stop moving in the x direction when the first term is zero. Hence the condition for dynamic equilibrium is

$$E_x = -v_y B_z. \tag{4.3}$$

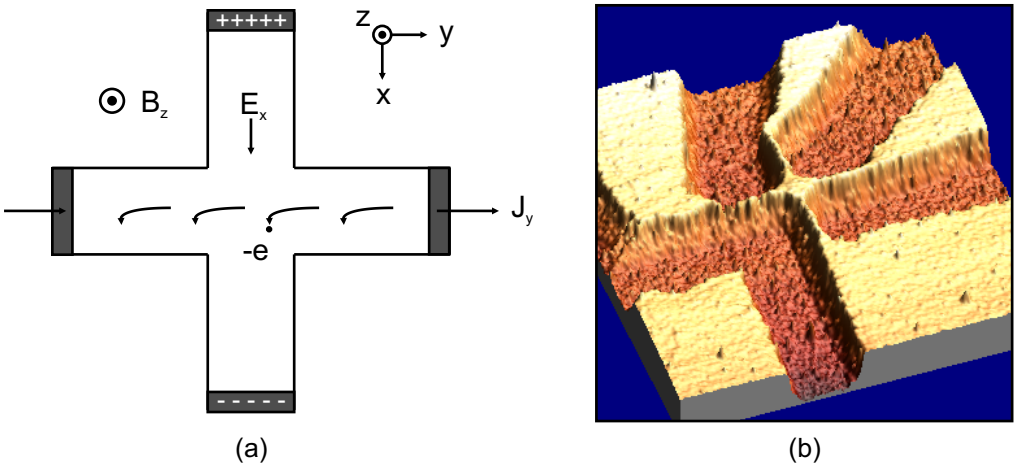

Figure 4.2: (a) An idealised cross shape of a Hall sensor. (b) AFM image of a HP with an active flux sensing region of 5 μm.

The term E_x on the left is the Hall field between the charges which are separated by the Lorentz force qv_yB_z. For electrons with $q = -e$ and $v_y = -v_y^e$, the transverse acceleration due to the Lorentz force is in the positive x direction and the electrons accumulate on the lower side of the voltage lead, as depicted in Fig. 4.2(a). The Hall field in Eq. (4.3) then yields a force in the negative x-direction to balance the Lorentz force. To relate this result to the current, the current density is expressed as $J_y = nqv_y = nev_y^e$. Therefore

$$E_x = -\frac{J_y}{ne}B_z.$$

Inspecting the terms of this equation, it can be seen that it is equivalent to the empirical relationship in Eq. (4.1). Hence for a given material the current density, the magnetic field and the Hall field are fixed by the following relationship

$$\frac{E_x}{J_yB_z} = -\frac{1}{ne} = R_H, \tag{4.4}$$

and this constant is called the *Hall coefficient*. Since a large R_H implies that a greater voltage is produced for a given applied magnetic field, it is a figure of merit for the Hall sensitivity of the material.

To measure the stray fields at a surface, the Hall voltage V_H corresponding to the field E_x in Fig. 4.2(a) can be measured while a HP is either actively scanned across it, giving rise to the technique of scanning Hall probe microscopy (SHPM),

or fixed in place, as in local HP magnetometry. In both these approaches, the smallest measureable magnetic feature is determined by the size of HP's field sensitive ("active") region and the minimum detectable field is set by the Hall coefficient R_H. The earliest HPs used to investigate superconductors were fabricated from Gold. Significant gains in sensitivity are achieved by using lower carrier concentration materials. The semimetals, such as Bismuth [56], and semiconductors, such as Si doped GaAs [57], were the next obvious choice for HP materials. However, the gains in sensitivity achieved using low carrier concentration materials are soon compromised by their higher resistivity, which results in increased Johnson noise and lower signal-to-noise ratio (SNR) with decreasing size of the active region.

Over the last few decades the major advance in sub-micron resolution Hall sensing technology has come with the invention of modulation doped semiconductor heterostructures. These structures contain a very low (10^{15} m^{-2}) concentration two dimensional electron gas (2DEG) trapped at the interface between two lattice matched semiconductors. The high mobility, low resistivity, and SNR in the 2DEG is nearly constant with temperature, making them ideal for imaging the small vortex exit fields from both HTSs and conventional superconductors. In addition, since they are grown in the form of semiconductor wafers, they are easily patterned into a small Hall sensor shape using well established lithographic techniques.

The reader is refered to the extensive literature on the subject for detailed information about the physics of 2DEG systems. It is sufficient here to examine the structure itself, for this gives it the physical properties relevant to Hall probe applications. The growth of the AlGaAs/GaAs heterostructure by molecular beam epitaxy was reported by Dingle *et al.* [58] in the context of its unusually high carrier mobility. The physical structure along with a schematic band diagram is shown in Fig. 4.3. Due to the lattice structure and low carrier concentration of GaAs, the Fermi energy resides in the range of forbidden electron energies. Hence there are no electrons in the conduction band at low temperatures. When AlGaAs is grown epitaxially on GaAs, the electrons from the Si donor atoms in the n-AlGaAs are thermally excited, leaving the positive charge of the Si ions uncompensated. The electrostatic potential from these ions creates a potential well at the AlGaAs/GaAs interface, where the electrons are confined to flow in two dimensions. Obviously the distribution of the electrons determines the potential

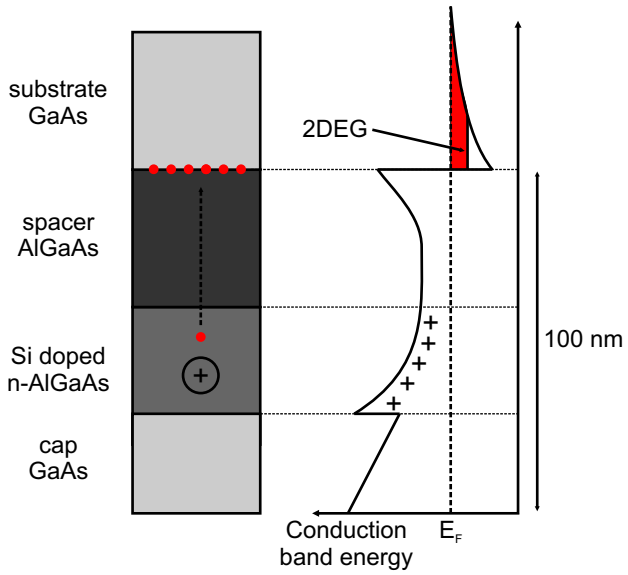

Figure 4.3: Layering and schematic band structure of GaAs/AlGaAs heterostructure used to fabricate micro-Hall probes.

landscape and the potential landscape determines the distribution of electrons, so a precise calculation of these effects must be self-consistent [23]. The band diagram shown in Fig. 4.3 illustrates the main results of this more precise calculation. The Fermi energy E_F must be the same throughout the structure because the electrons are in equilibrium. The effect of the charge landscape is to 'bend' the energy of the conduction band, eventually bringing it below the Fermi energy near the interface. The most energetic electrons will then have access to the conduction band, though only in the narrow region at the interface. The electrons at the interface are separated from the Si donor ions in the n-AlGaAs by the spacer AlGaAs layer, which reduces the scattering from impurities that normally dominates the electron mobility at low temperature. This separation between the donor atoms and the 2DEG, a technique known as modulation doping, is the key to understanding its high carrier mobility. The specific density of electrons and currents in 2DEGs refers to a surface area, so the Hall coefficient derived in the previous section takes on a slightly different meaning known as the Hall resistance given by

$$R_H = -\frac{1}{n_{2D}e}.$$

Due to the discovery of the high temperature superconductors coinciding with the development of modulation doped semiconductor heterostructures, 2DEG micro-Hall probes have played a pivotal role in determining the magnetic properties of HTSs. Single AlGaAs/GaAs HPs are ideal for measuring the local surface field

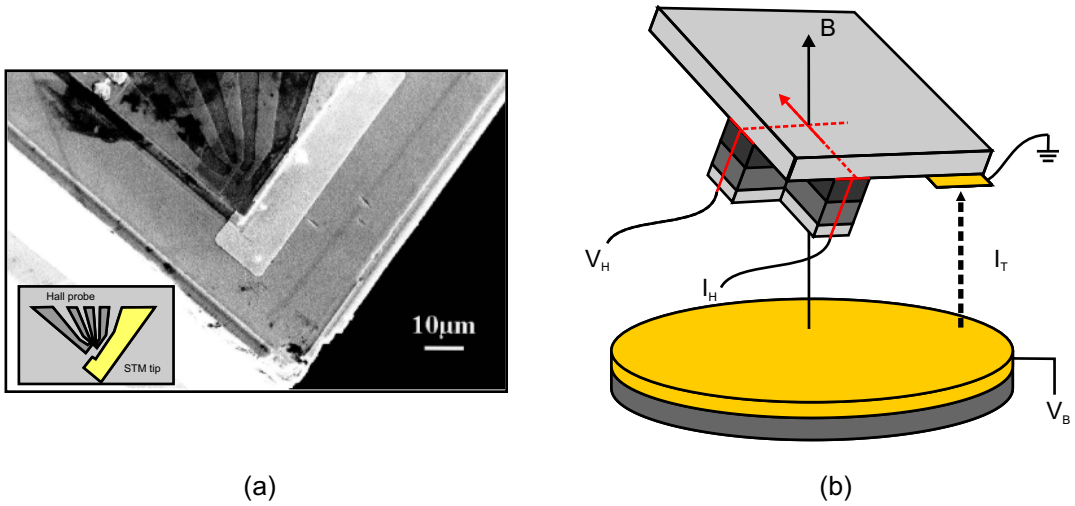

Figure 4.4: (a) Electron micrograph of a SHPM chip. (Reproduced from [54].) (b) Schematic representation of the HP and the STM tip during operation of the SHPM chip.

at one location, but modest spatial resolution can also be obtained by fabricating linear arrays of Hall probes which measure the fields separated by some tens of microns. Linear arrays have been used to measure the fields across BSCCO single crystals [2]. The fabrication of Hall probes for SHPM chips from 2DEG wafers involves conventional optical and electron beam lithography techniques. The reader will find a comprehensive treatment of the procedure in [59]. The basic procedure involves etching away the Si doped n-AlGaAs layer everywhere except along narrow channels, so that the 2DEG current is forced to flow through an active HP region. Ohmic contact to the 2DEG is achieved through annealing Au/Ge pads which are deposited on the GaAs surface.

There are currently two well known implementations of *scanning* HP systems. The HP can be mounted to the head of an insert to a crysotat and moved towards and over the sample surface by stepper motor controlled stages, or by a segmented piezoelectric tube that can be moved laterally by applying high voltages to opposite segments. The spatial resolution of the mechanical system is usually coarse ($\approx$ 1 μm), but recent work by Dinner *et al.* [60] has achieved sub-micron resolution whilst scanning over centimetres of sample surface. The piezoelectric implementation uses an approach mechanism based on conventional scanning tunnelling microscopy, where a tunnel current is used to determine the distance to the surface. Fig. 4.4(a) shows a SEM image of an SHPM chip with a gold film that acts as an integrated STM tip. The tip is earthed and the sample is biased, giving rise to a tunnel current I_T whose strength can be used to determine

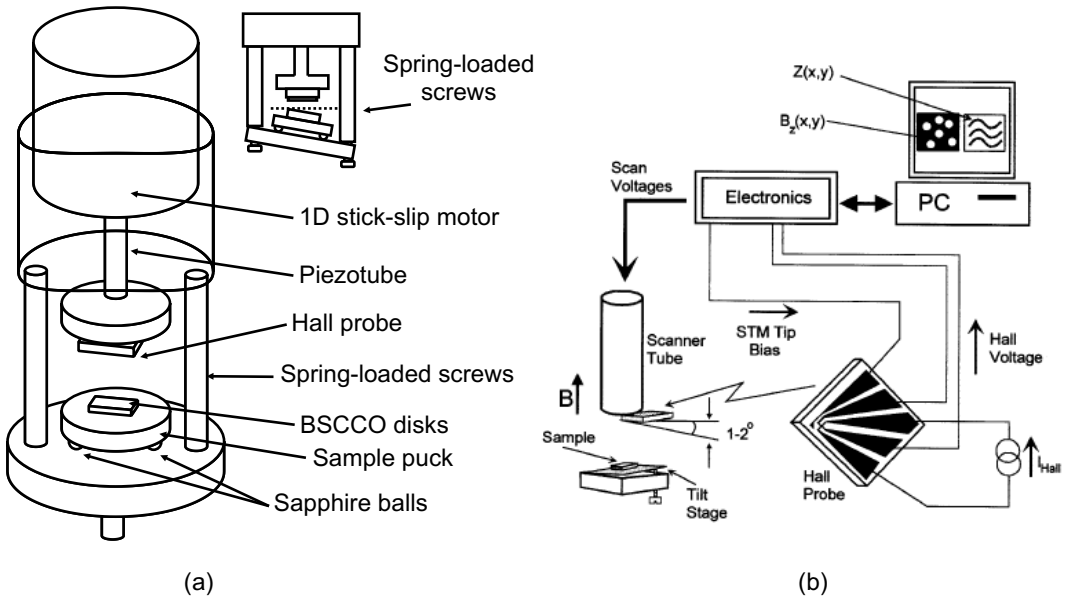

Figure 4.5: (a) Schematic of the head of the SHPM. The inset diagram illustrates the angle between the HP and the sample surface. (In reality there are three screws to adjust the angle.) (b) Schematic of the SHPM.

the distance from the surface [see Fig. 4.4(b).]

For successful operation, SHPMs demand careful consideration of the position and orientation of the sample prior to scanning. Fig. 4.5(a) shows a diagram of the head of the microscope and a schematic of the whole apparatus is shown in Fig. 4.5(b). The sample was fixed to the "puck" shaped sample holder of the SHPM using silver paint, which also provides the electrical contact required to bias the sample surface for tunnelling. The puck was then mounted to the sample stage and the active area vertically aligned with the HP under an optical microscope. Three sapphire balls seated underneath the puck allow the sample to be manouvered into position. The puck was fixed firmly in place to prevent relative motion of the sample and sensor during the insertion of the microscope into the liquid nitrogen cryostat. Once the HP was aligned to the sample, the angle between the planes of the HP and the sample surface was set to around 1°; larger than this and the active HP region would be too far from the surface when the tip is in tunnelling contact, whilst smaller than this and there is a risk of crashing the HP into the surface before tunnelling.

The angle was adjusted at room temperature by tightening the three spring-loaded screws which tilt the sample stage [see inset to Fig. 4.5(a).] At room

temperature, the sample was moved close to the HP until its reflection was seen in the sample surface. The reflection allows one to assess the size of the angle, which can be adjusted by backing off the sample and adjusting the screws appropriately. For low temperature work the microscope insert sits in the sample space of a LN_2 cryostat. The whole setup was cooled in the Earth's field to 77 K and the HP is approached into tunnelling contact with the sample surface using a stick-slip motor. The threshold tunnel current is set to 0.2 nA and the sample bias voltage to 0.2-0.8 V. Once the tunnel current reaches the threshold, the HP is backed off and the edges of the scan area are checked for tunnelling. If tunnelling contact is found at this stage, the HP was backed off until the probe could safely scan without tunnelling. This means that the actual working distance of the HP varies between experiments and was typically $\approx$ 100 nm - 500 nm.

4.2 Magneto-Optical Imaging

The second technique which was used in this work to measure the stray fields at a surface exploits the Faraday effect. The Faraday effect consists of a rotation of the plane of polarisation of light as it passes through a medium in a magnetic field applied parallel to the direction of propogation. It was first observed by Faraday in 1845, when he passed light from a flame through lead borate glass placed between the poles of an electromagnet [61]. Fig. 4.6(a) illustrates the important features of the Faraday effect. A ray of linearly polarised light with wavevector k passes through a magnetically active medium with length d. Around the medium is a coil that produces a magnetic field at the location of the ray and in the same direction. If the field has magnitude B, then experimentally one finds that the angle of rotation is proportional to the product Bd and is in the direction of the current. The constant of proportionality is called the *Verdet* constant V of the medium and is defined by

$$V = \frac{\theta}{Bd}.$$

A practical implication of this empirical formula is that a measurement of the rotation of the light from a location in an optically active medium will also be a measure of the intervening magnetic field, and that the light will develop a greater rotation for a given field if the material is thick and has a high Verdet constant. Hence the Verdet constant is the figure of merit for the sensitivity of the Faraday effect. In reality the setup shown in Fig. 4.6(a) is impractical for

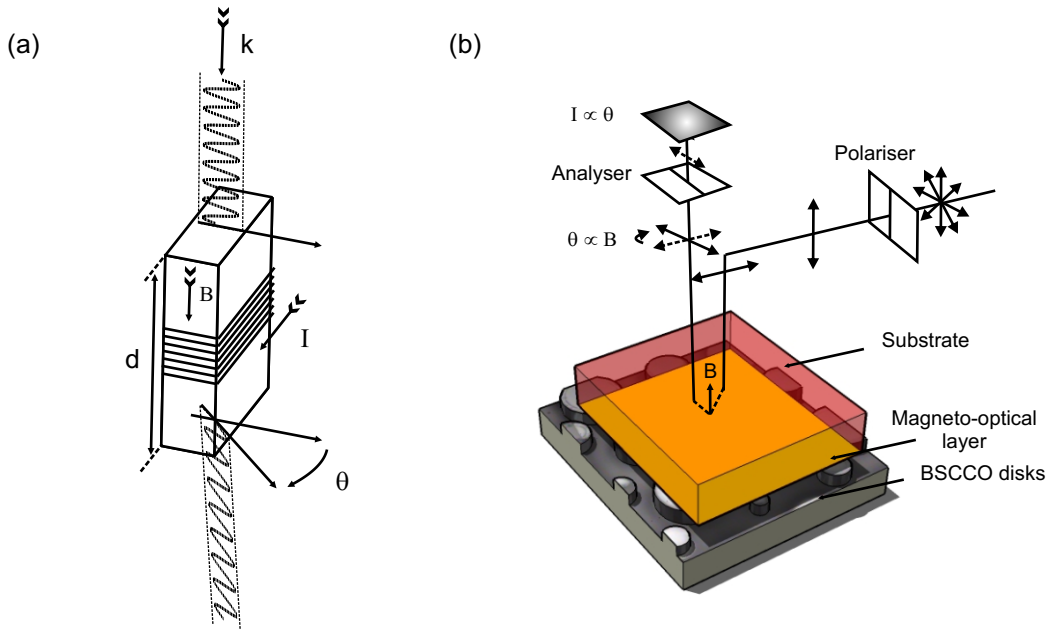

Figure 4.6: (a) The Faraday effect. The polarised light with wavevector k is incident from the top. The current through the coil around the optically active medium produces a magnetic field B which rotates the polarisation of the light by an angle θ. (b) Illustration of the magneto-optical Kerr effect used to measure the stray field at the surface of the disk array. The incident light is polarised before being reflected by a mirror (not shown) onto the sample surface where it interacts with the stray magnetic flux in the MOL from the disk array. After reflection from the surface, the analyser, which is set perpendicular to the polariser, passes the component of the light which was rotated at the surface.

measuring surface fields because it relies on the passage of light through a transparent medium. In this work the setup shown in Fig. 4.6(b) is employed instead. This configuration is technically called the magneto-optical Kerr effect because the light is reflected rather than transmitted [62]. An optically active medium, refered to as the magneto-optical layer (MOL) of the substrate, is brought into intimate contact with the sample's surface. A metallic film, deposited on the side in contact with the sample, acts as a mirror. Light is passed through a polarising filter and directed onto the garnet, where the rays interact with the stray magnetic fields which pass through the MOL. After reflection from the mirror layer, the rays are sent through an analyser. If the polarisation of the analyser is set perpendicular to the original polariser, the light that emerges from the system must have been rotated at the surface with intensity θ. Since θ is approximately proportional to B, the intensity image corresponds to the spatial distribution of the stray magnetic fields from the sample.

The application of the MOI technique to examine the magnetic fields from su-

perconductors in the intermediate state was first demonstrated in 1957 by Alers [63] who successfully imaged the surface field from normal regions of a large lead alloy disk using a paramagnetic salt as the MOL. In comparison with other magnetic imaging techniques at the time, MOI suffered from low sensitivity to weak magnetic fields. The spatial resolution, limited to around 0.25 mm, was comparable to contemporary SHPM [56]. A major breakthrough in field resolution came with the investigation of the europium chalcogenides, discovered and employed as MOLs from the 1970's, which have Verdet constants two orders of magnitude greater than the paramagnetic salts [64]. They can also be grown in thin films, making it easier to bring them into close contact with the sample surface. However, these materials only function well at low temperature, so their application has been limited to the conventional low temperature superconductors and recently the material of choice has become the Bi-doped Yttrium Iron Garnet (Bi:YIG) or Bismuth ferrite garnet films (FGF).

In this work, the sample was cooled below T_c and imaged using a low-temperature MOI system based on a cryocooler. The Si chip with the BSCCO disk array[1] was fixed with Apiezon grease to a copper sample puck. The inset to Fig. 4.7 shows how the Bi:YIG garnet is carefully placed over the sample and copper leaf springs either side tightened until the garnet is held firmly in place and the leaf springs were noticably curved. The natural height of the leaf springs was adjusted with the use of a suitable copper spacer in order to avoid damaging the sample with excessive pressure. Care was also taken to avoid bumps on the sample surface, as these were found to cause distortions in the garnet which produce spurious changes in the magneto optical contrast with applied field. The sample puck was fixed to the copper cold head of the cryocooler and partially covered by a copper radiation shield. A schematic of the sample chamber is shown in the main diagram of Fig. 4.7. Optical access to the polarised light is acheived through a window in the top of the sample chamber of the cryocooler. A heater and temperature sensor attached to the cold head was used to set and control the temperature between 30 K and 90 K. The angle between the polarisation of the analyser and polariser was adjusted until the light was extinguished and then a CCD camera was attached to the microscope. The camera was then directly connected to a PC, allowing the use of powerful image acquisition software for viewing, capturing and averaging the images. The software operates by binning each pixel from the CCD in one of 4096 intensity levels distributed between the maximum and

[1]See appendix (A) for details of the sample.

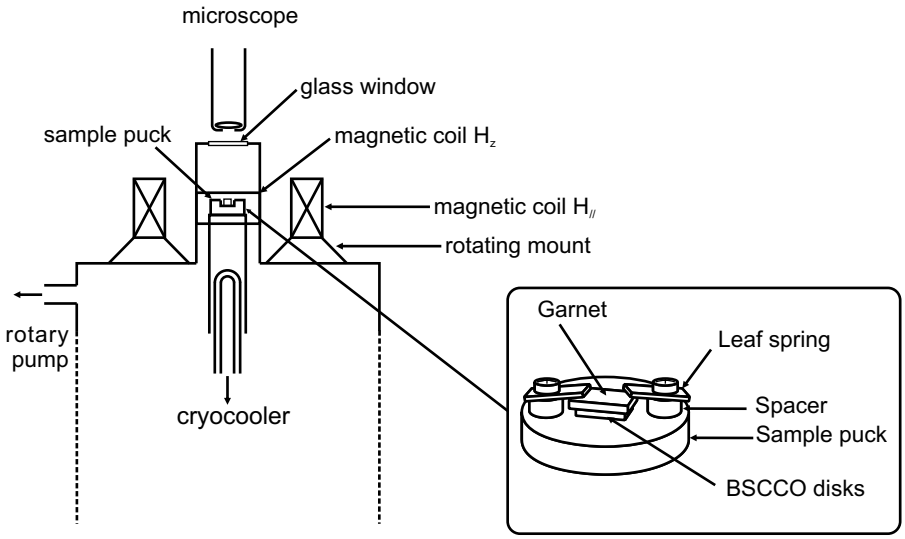

Figure 4.7: Schematic of the sample chamber of the cryocooler MOI system. The inset diagram shows how the sample and garnet are brough into contact on the sample puck.

minimum intensities, both of which are controlled by the relative angle between the polariser and analyser. This angle was fine tuned using an electronically controlled stepper motor to find the strongest contrast in "difference" images, i.e., images produced by subtracting two raw images captured under different applied fields. Difference images enable one to discern much subtler changes in the flux distribution because they remove features unrelated to the influence of the applied field on the sample, such as scratches and domain patterns in the garnet. An out-of-plane field H_z was applied using a copper coil wound directly around the sample and powered using a manually controlled power supply. A pair of external Helmholtz coils mounted on a rotating stage was used to apply an in-plane field at the same height as the sample. It was generally always necessary to work with a small in-plane field to saturate the domains in the MO garnet. After the fields were applied, the exposure time of the CCD was set to between 50 and 100 ms and the image averaged between 300 and 500 times, depending on the image quality and contrast. The out-of-plane field was then set to a new value and the measurement repeated, with each image taking approximately 10 minutes to acquire and process.

Chapter 5

Magneto-Optical Imaging of Flux Penetration into Arrays of BSCCO Micro-disks

5.1 Introduction

The interior of a bulk type II superconductor in a magnetic field remains in a flux-free state which survives to a lower critical field, H_{c1}. Above this field superconductivity is partially destroyed by the nucleation of flux quantised vortices at surfaces and their subsequent penetration into the body of the sample. An important consequence of the distortion of the edge (surface) currents during the vortex nucleation stage is the appearance of an attraction between the vortex and the surface. This attraction can be viewed as arising from an external image antivortex, whose presence ensures that there is no net current perpendicular to the surface. Image antivortices effectively delay the transition to the vortex state until the applied field reaches a penetration field, $H_p > H_{c1}$, and the potential "hill" which must be surmounted to enter the sample is called the Bean-Livingston barrier (BLB).[1]

This scenario is slightly complicated by the fact that vortices can be thermally

[1] C.f. Chapter (3.1)

excited over the BLB at finite temperatures, when the transition to the vortex state is not fundamentally blocked. Hence, provided sufficient time elapses after application of the field, the transition will occur close to H_{c1}, as for a "bulk" sample (see, for example, ref. [30].) For finite measurement times, however, the magnitude and temperature dependence of the penetration field differs dramatically from H_{c1}, and several studies have attempted to determine the form of $H_p(T)$, most recently in the layered cuprate superconductor $Bi_2Sr_2CaCu_2O_8$ (BSCCO). The highly anisotropic electronic structure of BSCCO is reflected in the vortices formed in the mixed state; with the applied field along the high symmetry c-axis flux lines are composed of stacks of weakly-coupled pancake vortices (PVs) whose currents are confined to the CuO_2 planes.[2] Since the PVs are only weakly coupled to one another, an individual PV can surmount the BLB independently of the rest of the stack, which is then subsequently dragged after it. This is however partially balanced by the large Ginsburg Landau parameter ($\kappa \approx 100$) of BSCCO, which increases the height of the BLB,[3] but it is now well established that the thermal excitation of individual PVs over the BLB is the rate-limiting step for flux penetration. For a layered sample with a pristine surface, it can be shown that $H_p(T)$ is described by [38]

$$H_p(T) = RH_c e^{-\frac{T}{T_0}}, \tag{5.1}$$

where R is the scaling factor between the applied field and the local field at the edge of the sample, T_0 is a characteristic temperature, and H_c is the thermodynamic critical field. While R corresponds to the demagnetisation factor in a sample with ellipsoidal cross section, it is not straightforward to specify its value in a sample with arbitrary cross section.[4] Indeed, experimental validation of Eq. (5.1) in real type II samples is made complicated by this as well as the effects of bulk pinning and edge shape or geometrical surface barriers (GB) [2], which together mask the true influence of the BLB on penetration. A common method for partially eliminating these other barriers is to modify the sample cross section [10, 5, 65], and there is good evidence to suggest that the BLB dominates the transition to the vortex state in BSCCO platelets at intermediate temperatures (15 K $< T <$ 70 K) [10, 39, 9], and the GB above ($T >$70 K). Due to the much larger energies required to surmount the GB the probability of thermal excitation is also vanishingly small [2]. Thus a measurement of the temperature dependence

[2]C.f. Chapter (2)
[3]C.f. Eq. (3.2) and Ref. [37]
[4]C.f. Chapter (3.2)

of the applied field at penetration is a conclusive way of distinguishing between the GB and the BLB [10].

BSCCO micro-disks fabricated from single crystals were recently suggested [9] as promising systems for investigating the effect of surface barriers in BSCCO due to the low bulk pinning barrier. However, a feature of BSCCO single crystals, and indeed most other superconductors that are used to fabricate such disks, is the presence of quenched microscopic disorder which inevitably locally perturbs the BLB. In BSCCO, for instance, disorder commonly takes the form of linear defects (LDs) aligned close to the a-axis growth direction. While the origin and composition of these defects is currently unclear, evidence for their oxygen deficient stoichiometry, obtained by high resolution STEM-EDS [66], is consistent with the enhanced pinning and preferential penetration of flux along the defects [67], a behaviour caused by the suppression of superconductivity and similar to that along weak intergranular links such as twin boundaries. Magneto-optical images of single crystals grown using the travelling solvent floating zone technique reveal that the LDs extend along the entire length of the crystal with a non-uniform spacing [68], suggesting that they could be small angle grain boundaries between individual crystallites [69, 70]. However, recent observations of a second drop in the in-plane resistivity at T $\approx$ 106 K supports the idea that they are needle-like intergrowths of the higher T_c Bi-2223 phase [71].

In order to observe the interplay between a controlled sample geometry, quenched disorder and the BLB, arrays of micro-disks have been fabricated on the surface of a BSCCO single crystal. By systematically observing the flux distribution as a function of sample history using differential magneto-optical imaging (MOI), we observe an exponential decay of $H_p(T)$ for penetration into the disks that is in good agreement with the behaviour predicted by Eq. (5.1). Additionally, the penetration field is suppressed for disks which lie on the linear defects, confirming that quenched disorder has a strong influence on the BLB.

In the series of samples investigated in this work, two flakes were cleaved from the same optimally doped BSCCO single crystal (2 mm $\times$ 2 mm $\times$ 100 μm) and arrays of disks were patterned to a depth of $\approx$ 300 nm in each using the fabrication method described in Appendix A. A typical region of the array, shown in Fig. 5.1, consisted of 5 μm, 10 μm, 15 μm and 20 μm diameter disks sited on the corners of a square with a lattice constant of 20 μm, and lattice vectors inclined at 45° to

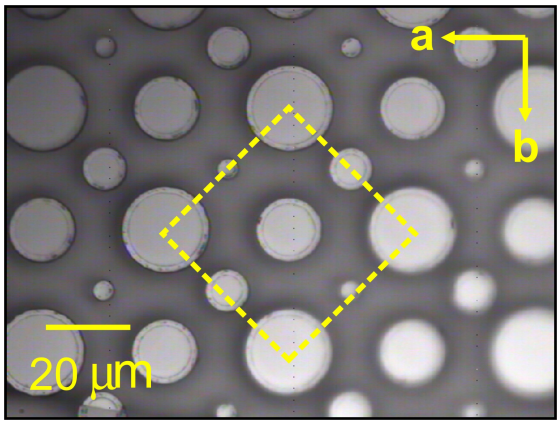

Figure 5.1: Optical micrograph of the disk array showing the square unit cell (40μm $\times$ 40 μm) orientation with respect to the crystallographic axes.

the crystallographic a-axis of the crystal. The patterned area was typically 1-2 mm^2 and was attached to a Silicon substrate for mechanical stability.

Although the disks are actually sitting on top of a BSCCO platelet, this plays no role for the penetration of flux into the disks themselves since bulk vortex pinning will be negligibly small at our measurement temperatures. Hence, once vortices enter into the platelet, they arrange themselves with distributions of $\mathbf{B}$ and $\mathbf{H}$ such that to good approximation $\mathbf{J} = \nabla \times \mathbf{H} = 0$, just as in free space. Prior to penetration the BLB at the sides of the disks presents a barrier to the entry of vortices into the disk. The screening currents are large on the top of the disk, pulling the tops of the vortices toward the center of the disk, but the vortex line tension balances this force. Even though there is no "surface" at the bottom of the disk, there must also be an effective sheet current similar to that on the top surface arising from $\mathbf{J} = \nabla \times \mathbf{H}$ and the discontinuity in $\mathbf{H}$ between the vortex-filled region, where $H_z > H_{c1}$, and the vortex-free region inside the disk, where $H_z = 0$ [72].

5.2 Results

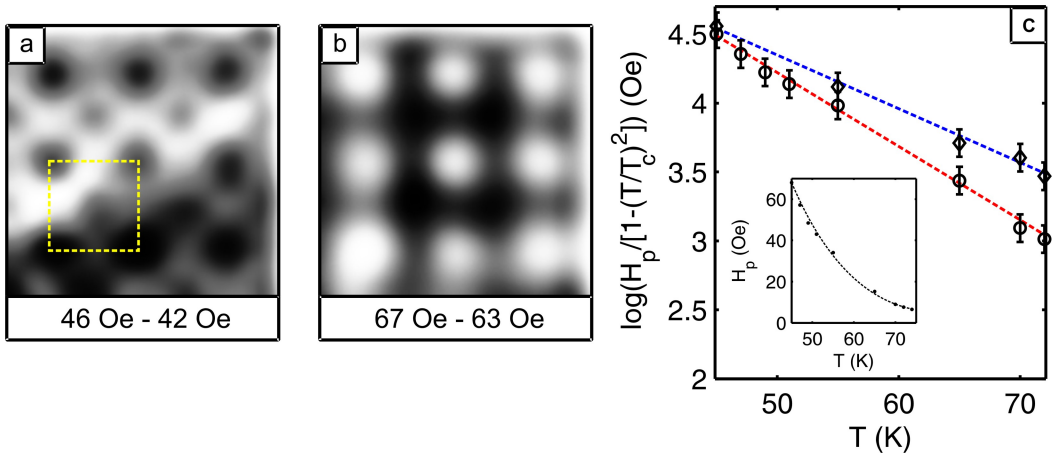

Figure 5.2: MOI difference images (100 μm $\times$ 100 μm) at $T = 45$ K: (a) below and (b) above H_p for the 20 m disks. Dashed outline indicates the unit cell [c.f., Fig. 5.1.] (c) Logarthmic plot of the experimental data for the 15 μm ($\diamond$) and 20 μm ($\circ$) for the temperature dependence of H_p together with the theoretical fits (dashed lines) using Eq. (5.1). The plot shown in the inset shows the same data on linear axes for the 20 μm disk.

The disk array was cooled below T_c and imaged using the low-temperature MOI system based on a cryocooler.[5] Figure 5.2 shows two MO difference images taken in increasing applied fields after cooling the sample to $T = 45$ K. As anticipated, the change in the distribution of flux for the low fields in Fig. 5.2(a) is strongly modulated by the disks. In particular, the intensity in the interstitial regions increases while the intensity over the unpenetrated disks remains low in comparison. Fig. 5.2(b) shows the difference between two slightly higher fields, where the opposite behaviour is observed and the disks exhibit the strongest positive change in flux. Clearly this is only happening in the 20 μm disks at this field, and it is not until a slightly higher field that the smaller disks begin to be penetrated. The smallest disks could not be analysed further in great detail due to the low spatial resolution in this experiment, but by systematically analysing difference images at various temperatures we were able to establish the temperature dependence of the penetration field of the 20 μm and 15 μm disks. (In this case, $H_p(T)$ is defined to be the field when flux first enters the disk.) the The amount of flux entering the disks at penetration was too small to be measured for $T > 80$ K, so there are no measurements close to the critical temperature T_c (≈ 91 K). (T_c itself was measured by finding the temperature at which contrast was lost at the edge of the platelet, and H_p should obviously be zero at T_c.)

[5]Details of the system can be found in chapter (4.2) and Ref. [34].

Since $H_c \approx (\sqrt{2}\kappa/\ln\kappa)H_{c1}$ [17] and

$$H_{c1}(T) = H_{c1}(0)\left[1 - \left(\frac{T}{T_c}\right)^2\right],$$

then the expression for the penetration field in Eq.(5.1) becomes

$$H_p(T) = R\frac{\sqrt{2}\kappa}{\ln\kappa}H_{c1}(0)\left[1 - \left(\frac{T}{T_c}\right)^2\right]e^{-\frac{T}{T_0}}. \tag{5.2}$$

The experimental data are plotted in Fig. 5.2(c) on axes of $\log\left(H_p/[1-(T/T_c)^2]\right)$ Vs. T in order to extract the parameters of Eq. (5.2). For clarity the raw data is plotted in the inset of Fig. 5.2, from which one can see that H_p decays rapidly with increasing temperature. Curves obeying the form of Eq. (5.2) were fitted to the data sets and the results are shown as dashed lines in Fig. 5.2(c), yielding values for T_0 of 19 K and 25 K for the 20 μm and 15 μm. The prefactor $[R(\sqrt{2}\kappa/\ln\kappa)H_{c1}(0)]$ is equal to 990 Oe and the correlation coefficient between the model with these parameters and the data is > 0.99 in both cases, suggesting that it produces a good fit. This result is consistent with previous studies, although we should emphasise that our fits are not sensitive to the behaviour of $H_p(T)$ close to T_c, where the parabolic decrease in $H_c(T)$ begins to dominate. The value for T_0 is close to those obtained previously for disks (35 K) [9], whiskers (18 K) [73], and single crystals (15 K) [39]. Using the most reliable data set for the 20 μm disks we can estimate an upper and lower bound for R from the exponential prefactor. Taking $\kappa \approx 100 \pm 10$ and $H_{c1}(0) \approx 100 \pm 20$ Oe[6], from which we obtain $0.27 < R < 0.42$. This value is closer to the expected values for a disk with rectangular cross-section, for which $R = \sqrt{(d/2W)} \approx 0.12$, than one with an ellipsoidal cross-section, for which R is an order of magnitude less $R = (d/2W) \approx 0.015$.[7]

[6] C.f. Fig. 2.8(b)

[7] C.f. Eq. (3.19), chapter (3.2)

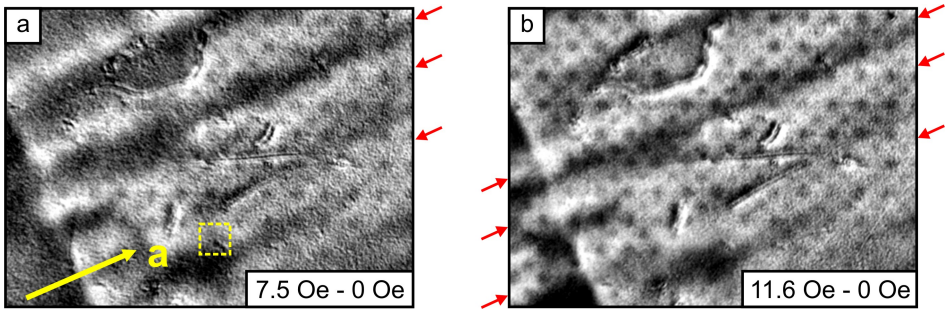

Figure 5.3: MO difference images (0.4 mm × 0.3 mm, T = 72 K) constructed by subtracting images captured at applied fields of (a) 7.5 Oe and (b) 11.6 Oe from the reference state in zero field. Red arrows indicate the location of linear flux channels and the dashed outline in (a) indicates the unit cell of the array with corners on the 20 μm disks [c.f. Fig. (5.1).]

Having established the dominance of the BLB in the disks, we now discuss our observations relating to inhomogeneous penetration into the underlying platelet. Figure 5.3 shows two 72 K MOI difference images captured at the two different indicated applied fields. Upon applying a small field of $H_z = 7.5$ Oe [Fig. 5.3(a)], well defined linear regions of high flux density, aligned close to the crystallographic a-axis, develop across the entire surface, showing that, in line with previous studies, PVs preferentially penetrate and accumulate along linear defects (LDs) which are aligned close to the a-axis growth direction [74, 75]. The disks are still resolved in these regions due to their slightly lower MO intensity. A surface step, produced when the sample was cleaved, is visible in the lower left hand corner, and the flow of the flux within the linear channels [indicated by the red arrows in Fig. (5.3)] can be seen to terminate at the surface step. It is not until a higher field, $H_z = 11.6$ Oe, is applied [Fig. 5.3(b)] that the vortices in the linear regions "spill over" into the interstital regions on the raised side of the step, where they continue to be guided by the linear channels, confirming their correlation down through the c-axis (perpendicular to the sample surface).

We observe a striking variation of the penetration field for a few disks at very specific locations in the array, as is demonstrated by the images in Fig. 5.4. In particular, a small proportion of the disks exhibit a positive change in flux at a field lower than the values of H_p plotted in Fig. 5.2(c). In Fig. 5.4(a), the change in the flux distribution at $T = 45$ K is initially strongly modulated by a linear channels due to enhanced vortex mobility and density in the brighter areas. Fig. 5.4(b) shows the same region at the slightly higher field of $H_z = 50$ Oe.

Strikingly, disks lying exactly on the border between the high and low flux den-

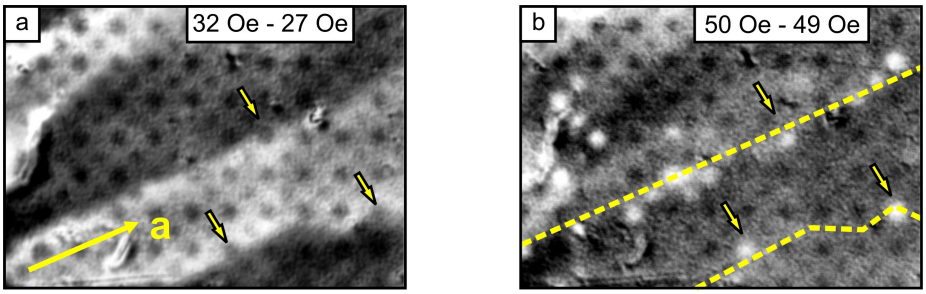

Figure 5.4: MO difference images (≈ 0.4 mm $\times$ 0.3 mm, $T = 45$ K): (a) [32 Oe - 27 Oe] and (b) [50 Oe - 49 Oe.] Arrows in both images indicate the location of disks lying on the interface between the regions of differing vortex mobility. The dashed lines in (b) trace the edge of the defect observed in (a).

sity regions are now already penetrated even though the applied field is 20 Oe below the normal penetration field (68 Oe) for this temperature. Premature penetration occurs in exactly the same disks over the whole range of temperatures investigated, although at higher temperatures the difference from the average penetration field becomes progressively smaller. It has been demonstrated that the vortex density within the linear regions is higher, making it plausible that the local field in the vicinity of the disks in these regions is slightly enhanced [76]. However, in this scenario one would expect all the disks within the defect region to be penetrated earlier, and not just those lying at the channel interface. Alternatively we speculate that early penetration is related to a local reduction of the BLB where the edge of the linear channel intersects the disk, though the exact microscopic origin of this effect remains unclear.

Chapter 6

Anisotropic Pancake Vortex Transport in BSCCO Crystals

6.1 Introduction

A novel consequence of the JV-PV interaction in the crossing lattices regime of BSCCO is that the penetration of pancake vortices under tilted magnetic fields becomes sensitive to the presence of Josephson vortices. SHPM experiments [25] have revealed that the PV mobility along JV stacks is considerably higher than in JV-free regions, and the presence of JVs reduces the interaction between PVs and quenched "bulk" disorder, effectively depinning them. In addition, at fields just above the out-of-plane penetration field, H_p, PVs preferentially enter the sample along JVs, where the superposition of Meissner and JV currents at the edges leads to a slight lowering of the Bean-Livingston barrier [38], and then enjoy a much higher mobility along the JV stacks [77, 78]. It has also been demonstrated that stacks of JVs can become indirectly pinned via their interactions with strongly pinned pancake vortices [79]. Consequently, the irreversible out-of-plane magnetisation under tilted magnetic fields is sensitive to the underlying JV structure and its relationship to the quenched disorder in the sample. This property is exploited in the work described in this chapter to explore the anisotropy of the disorder in an as-grown BSCCO single crystal.

BSCCO single crystals commonly exhibit correlated disorder which often takes

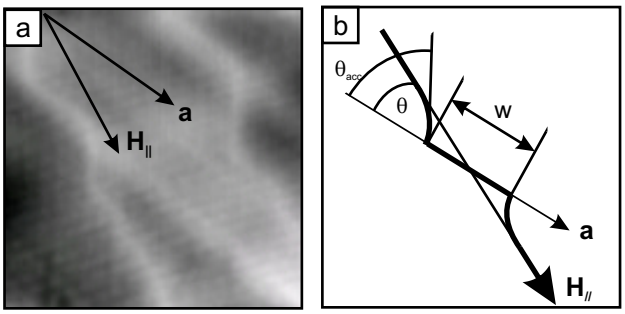

Figure 6.1: (a) SHPM image (archive data) of kinked pancake vortex chains which are decorating underlying stacks of indirectly-pinned Josephson vortices at $T = 85$ K ($H_z = 10$ Oe, $H_{||} = 34$ Oe, image size $\approx 27.5 \times 27.5$ μm^2).(b) Sketch of the model used to describe vortex trapping.

the form of linear defects (LDs) aligned close to the a-axis growth direction [74, 75] and strongly pins pancake vortices. While the origin and composition of these defects remains unclear,[1] it is generally accepted that they are able to pin high PV flux densities and have a striking indirect consequence on the local structure of the in-plane JV lattice.

Due to the mutual attraction between the crossing lattices,[2] a segment of a JV stack can be indirectly pinned along a LD by PVs directly pinned in the LD region. In addition, when the in-plane field subtends an angle θ to the LDs, partially trapped JV stacks form kinks at each defect-JV line intersection, analogous to the accommodation of tilted vortices by columnar defects [80] and twin boundaries. An SHPM image of this kinked structure is shown in Fig. 6.1(a) and may be analysed by accounting for the anisotropy in an existing theory of vortex deformation by planar defects, to relate the length of the trapped segment, w, to θ [79, 81, 82]. The geometry used to analyse vortex deformation is shown in Fig. 6.1(b). The elastic energy of the stretched JV string and the deformation of the surrounding JV "cage" is balanced against the additional crossing energy gained due to interaction with the extra pinned PV stacks on the LD. For angles smaller than a critical accommodation angle, θ_{acc}, w reduces with increasing angle according to

$$w \cos\theta = \sqrt{\frac{4\sigma}{K}} \left(\sqrt{\frac{\tan\theta_{acc} \sin\theta_{acc}}{\tan\theta \sin\theta}} - 1 \right), \tag{6.1}$$

[1] See chapter (5) for a detailed discussion.
[2] C.f. Chapter (2.6)

where $K = \Phi_0 B_{||}/4\pi\gamma^2\lambda^2$, arises from the "cage potential" interaction with neighbouring Josephson vortices, $\sigma = {\Phi_0}^2/4\pi^2\gamma\lambda^2$ is the JV line tension and θ_{acc} is defined by

$$\tan\theta_{acc}\sin\theta_{acc} = \frac{2U_p}{\sigma}, \tag{6.2}$$

where U_p is the indirect pinning potential per unit length. (Here Φ_0 is the flux quantum, $B_{||}$ is the in-plane induction, γ is the anisotropy parameter, and λ is the in-plane penetration depth.) For $\theta \geq \theta_{acc}$, $w = 0$ and the Josephson vortex is straight and parallel to the in-plane field direction. In the following we demonstrate that the out-of-plane "local" magnetisation of a BSCCO crystal in a fixed applied in-plane field reflects this angle-dependent interaction between Josephson vortices and linear defects.

6.2 Experiment

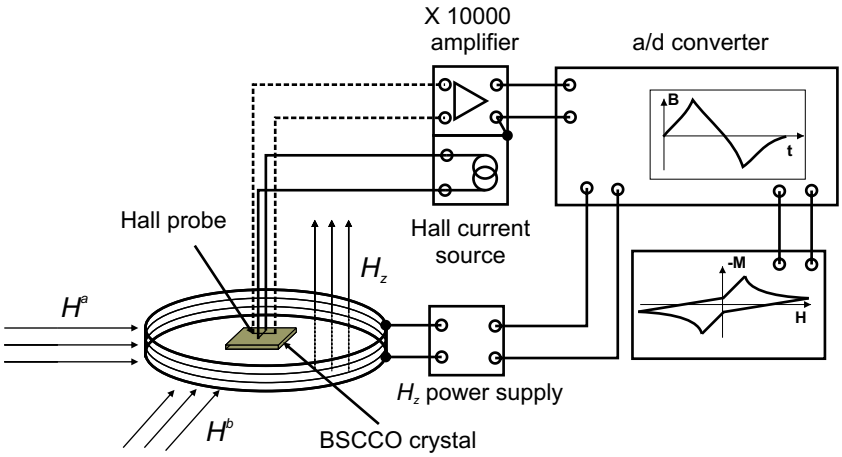

Figure 6.2: Schematic of the apparatus for measuring the irreversible magnetisation of a BSCCO single crystal. The a/d converter records the Hall voltage, which is proportional to the induction, then subtracts a previously recorded reference field to obtain the magnetisation. The in-plane fields H^a and H^b are generated by coils with orthogonal axes controlled using separate power supplies.

An as-grown BSCCO single crystal ($T_c \approx 91$ K, dimensions ≈ 2.5 mm $\times$ 2 mm $\times$ 100 μm) was fixed with low melting temperature paraffin wax to a low noise micro-Hall probe, patterned by electron beam lithography and wet etching in a GaAs/AlGaAs heterostructure two-dimensional electron gas, with an active flux sensing area of 1 μm^2 and a Hall coefficient of 0.3 Ω/G. The Hall sensor was driven with a 10 μA dc current from a precision source, and the measured Hall

voltage amplified with a 10,000 gain ultra-low noise pre-amplifier, which incorporated electronic compensation of the $H_z = 0$ sensor offset. The magnetic field resolution of the entire measurement system at 85 K is ≈ 1 mG/Hz$^{1/2}$ or about $10^{-4}\Phi_0$/Hz$^{1/2}$. The crystal was cleaved immediately prior to mounting and the sample-sensor spacing is ≈ 1 μm. The packaged sensor was mounted on the copper head of the sample insert for a temperature-controlled cryostat, and the crystallographic a- and b-axes of the crystal aligned to within $\pm 10^\circ$ of the axes of two external Helmholtz coil pairs used to produce independent in-plane fields, H^a and H^b , up to ≈ 36 Oe. An out-of-plane field, H_z, was generated by a copper coil wound directly around the cryostat at the same height as the sample (Fig. 6.2.)

At the start of each measurement the sample was cooled in the Earth's field to the desired temperature between 77 K and T_c. H^a and H^b were then applied manually to generate the required field, $H_{||}$, at an angle θ to the a-axis. Finally the out-of-plane field, H_z, was swept around a measurement cycle between $\pm$ 36 Oe using a computer-controlled power supply, and the local magnetic induction at the Hall sensor, B_z, recorded at each point via an a/d converter. The first "virgin" trace was discarded, and the subsequent 25 cycles then averaged to improve the signal:noise ratio still further. The measured "local" out-of-plane magnetisation ($\mu_0 M_z = B_z - \mu_0 H_z$) was then constructed as a function of magnitude and angle of the in-plane field.

6.3 Results

Fig. 6.3 illustrates typical out-of-plane local magnetisation data at $T = 85$ K with no in-plane field ($H_{||} = 0$) as well as $H_{||} = 16.5$ Oe applied close to the a- or b-axes (see inset). Close inspection reveals that the zero-field irreversibility, $\Delta M_z = M_z(H_z = 0, dH_z/dt > 0) - M_z(H_z = 0, dH_z/dt < 0)$, depends strongly on the magnitude and direction of the in-plane field. The data for a- and b-axis in-plane fields of varying magnitude are summarised in Fig. 6.4, where ΔM_z has been normalised with respect to $\Delta M_{z,0}$, which is the value at $H_{||} = 0$, and behaviour for the two orthogonal directions are strikingly different. For fields applied close to the a-axis the irreversibility actually increases as $H_{||}$ is increased up to ≈ 15 Oe, beyond which it starts to fall again. In contrast, a reduction of

the irreversibility is always observed as $H_{||}$ is increased parallel to the b-axis.

The two different behaviours can almost certainly be related to the fact that the a-axis is parallel to the characteristic linear defects in these crystals, while the b-axis is perpendicular to them. The observation that the irreversibility falls monotonically for increasing in-plane fields directed along the b-axis is in line with previous reports [71]. It is consistent with the "channelling" of penetrating PVs along underlying JV stacks, which is known to suppress their interaction with quenched disorder and hence reduce the measured irreversibility [25, 83]. The inset of Fig. 6.4 illustrates that, for $H_{||} > 5$ Oe, the decrease in the irreversibility in this geometry depends linearly on $\sqrt{H_{||}}$.

Since the lateral density of JV stacks, $1/a_y = \sqrt{2B_{||}\sqrt{3}\gamma\Phi_0}$, also depends on $H_{||}$ in the same way (the difference between $H_{||}$ and $B_{||}$ becomes small at fields above 5 Oe for our sample,) this suggests that the reduction of irreversibility is simply proportional to the total number of JV stacks present in the sample in this regime. The fact that the fit line in the inset of Fig. 6.4 extrapolates to ≈ 1.4 at $H_{||} = 0$, instead of the expected value of 1, is not surprising. The effectively 1D process of PV motion along JVs will only suppress the irreversibility due to interactions with random and linear disorder when the JV stacks are sufficiently dense. At low

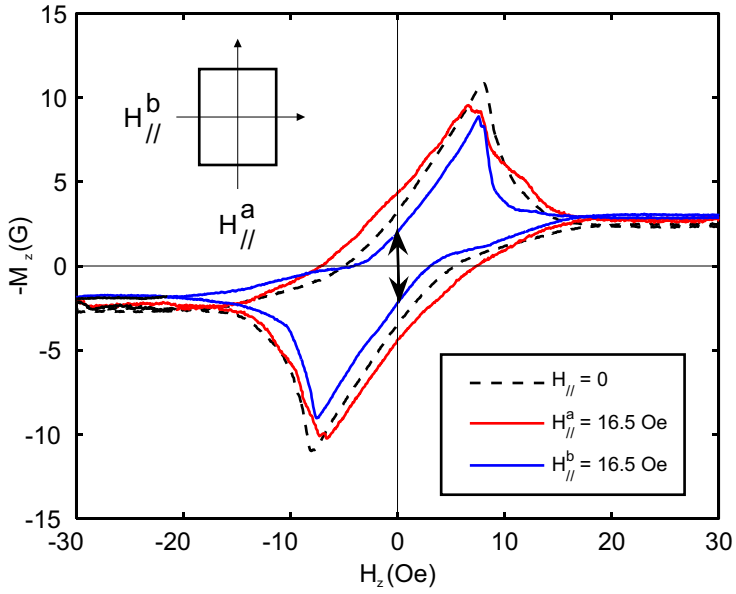

Figure 6.3: Plots of the "local" magnetisation versus out-of-plane magnetic field at $T = 85$ K for $H_{||} = 0$ (dashed line) and in-plane fields, $H^a_{||} = 16.5$ Oe ($H^b_{||} = 0$) and $H^b_{||} = 16.5$ Oe ($H^a_{||} = 0$) (solid lines - see inset). Vertical arrow indicates the zero-field remanence.

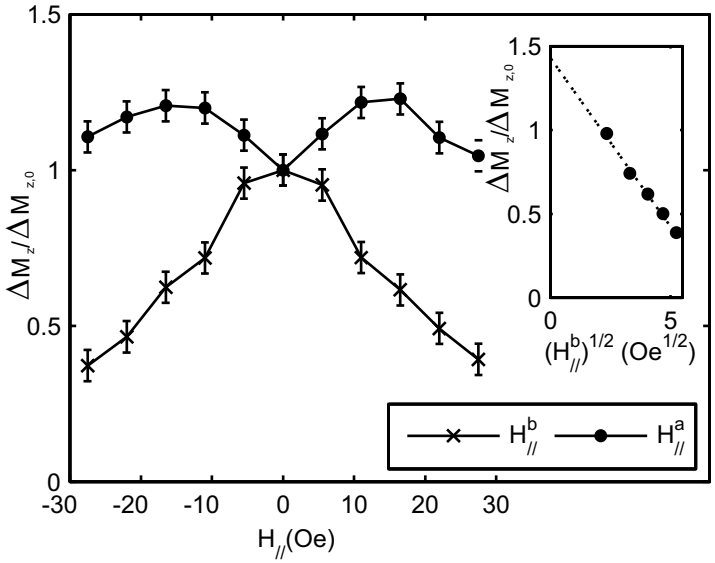

Figure 6.4: Normalised remanence, $\Delta M_z/\Delta M_{z,0}$, plotted against $H_{||}$ for the two in-plane field orientations, and (inset) against $(H^b_{||})^{1/2}$ to illustrate the linear dependence of the JV channelling efficiency (dashed line is extrapolated from the linear fit to the high field data).

fields, when the stack spacing is large, the measured changes in the irreversibility will be smaller than an estimate based on 1D effects alone. Another factor that contributes to this deviation is the difference between the applied field, $H_{||}$, and the actual induction, $B_{||}$, which yields the negative in-plane magnetisation [35] due to JV screening currents, and is important at low fields.

The increase in the irreversibility when the in-plane field is parallel to the a-axis ($H_{||} < 15$ Oe) is a surprising result which has not been reported before. It does, however, have a natural explanation in terms of the indirect pinning of JV stacks interacting with strongly pinned PVs. For $H_{||}$ parallel to the a-axis, and hence the LDs, this would tend to trap JV stacks along linear defects. Therefore, at low in-plane fields the penetrating PVs are channelled into the regions of highest disorder, they become strongly pinned, and the irreversible magnetisation increases. Within this scenario the maximum pinning occurs when there is quasi-commensurability between the JV stacks and the disordered distribution of linear defects. At the peak field of $H_{||} \approx 15$ Oe the JV stack spacing in as-grown BSCCO ($\gamma = 600$) is $c_y \approx 20$ μm, implying a similar mean lateral spacing between linear defects, in good agreement with estimates from both angular x-ray measurements [75] as well as the SHPM and MO images presented in references [79] and [70] for crystals from the same source. As the in-plane field is increased above ≈ 15 Oe JV stacks increasingly start to fall between defect regions, which

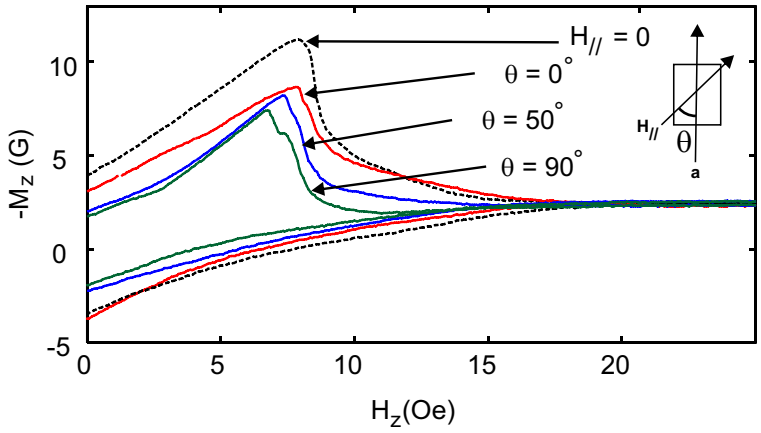

Figure 6.5: $T = 85$ K "local" magnetisation loops for $H_{||} = 0$ and $H_{||} = 36$ Oe at different in-plane angles (see inset for definition of θ).

begin to channel penetrating PV stacks in the usual way, leading to a reduction in the irreversibility. The defect separations will be quite disordered in practice, but the JV lattice will be able to deform to accommodate to this provided approximate commensurability is achieved. The relatively broad "matching peak" in Fig. 6.4 is consistent with this picture. Anisotropic pinning due to LDs was also observed in a.c. permeability measurements on BSCCO crystals with the a.c. excitation field parallel to the CuO_2 planes. However, this work, presented in Ref. [75], focuses on the first order vortex melting transition, and was not interpreted in terms of crossing lattices.

Fig. 6.5 shows a series of magnetisation curves illustrating how the irreversibility, ΔM_z, varies as a function of in-plane field angle, θ, for a fixed in plane field strength, $H_{||} = 36$ Oe. In this experiment, the two pairs of Helmholtz coils were driven by two separate power supplies to give the required in-plane field vector. The in-plane field angle was rotated through 360° and Fig. 6.6 shows the plot of the normalised irreversibility $\Delta M_z/\Delta M_{z,0}$ as a function of angle. $\Delta M_z(\theta)$ is found to display a 180° rotation symmetry as expected from the rectangular symmetry of the BSCCO crystal, but pronounced shoulders around 55° and 235° break the expected $\Delta M_z(\theta) = \Delta M_z(-\theta)$ symmetry. These angles are close to the accommodation angle beyond which a JV is unable to become even partially indirectly pinned along a linear defect [c.f. Fig. 6.1(b) for definition of θ_{acc}.] JV trapping has been clearly observed in earlier SHPM measurements [79] in very similar crystals to the one studied here. Fig. 6.1(a) shows a typical image which contains two partially pinned JV stacks in a sample at $T = 85$ K where an in-plane field of 34 Oe has been applied at an angle of about 30° to the a-axis. It can

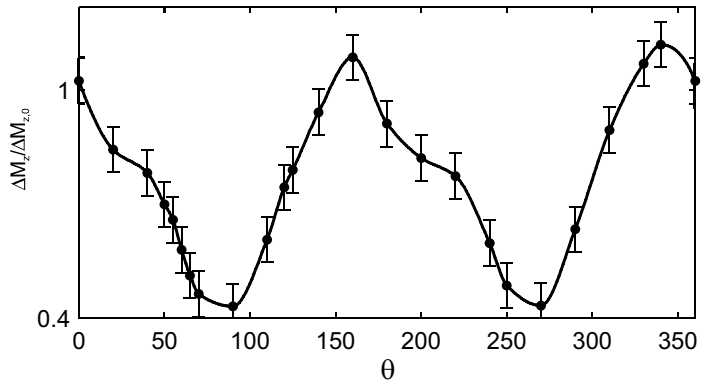

Figure 6.6: Normalised remanence, $\Delta M_z/\Delta M_{z,0}$, as a function of in-plane field angle (solid line is a guide to the eye).

be shown that the accommodation angle defined in Eq. (6.1) can be identified with the angle at which elastic JV strings approach the linear defect parallel to the a-axis [c.f. sketch in Fig. 6.1(b).] Hence we can estimate that $\theta_{acc} \approx 65^\circ$ for this image. Beyond the accommodation angle the length of the trapped JV segment drops to zero and the channelling of penetrating PVs should be greatly enhanced, since they are no longer being forced to travel along the linear defects in the indirectly pinned regions. The angular shift of $\approx$ -10° of the shoulder positions from the expected accommodation angles must be partly due to a slight misalignment of the BSCCO crystal relative to the Helmholtz coils. However, within vortex trapping theory it is the LD direction which defines the angular origin, and MO images [70] suggest that it can deviate by up to $\approx 10^\circ$ from the a-axis.

The broken $\Delta M_z(\theta) = \Delta M_z(-\theta)$ symmetry must arise from some irreversibility associated with the vortex trapping that depends on the measurement history. The in-plane fields in Fig. 6.6 were rotated monotonically in a positive sense from $\theta = 0$, and the broken symmetry must arise from the details of the trapping of elastic Josephson vortex strings under these conditions. For example, at small angles ($\theta \approx 0$) the JVs will be readily trapped on linear defects since they run almost parallel to them. Furthermore, even when the out-of-plane field is reduced to zero, enough strongly pinned PVs remain in the sample to ensure the indirect pinning of JVs. Hence, when the in-plane field is rotated to a new angle the JV system retains a memory of its history.

Once the angle exceeds the accommodation angle the JVs snap away from the

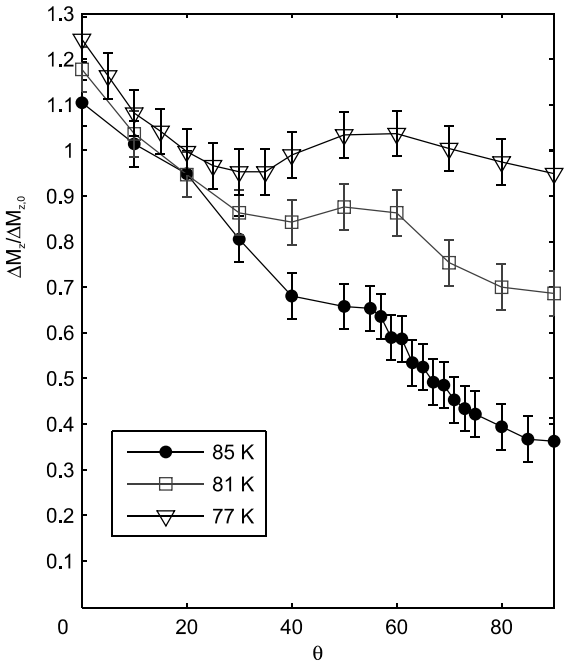

Figure 6.7: Angular dependence of the normalised remanence, $\Delta M_z/\Delta M_{z,0}$, in the vicinity of the trapping shoulder around the accommodation angle for three different temperatures. The in-plane field strength is 36 Oe.

linear defects and become straight. If one continues rotating the JV system beyond the second accommodation angle [$\theta > (180 - \theta_{acc})$] there will be a large barrier for the straight JV strings to deform and find their equilibrium trapping state. Hence it is likely that metastable straight JVs are found even well within the accommodation angle (and also metastable trapped JVs outside the accommodation angle) giving rise to the observed asymmetry as θ_{acc} is approached from above or below. This picture has been confirmed by varying the in-plane field angle in both a positive and negative sense at $T = 77$ K. For the former situation a shoulder was observed at $\theta \approx 55°$ in agreement with Fig. 6.6, while for the latter it only formed at the second accommodation angle $\theta \approx 55°(\equiv +285°)$.

Fig. 6.7 illustrates how the normalised irreversibility in the range $0° < \theta < 90°$ changes with temperature. At lower temperatures, due to a reduction in PV thermal energy, bulk pinning of PVs dominates over PV trapping and channelling along JVs, and we observe an overall increase in number of PV stacks pinned at H_z =0. (The ratio of PV bulk pinning energy to crossing energy of PV-JV interaction is proportional to $1/\lambda(T)^2$ [32] and hence is higher at low temperatures.) In this regime the influence of channelling is therefore reduced, and the irreversibility is a relatively weak function of angle. It is interesting to

note that even in the absence of efficient channelling, the JV-PV interaction with LDs still produces a weak peak around the accommodation angle. We speculate that this is due to increased meandering of JV stacks in this angular range arising from indirect pinning on strong point-like pinning sites in addition to linear defects. In contrast, at high temperatures ($T = 85$ K) the system appears to be dominated by channelling on JVs, the shoulder near 55° is very pronounced, and the irreversibility drops by almost a factor of four on rotating the in-plane field from the a- to b-axis.

Chapter 7

Continuum Versus Discrete Flux Behaviour in BSCCO Micro-disks

7.1 Introduction

Developing computational techniques that can span multiple length-scales is a major focus of research in modern day nanotechnology. Models of nanoscale transistors must, for example, be able to describe them from the microscopic level of discrete electron dynamics all the way up to the macroscopic scale of contact pads, bond wires and packaging. An attractive feature of using so-called multiscale methods is that the physics of the discrete components is embedded in parameters used at the coarse scale without dramatically increasing the analytical and computational overhead. A certain degree of added complexity is often unavoidable when using such methods, however, especially when the fine scale properties are included without using approximations, and as a result most physical problems are in reality still described at either the discrete or continuum level.

The application of continuum models to systems composed of discrete components is a core concept common to all of the natural sciences. In physics, for example, the semi-classical conductivity tensor is a continuum approximation of the discrete quantum-mechanical Landauer-Buttiker formalism, which views conductance as the transmission of individual electrons. Continuum elasticity has

been hugely successful in describing many of the properties of structural materials, yet plastic deformation can only be understood by considering the discrete composition of solids and the atomic-scale dislocation dynamics. Since the two approaches are nearly always exclusive the key to successful multiscale modelling is establishing where the crossover lengthscale between discrete and continuum behaviours actually lies, and finding theoretical descriptions capable of bridging it.

One of the key topological properties of a type II superconductor in an applied magnetic field is the penetration and collective triangular ordering of mutually repelling lines of magnetic flux (i.e. vortices), into the so-called Abrikosov lattice. If, however, the size of a superconducting sample is reduced to mesoscopic dimensions, it is well known that the interaction between the penetrating vortices and the circulating edge currents can become comparable to the intervortex repulsion, leading to the destruction of the ordered triangular lattice. Deep in the mesoscopic regime, where the sample size is comparable to the penetration depth and/or the coherence length, this "topological confinement" is so strong that the sample geometry imposes its symmetry on multi-vortex states [51]. In superconducting disks this results in the arrangement of vortices in concentric shells [see Ref. [11] and Fig. 3.9(a)] or their collapse into a single multiquanta vortex [84]. The behaviour of vortex matter when the size of a sample is between the mesoscopic, where the position of each vortex has a direct influence on its superconducting state, and the macroscopic, where the only relevant parameter is the "local" vortex density, remains an open question. In this "large mesoscopic" regime, superconductivity coexists with a large numbers of vortices, which may or may not be organized in an Abrikosov lattice (see Ref. [6] or [85] for the analogy with confined classical clusters.) To date only a few studies have been able to access this regime experimentally [12, 86]. Available imaging techniques have proved unable to resolve individual vortices at large applied fields, while "local" magnetisation curves do not generally exhibit discontinuities that can be directly associated with transitions between the different fluxoid states seen in smaller mesoscopic disks [49]. In the absence of strong features related to individual vortices, the continuous magnetisation curves and flux profiles of large superconducting disks can be rather well described by classical continuum electromagnetism [47, 2].

Vortex matter in mesoscopic superconducting disks therefore represents an ideal

model system for studying the continuum/discrete crossover, since the vortex density and interaction strengths can be continuously tuned by varying the magnetic field and the size of the disk. The primary objective of this chapter is to address how the discrete and continuum descriptions discussed in chapters (3.4) and (3.3) can be used almost interchangeably to describe the superconducting state of disks with dimensions near this meso-to-macro crossover point. This regime is explored both experimentally, using scanning Hall probe microscopy (SHPM) and "local" magnetometry of BSCCO micro-disks, and theoretically using analytic models and modified molecular dynamics numerical simulations. Single crystal high-T_c materials are excellent candidates for studies in the large mesoscopic regime due to their low pinning, readily accessible temperatures of interest, and large κ, all of which combine to ensure that vortices are able to attain the highly ordered ground state shell structures. The disks[1] are fabricated in a periodic array on the surface of an optimally doped BSCCO single crystal in the manner described in Appendix (A). The sample was coated with Ti(5 nm)/Au(20 nm) films to enhance the stability of the SHPM when in tunnelling contact.

7.2 Results

In our first experiments the array was cooled to $T = 77$ K and SHPM images were captured at regular (increasing) field intervals. Fig. 7.1(a) illustrates how we subtract the pixels ($B^d_{i,j} = B^2_{i,j} - B^1_{i,j}$) of two SHPM scans captured in different magnetic fields to construct "difference" images. These are used in this study to enhance the contrast due small numbers of penetrating vortices which cannot be resolved in raw SHPM images. As expected [47, 2], for fields just above the penetration field H_p, a central vortex "dome" is formed which expands with increasing applied field in both the 20 μm and 10 μm diameter disks [see insets in Fig. 7.1(b).] While the "local" field[2] at which the dome forms must be almost the same in both disks, the greater enhancement of the applied field around the 20 μm disks (i.e. the larger demagnetisation factor) leads to a reduction of the measured penetration field. Figure 7.1(b) shows plots of the radius, b, of the dome of penetrated flux as a function of the applied field, H_z, for the two disk sizes. (Here we define b to be the radius at which the field reaches its minimum

[1] C.f. Fig. 5.1

[2] H_{Lp} in the notation of Eq. (3.19), chapter (3.2)

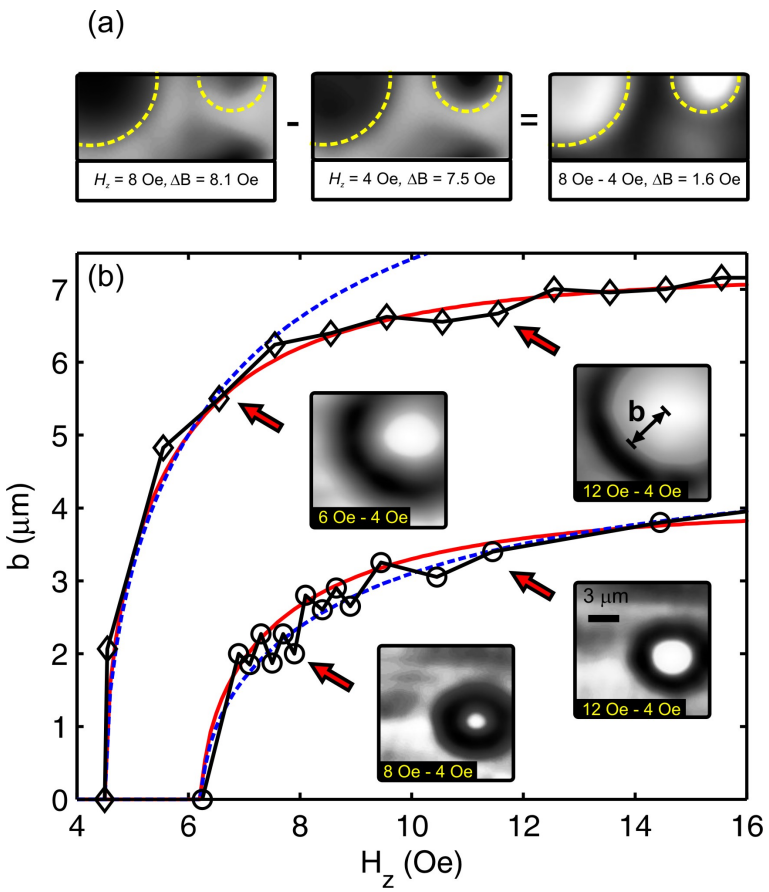

Figure 7.1: (a) 10 μm $\times$ 26 μm SHPM images captured in two applied fields at $T = 77$ K and their difference image. Dashed outlines indicate the location of two of the disks in one unit cell. (b) Radius b of the vortex dome versus the applied field, H_z, for the 10 μm ($\circ$) and 20 μm ($\diamond$) diameter disks. Insets show typical difference images used to extract the experimental points. The solid lines are fits to the measured data using a continuum model [2] and the dashed lines denote the relation for the instability radius of vortex molecules from Ref. [6].

value from the centre of the dome.) To obtain $b(H_z)$ difference images at a given applied field, H_z, were constructed with respect to a vortex-free reference state just below penetration ($H_p \approx 6.25$ Oe and 4.5 Oe for the 10 μm and 20 μm disks, respectively.) Linescans from the central peak of the dome to the minimum at its perimeter were taken along different radial directions to find an average value for the dome radius. The experimental form of $b(H_z)$ illustrates how the dome expands rapidly within a few Oersteds of the penetration field and then saturates upon approaching the high density screening currents close to the disk edge.

Focussing first on the 20 μm disk, our observations find a natural explanation within continuum [47, 2] models for flux penetration in which vortices nucleate when the applied field reaches the minimum field required for thermal activation of pancake vortices over the Bean-Livingston surface barrier (BLB). Note that

in the absence of the BLB and demagnetisation effects this field would simply be H_{c1}. In terms of the radially distributed current density, $J(r)$, the entrance condition is equivalent to requiring a critical current density at the sample edge. Analytic expressions for $J(r)$ follow from the approximation that the current density is zero within the vortex dome ($r < b$) and the magnetic induction is zero in the vortex-free region ($b < r < R$) [2]. The application of the strip model to our disks is justified by a number of studies, particularly the numerical simulations conducted in Ref. [87], where the irreversible magnetisation in pin-free disks and strips shows qualitatively identical behaviour if the strip is chosen to be twice as thick as the disk. At a given value of H_z, a steady state is reached when the radius of the dome satisfies $b = W'\sqrt{1-(H_p/H_z)^2}$ and the solid lines in Fig. 7.1(b) represent fits to this expression using W' as a fitting parameter (in the case of a strip, W' is equal to the half-width.)[3] The agreement between theory and experiment is good (we find $W' = 7.16$ μm for the upper curve, and 3.5 μm for the lower curve of Fig. 7.1(b), close to the expected 2:1 ratio,) and to our knowledge this result is the first direct experimental validation of the assumptions behind continuum models for the field dependence of the vortex dome. We note that an alternative form for the critical entry condition was derived specifically for thin disks by Brojeny and Clem [46], but was found to rise more abruptly than the experimental data.

In contrast to the 20 μm disk, it is quite apparent from Fig. 7.1(b) that the continuum expression fails to describe the oscillatory behaviour of $b(H_z)$ observed at low fields in the 10 μm disk. The origin of these features can be seen in the SHPM images of vortex clusters with 2, 3, and 4 vortices shown in 7.2(a)-(c). Although the shape of the cluster in each case allows us to determine the number of vortices without ambiguity, the strong overlap of the vortex fields hampers the resolution of their exact core positions. The field increment was reduced to just below the field step, ΔH_1, required to nucleate an additional vortex in a 10 μm disk ($\Phi_0/\pi W^2 \approx 0.263$ Oe) and the images in Fig. 7.2(d)-(f) show "difference" images between states with the same vorticity in two different applied fields. The dark regions correspond to a reduction in the local flux density where the vortices have moved closer to the centre and represent the first direct evidence for the compression of vortex clusters in increasing applied fields. This is a distinctive mesoscopic effect, caused by the interaction between vortices and the

[3]This fit corresponds closely to the model of Benkraouda and Clem [Eq. (3.25), chapter (3.3)] in the limit $R \to 1$.

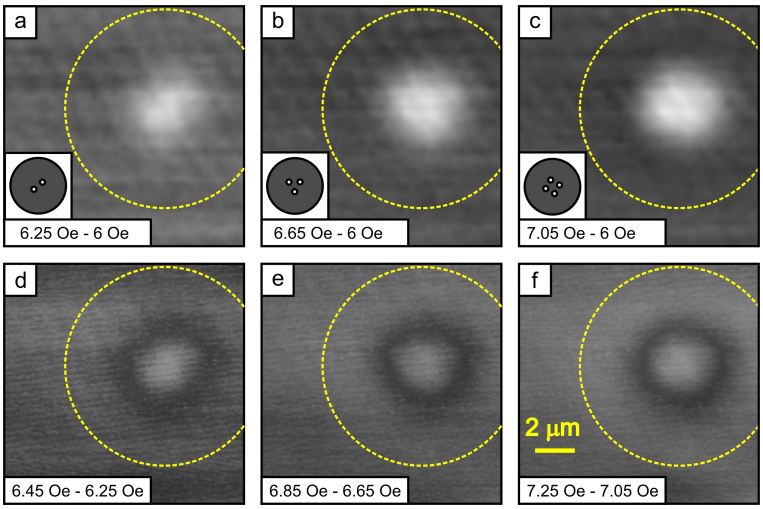

Figure 7.2: (a)-(c) Sequence of SHPM difference images showing the evolution of vortex clusters (white) with 2, 3, and 4 vortices in a 10 μm disk. Insets show sketches of the proposed vortex configurations. (d)-(f) "Difference" images between states with the same vorticity in different applied fields, corresponding to the vorticity for (a)-(c) respectively.

increasing Meissner currents at the disk edge. Considering that the edge currents decay away from the boundary on the scale of the penetration depth ($\lambda \approx 400$ nm in our sample), this striking observation of the "breathing" mode of vortex configurations is surprising given the large size of the disk ($R > 12\lambda$) and clearly supports the classification for this disk as "large mesoscopic". Returning now to the discussion of Fig. 7.1, a suitable expression for $b(H_z)$ accounting for the discrete composition of the dome has been derived in the limit of large κ [6]. By considering the forces on vortices arranged in a regular polygon encircled by a ring of radius, b, Cabral *et al.* derived $b(H_z)$ at which each vortex cluster becomes unstable with respect to the entrance of the next vortex. It is obtained by balancing the total force given by Eqs. (3.27-3.29), a procedure which amounts to finding the radius beyond which the repulsion from the edge currents overcomes the attraction from the image antivortex. For the trivial case of one vortex, the force $\mathbf{F}_i$ is balanced when

$$\left(\frac{2}{W'}\right)^3 \left(\frac{1}{1-b^2}\right) = \frac{H_0 W'^2}{2}$$

Hence the expression for the radius (in units of length) is given by

$$b = W' \sqrt{1 - \frac{\Delta H_1}{H_z}}.$$

As it stands, however, this expression cannot be compared to the measured data

because it states, unrealistically, that penetration initiates simply when the flux over the area of the disk is a single flux quantum, thus ignoring the effects of screening and surface barriers. Since the magnitude of the magnetic screening cannot be estimated with great precision, it is assumed instead that the qualitative form is correct and simply set the offset field equal to the BLB dominated penetration field H_p, and fit the above expression to the data for both disks, again using W' as a free parameter. The best fits are shown as dashed curves in Fig. 7.1(b), and were obtained for W' equal to 5.1 μm and 8.9 μm for the 10 μm and 20 μm diameter disks, respectively. The qualitative fit to the data is good for the 10 μm disk (since W' is close to the actual radius) but evidently fails for the 20 μm disk, suggesting that the crossover from discrete to continuum behaviour occurs between these two disk sizes.

In the light of the foregoing observations we see that the discrete composition of the flux must be considered in order to describe the magnetic properties of the system theoretically. A modified molecular dynamics (MD) approach based on London theory has been employed to simulate the behaviour of vortices.[4] The MD approach shows excellent correspondence to the more complex Ginzburg-Landau formalism in the extreme type-II limit. References [52] and [6] outline the derivation of the vortex-vortex and vortex-boundary interaction potentials from the expression for the free energy of small superconducting disks. Although our samples are significantly larger than λ, the results shown in Fig. 7.2 suggest a very strong influence of the boundary on the vortex configurations. On the basis of this empirical evidence we use the mesoscopic approximation for 10 μm diameter disks, and exploit Eqs. (3.27-3.29) to perform the presented simulations. A key feature of this model is the investigation of configurational changes in the vortex states in decreasing field. Starting from high applied field and a large number (≈ 100) of vortices, we track states with same vorticity as long as they are stable. In decreasing field, the previously found state is used as an initial configuration for the next, and we allow vortices at the boundary to leave the sample as the Bean-Livingston barrier decreases. This model closely corresponds to the experimental situation in which an applied magnetic field is swept down, since the weakening of the screening currents close to the vortex expulsion field favours the applicability of the London approximation (in general, London theory neglects the suppression of superconductivity on the disk edges

[4]The results which follow were performed in close collaboration with Milorad Milosevic (University of Bath.)

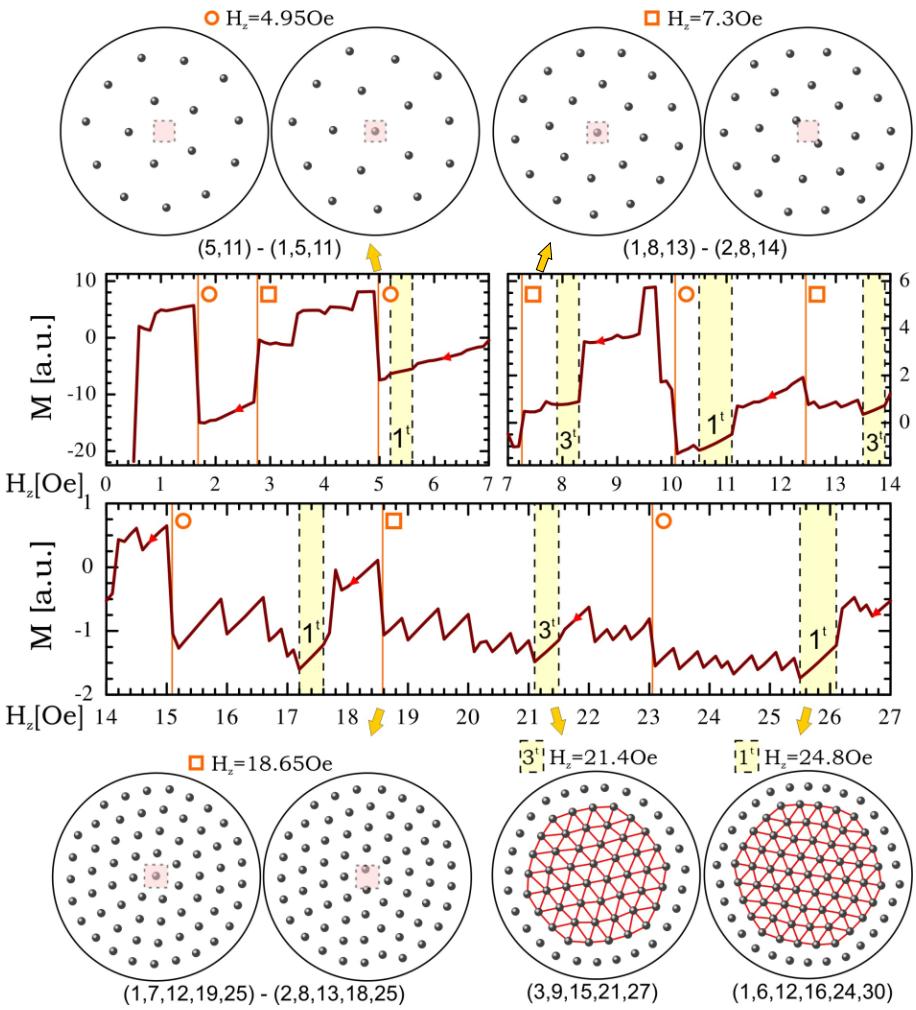

Figure 7.3: The calculated magnetisation in decreasing applied magnetic field. Top and bottom cartoons show characteristic vortex configurations to illustrate the origin of the features in the $M(H)$ curve measured across the depicted Hall probe (shaded square). In the main panel, open circles indicate formation of a new shell, while open squares denote the formation of a multivortex state in the innermost shell.

due to circulating Meissner currents.) For sequential vortex states in decreasing field, the magnetisation of the sample was calculated by integrating all vortex fields [88] [as described in Chapter (3.4).] To link the approach to the current experiments even more closely, the integration is performed at a scanning height of $z = 300$ nm through a $1{\times}1$ μm^2 square area above the centre of the disk (a situation which corresponds to a realistic Hall probe.)

The magnetic response, starting from a maximum vorticity of 100, is shown as a function of applied field in Fig. 7.3. As anticipated, each change in vorticity is accompanied by a jump in the magnetisation curve. However, in addition to these

features we also observe a series of significantly larger jumps, which stem directly from the reconfiguration of vortices in the sample. It is known that vortices in mesoscopic disks tend to form shell structures [51]. Although the evolution of the number of vortices occupying each shell strongly depends on the size of the disk and the applied field, in decreasing fields it is always the case that the innermost shell collapses first. Prior to this the number of vortices in the centre of the disk gradually decreases, and the final collapse of the shell is marked by the integration of the last central vortex into the other shells (for illustration, see configurations (1, 5, 11) $\rightarrow$ (5, 11) in Fig. 7.3.) For a Hall probe placed above the centre of the disk, there is consequently always a sharp increase in the measured magnetisation when a shell collapses, as is indicated by open circles in Fig. 7.3 (the first such transition is at 23.1 Oe.) In agreement with studies of colloidal systems, we never observe more than 5 vortices in the new innermost shell.

Further decrease of the applied field relieves the magnetic pressure at the centre, and the number of vortices in the central cluster decreases. The effect of the resulting transitions between multi-vortex structures is subtle because it depends on the size of the cluster compared to the size of the Hall probe. In principle, the reduction of the vorticity under the probe increases the measured magnetisation (see for instance the transition at 18.65 Oe and the corresponding configurations in Fig. 7.3.) However, for low vortex densities the cluster size may exceed the size of the probe. With all vortices in a cluster being effectively around the probe, the measured magnetisation now decreases when the vorticity is lowered (see transitions marked by an open square for fields below 10 Oe, and inset configurations for $H_z = 7.3$ Oe in Fig. 7.3.) In addition to the discontinuities in the magnetisation that are due to reconfigurations, we have also identified several vortex states of pronounced stability, shown by dashed lines in Fig. 7.3. All of these states show a triangular arrangement of vortices (with either one (1^t) or three (3^t) vortices in the disk centre) which gradually deforms to a shell structure near the disk boundary. In actual fact, the latter structures are simultaneously triangular and ringlike, and therefore clearly minimise the energy of a large mesoscopic disk by combining the energetically favourable vortex arrangements seen in the bulk and mesoscopic limits. This absolute minimisation of intervortex interactions results in a stable locking of the vorticity over a finite range of applied fields, as observed in Fig. 7.3.

In Fig. 7.4 we present the experimentally measured "local" magnetisation (M

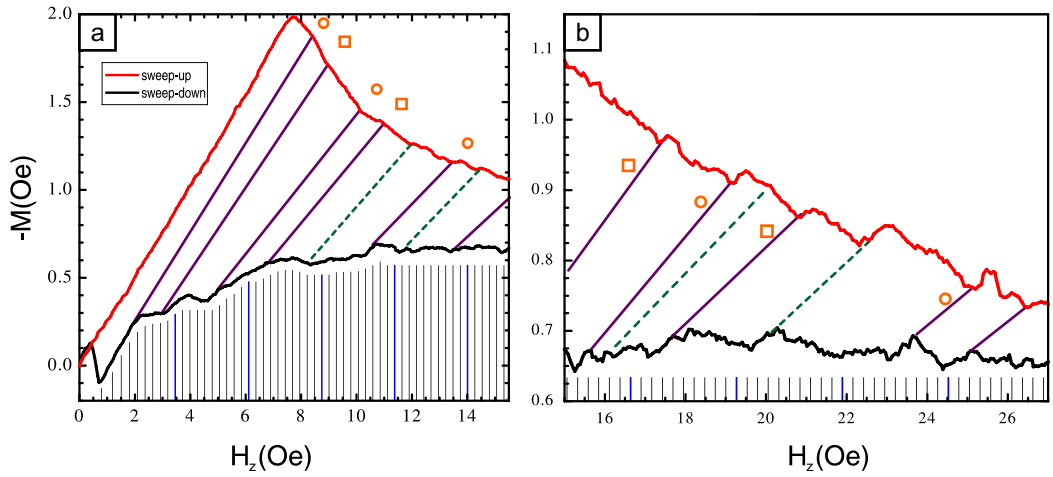

Figure 7.4: Experimentally obtained "local" $M(H_z)$ curves, for increasing (red) and decreasing (black) fields. Solid slanted lines indicate vortex transitions of the same kind (shell collapse or multvortex transition) in sweep-up and sweep-down traces, and dashed lines indicate the stable shell-triangular states. Vertical lines show the expected ground state transition fields between states with sequential vorticities [51], and blue lines have been used to indicate the fields at which the vorticity is a multiple of ten in order to facilitate the counting.

$= B_z$- $\mu_0 H_z$) captured with the SHPM Hall sensor parked at the centre of a 10 μm disk. The applied field, H_z, was swept around a measurement cycle between 36 Oe and the local magnetic induction at the Hall sensor, B_z, was recorded at each point. The first "virgin" trace was discarded, and the subsequent 50 cycles then averaged to improve the signal-to-noise ratio still further. The top curve in Fig. 7.4 was obtained in increasing field, and is different to the curve measured in decreasing field due to different conditions for flux entry/exit [c.f. Fig. 3.8(b).] Nevertheless, by following the pattern of magnetic signatures shown in Fig. 7.3, we were able to identify and link pronounced features in both sweep-up/down curves, as marked by the slanted lines in Fig. 7.4. Remarkably, almost all of the magnetisation jumps predicted by the numerical simulation were indeed found in the experimental data, for virtually the same values of the applied field on the sweep-down leg of the curve. The solid slanted lines in Fig. 7.4 represent, therefore, transitions of the same type: either a new shell formation or multivortex formation in the innermost shell. It should be emphasised that this type of transition does not necessarily occur at the same vorticity in increasing and decreasing field. The states in the combined shell-triangular structure, which are linked by the dashed lines, must appear at the same vorticity in both sweep directions due to their enhanced topological stability. It is clear that the slope of the transition lines drawn in Fig. 7.4 gradually decreases with field. At larger fields, and conse-

quently larger vorticity, the screening currents are strongly compensated by the vortex currents, and the lines gradually deviate from the Meissner slope observed prior to flux penetration. For the sake of completeness we also show the expected vorticity in the ground-state as a function of applied field in Fig. 7.4, using the expression from Ref. [51].

Finally, we use this competition between the triangular ordering of a lattice and deformation into vortex shells to define a criterion for the meso- to macroscopic crossover. For high vortex densities, a perfect triangular lattice would be ideally fitted into a superconducting disk in such a way that apices of its hexagonal footprint sit at a distance λ from the disk boundary. Vortices along the straight edges of the outer hexagon experience a net outward force which makes the formation of a shell more favourable and diminishes with increasing size of the disk. Balancing all the forces acting on the central vortex on one edge of this outer hexagon, we obtain an equality

$$\frac{1}{8\pi}\left(K_1(a\sqrt{3}) + \sqrt{3}K_1(a) + K_1((2-\sqrt{3})W + \sqrt{3})\right) = \frac{1}{a^2\sqrt{3}}e^{-((2-\sqrt{3})W+\sqrt{3})/2} \tag{7.1}$$

where a is the lattice constant of the triangular lattice (in units of λ), and K_1 is the first order Bessel function. The left side of this expression gives the sum of all inter-vortex interactions, including the image vortex, and the right side is the standard Bean-Livingston barrier decaying exponentially away from the surface, with the applied field given by a single flux quantum per unit cell of the vortex lattice. Taking $a = \lambda$ to be the limiting case for "magnetically" distinguishing between vortices in the lattice, Eq. (7.1) results in $W = 11.85\lambda$, which falls exactly within the crossover regime where our experiments are performed. However, this threshold value for a is rather conservative, and a lower estimate leads to a moderate increase of W (e.g., for $a = 0.2\lambda$, we obtain $W = 19.72\lambda$.)

Chapter 8

Thermal Fluctuations of Vortex Positions in BSCCO Crystals

8.1 Introduction

At low applied magnetic fields and temperatures, the configuration of vortices in a type II superconductor is a rigid triangular lattice with one vortex at each lattice site. It has been demonstrated by NMR [89], μSR [90], and Josephson plasma resonance [91] techniques that the field distribution around each lattice site broadens with increasing temperature, suggesting that increasing the available thermal energy allows each vortex to wander further from its equilibrium lattice position. In addition, local magnetisation [76, 92] measurements and MO images [93] have also revealed that there is an abrupt increase in the density of vortices above a characteristic field $H_m(< H_{c2})$ and temperature $T_m(< T_c)$. Taken together, these observations imply that the vortex lattice goes through a thermodynamic first order transition to a higher density liquid phase, in close analogy with the melting of an atomic lattice. H_m is found to decrease linearly with temperature near T_c, in good agreement with the thermodynamics of first order melting transitions associated with discontinuous changes in density [76, 92]. There is as yet no consensus on the precise nature of the melted vortex state, especially in the layered high temperature superconductors where PVs in separate layers are expected to decouple from one another beyond the melting field.

Since the local magnetic field at a point on the surface of a type II sample arises partly from the flux threading the cores of the vortices, the fluctuations in the positions of the vortex cores during the field broadening stage should be reflected in a time dependence of the surface field [94]. In particular, when the vortex lattice is in the crystalline phase, the spectral distibution of the surface field should replicate the spectrum of vibrations of the lattice. When vortices are in the liquid phase on the other hand, i.e., above the melting field H_m, this signature of the lattice vibrations should be replaced by the fluctuations associated with individual melted PV stacks. Hence the surface field contains valuable information about the fluctuations of the vortex state and a variety of techniques have been proposed and implemented to detect its time dependence, including cross-correlated SQUID magnetometers [95] and 2DEG Hall probes [94]. An important parameter to consider when designing experiments for detecting flux noise is the characteristic frequency ν_0 of the vortex vibration, as some techniques are more suitable over different frequency ranges than others. The value of ν_0 of vortices is unknown in detail, but is assumed to lie in the range from 10^5 to 10^{11} Hz [17]. By considering the vortex lattice as a ensemble of elastically coupled oscillators, Brandt [40], for instance, was able to derive a value for ν_0 as a function of field and temperature. For BSCCO the characteristic frequency is predicted to be $\approx$ 100 MHz and to increase linearly with the applied field. In this work, an AlGaAs/GaAs micro-Hall probe has been used to investigate how the time variation of the surface field of a BSCCO single crystal in the vortex state changes with field and temperature.

The time varying Hall voltage produced by a fluctuating magnetic field is superimposed on two random voltage sources generated inside the Hall probe. The first is 'shot' noise, which arises from the detection of individual electrons in the Hall current. This noise is especially prominent in 2DEG HPs due to the small number of electrons involved in conduction. The second voltage source is due to the thermal agitation of the electrons and is proportional to the temperature T and resistance R of the HP. This voltage V_{JN} is called Johnson noise, after Nyquist [96] and Johnson [97] who were the first to identify and explain it using the principles of statistical mechanics. Hence the Hall voltage at a given time is the sum of the shot noise, the Johnson noise and the desired "flux noise" voltage V_{FN} produced by an external magnetic field. Since time varying voltages are most naturally analysed in the frequency domain, the most appropriate way of quantifying the time variation of the Hall voltage is by measuring the noise spectral power density (NSPD), which is just the total voltage at a given frequency

measured over a square root Hertz bandwidth. The expectation is that, since V_{JN} and V_{SN} are independent of field, any field dependence of the spectral distibrution of the NSPD is related to the component V_{FN}. It is not clear whether V_{FN} will be white or manifested over a limited band of frequencies, so in this work the NSPD is investigated over the whole range of frequencies up to 300 MHz.

8.2 Experiment

An as-grown BSCCO single crystal ($T_c \approx 91$ K, dimensions ≈ 2.5 mm $\times$ 2 mm $\times$ 100 μm) was fixed with low melting temperature paraffin wax to a low noise micro-Hall probe. NSPD spectra were captured after amplification of the Hall voltage by two cascaded low noise op-amps, which provided a net gain of 10,000 on signals with frequencies up to 100 kHz. The d.c. Hall probe sensor offset was manually compensated to prevent saturation of the amplifiers and the frequency spectrum of the amplified signal was extracted using a spectrum analyser and recorded on a personal computer connected via GPIB cable. At the start of each measurement the sample was cooled in the Earth's field to the desired temperature between 77 K and T_c. The vortex lattice melting field H_m was obtained at each temperature by sweeping the out-of-plane field, H_z, around a measurement cycle between $\pm$36 Oe using a computer-controlled power supply and finding the jump in the magnetisation. Once the melting field was found at a given temperature, a static out-of-plane field was applied below the melting field and the low (1-100 Hz) and intermediate frequency (1-50 kHz) spectrum of the Hall voltage recorded using a Hewlett Packard Dynamic Signal Analyser (3561B). H_z was then raised above the melting field and spectra were recorded over the two ranges at regular field intervals.

Essentially the same procedure was followed to measure high frequency (HF) noise (1 MHz - 300 MHz). However, due to parasitic impedances of the connecting wires between the HP and the room temperature amplifiers, the expected weakness of the signal, and the presence of external interference, some modifications of the apparatus were required to enable HF signals to propogate through the system without attenuation (see Fig. 8.1.) The low frequency amplifiers were replaced with two low noise HF amplifiers (Marconi Instruments TF 2175 and Mini-Circuits ZFL-500LN), which were cascaded to achieve a maximum gain of

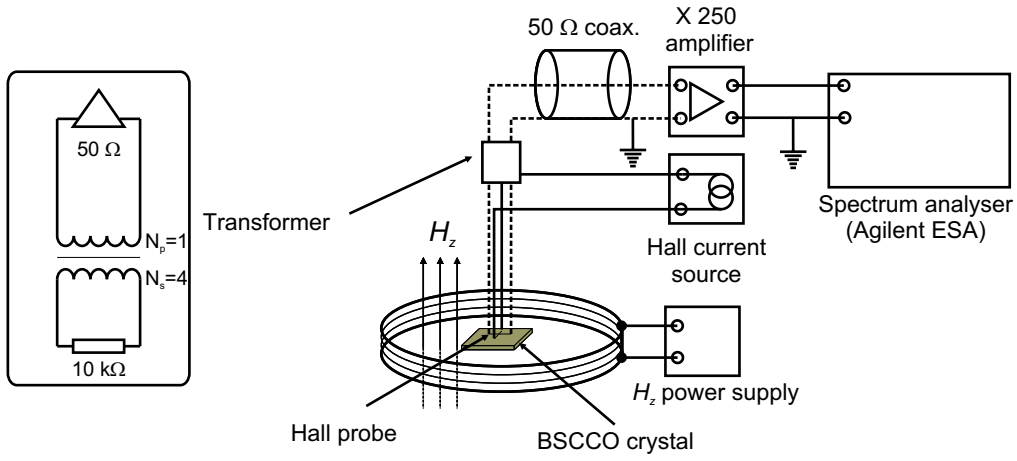

Figure 8.1: Schematic of the apparatus used to measure the high frequency flux noise spectrum at the surface of a BSCCO single crystal. The circuit shown in inset illustrates the function of transformer inserted to improve the impedance matching between the 50 Ω amplifier and the HP.

×250 across a bandwidth of 300 MHz. Unlike the input to the low frequency amplifiers, which were able to amplify the voltage difference across the Hall voltage lead, the input to the HF amplifier amplifies the Hall voltage with respect to ground. Hence one terminal of the Hall voltage leads was grounded in the HF experiments and, in order to avoid a short via ground to the current leads, the Hall current was driven with a battery powered current source with floating terminals.

The input impedance of the HF amplifiers is 50 Ω and the resistance of the AlGaAs/GaAs HP is typically 10 kΩ. It is a well known result from a.c. circuit theory that the power transferred from the source (HP) to the load (amplifier) is maximised when their impedances are equal. Thus in order to maximise the field resolution of the setup, the impedance match was improved by inserting a transformer between the HP and the amplifier. The parameter which controls the impedance (Z_{eqs}) seen by the amplifier is the turns ratio, which transforms the source impedance Z_s into an equivalent impedance given by the formula

$$Z_{eqs} = \left(\frac{N_p}{N_s}\right)^2 Z_s$$

where N_p and N_s are the number of primary and secondary turns. A transformer (TC16-1T) with a 4:1 turns ratio (reducing the mismatch by a factor of 16) was chosen and inserted close to the HP. The twisted wire pair used to connect the Hall voltage leads to the room temperature amplifiers was replaced with a miniature semi-rigid coax cable to connect the amplifier to the transformer. Tests carried

out to examine the low temperature behaviour of the transformer revealed that the operating bandwidth was shifted to lower frequencies, but the transformer still functioned well between 20 and 100 MHz. The transformer effectively isolates the amplifier from the d.c. component of the Hall voltage, so after installing the transformer it was not possible to use the Hall probe for measuring magnetisation curves.

8.3 Results

Figure 8.2 shows the local magnetisation at the surface of the BSCCO crystal measured as a function of the applied out-of-plane field at 82 K. At a field of approximately 35 Oe, the crystal is fully penetrated with flux and the vortex density increases at a constant rate. As a consequence, the magnetisation maintains an equilibrium value and the induction increases linearly with the applied field. A jump in the magnetisation occurs at 44 Oe, above which the magnetisation assumes a slightly higher value. The direction of the jump is positive and therefore corresponds to an increase in the local vortex density. This field is the the melting field H_m and its measured temperature dependence is plotted against temperature in Fig. 8.2. The linear temperature dependence of H_m is in good agreement with other studies [76, 92].

Fig. 8.3(a)-(b) shows the low frequency (1-100 Hz) spectral distribution of the HP voltage at two temperatures, 77 K and 89 K, for two values of H_z. Each curve was constructed by averaging 10 spectra at each field and took a total of 10 minutes to capture and process. It was not possible to take more averages over this frequency range because the HP can drift with time, making it difficult to isolate the effect of the applied field. The large NSPD below 100 Hz in Fig. 8.3(a) is characteristic of $1/\nu$ noise, which dominates the HP voltage spectrum at low frequencies in transport measurements. The shape of the $1/\nu$ distibution is clearly different at each temperature. However, it is uncorrelated with the applied field and is therefore related to the characteristic noise of the HP. The NSPD drops to a noise floor of approximately 100 μV/Hz$^{1/2}$ by $\approx$ 100 Hz. For a resistor with R=7 kΩ and temperature T=87 K, the Johnson noise due to

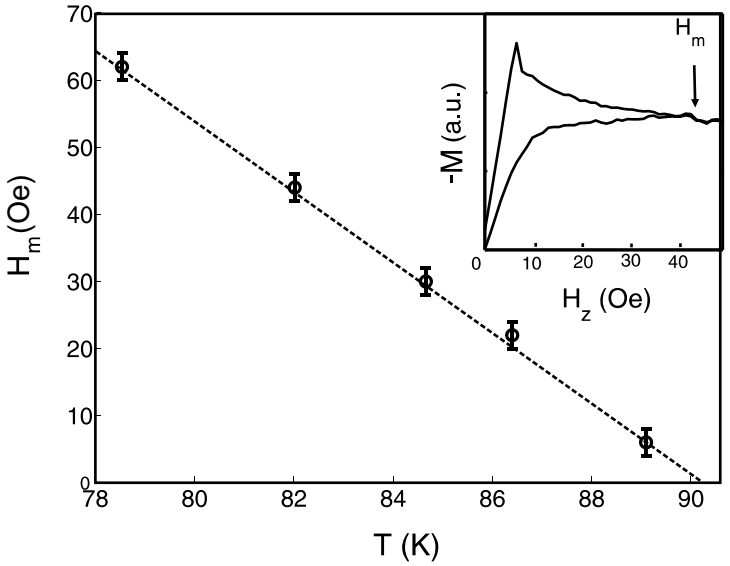

Figure 8.2: Plot of the temperature dependence of the melting field H_m. Open circles are the measured data and the dashed line is a guide to the eye. A typical magnetisation curve (T = 82 K) used to obtain the location of the melting field H_m is shown in inset and the arrow indicates the jump in the magnetisation.

thermal agitation of the 2DEG electrons is given by

$$V_{JN} = \sqrt{4k_B T R \Delta\nu}, \tag{8.1}$$

where $\Delta\nu$ is the bandwidth over which the voltage is measured. Therefore the component of the NSPD from the thermal noise

$$G \times V_N/\sqrt{\Delta\nu} = 10000 \times \sqrt{4k_B RT} = 57 \pm 10\ \mu V/Hz^{1/2},$$

where we have taken into account the $\times$10,000 gain of the amplifiers. The stated uncertainty arises from the value of the Hall resistance, which can vary with temperature and is not known with great accuracy. The predicted value is slightly lower than the measured NSPD, suggesting that the thermal noise is well coupled to the detection circuit. One would also expect the NSPD to be slightly higher than the Johnson noise floor because of the contributions from other noise sources. The insets shown in Fig. 8.3 are spectra which have been normalised with respect to the spectrum in zero field and plotted on logarithmic axes. All of the spectra are distributed around 1, and for clarity only one normalised spectra has been presented.

The NSPD as a function of frequency over the range of intermediate frequen-

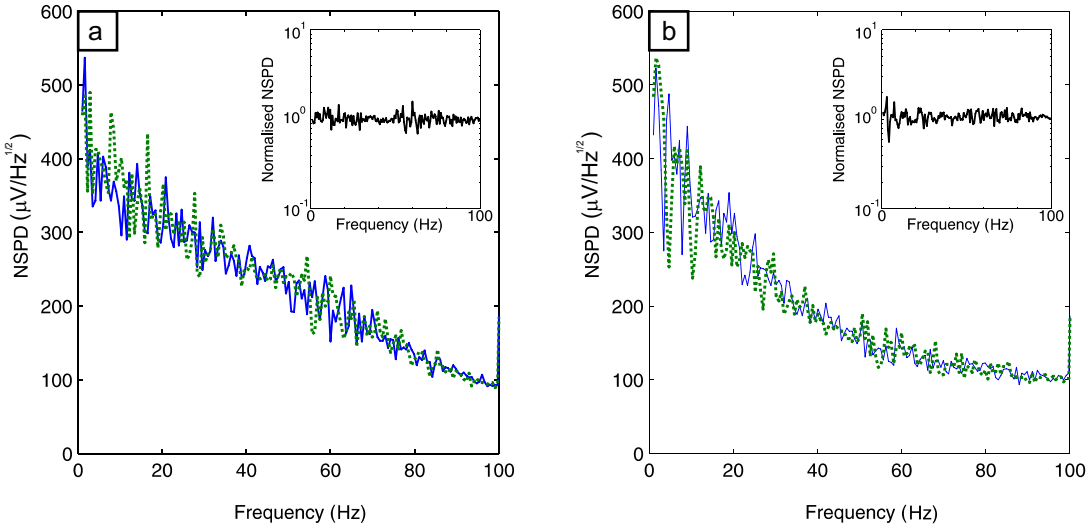

Figure 8.3: Examples of noise spectral power density (NSPD) as a function of frequency between 1-100 Hz. (a) T=77 K,H_z=0 (blue) and H_z=10 Oe (green). (b) T=89 K for H_z=0 Oe and H_z=8 Oe. The spectra shown in the insets are normalised with respect to the zero-field spectrum.

cies between 100 Hz and 50 kHz is shown in Fig. 8.4. In this experiment it was possible to capture the higher frequency spectra at a higher sampling rate, so these curves represent the mean of 500 spectra. Apart from the high NSPD around 100 Hz, which is caused by external mains interference, the NSPD noise floor drops to an approximately constant $\approx 60\ \mu\mathrm{V/Hz}^{1/2}$, and at 85 K is $\approx 0.25\ \mu\mathrm{V/Hz}^{1/2}$ higher than at 77 K. This is in good agreement with the calculated Johnson noise value and demonstrates that thermal noise dominates the NSPD within this range. There is a small attentuation of the NSPD towards 50 kHz due to the roll off of the amplifier gain. It can be seen that the normalised NSPD is again close to 1 for all values of the applied field. Hence over these two ranges of frequency the NSPD is unaffected by changes in the magnetic field, at least to within the resolution limits of this experimental setup. The limit arising from the noise and drift in the spectra is approximately 5 $\mu\mathrm{V/Hz}^{1/2}$, which is equivalent to a field of B = 10^{-4} G/Hz$^{1/2}$ field equivalent noise or $\approx 10^{-5}\Phi_0/\mathrm{Hz}^{1/2}$. However, the fundamental limit is set by the field resolution of the HP, which is approx $10^{-4}\Phi_0/\mathrm{Hz}^{1/2}$.

The curves which have been presented are typical of all the measurements taken at temperatures between 77 K and 90 K, implying that either the attempt frequency is beyond this range, or that the Hall probe to sample spacing is too

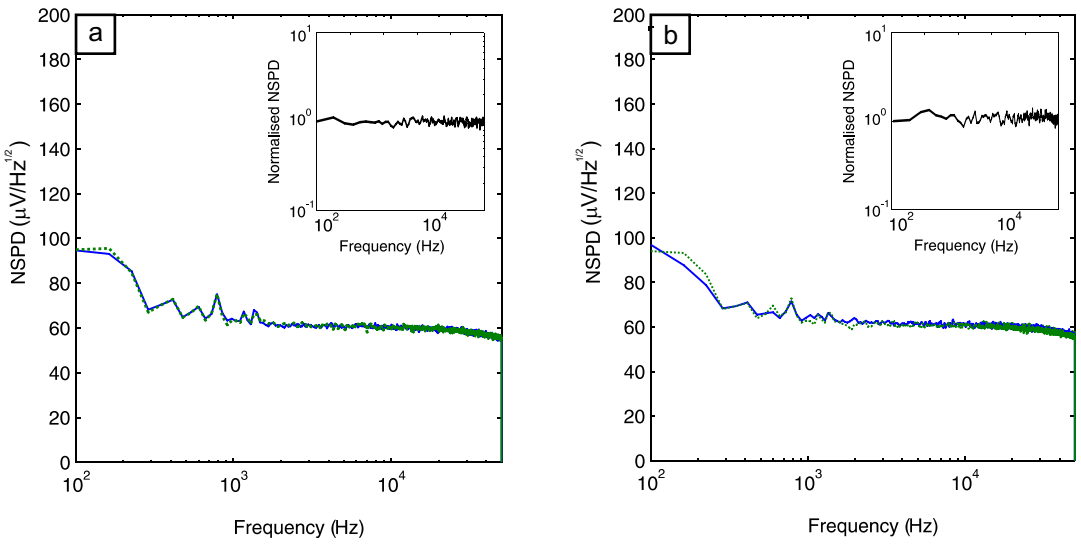

Figure 8.4: Examples of the NSPD as a function of frequency at intermediate frequencies between 100 Hz - 50 kHz for (a) $T = 79$ K ($H_m = 60$ Oe), $H_z = 58$ Oe (blue) and $H_z = 65$ Oe (green). (b) $T = 85$ K ($H_m = 30$ Oe), $H_z = 28$ Oe and $H_z = 35$ Oe. The spectra shown in the insets are normalised with respect to the zero-field spectrum.

large to resolve the fluctuations of individual vortices. Alternatively, the energy associated with the fluctuation of vortex positions may be distributed over such a broad range of frequencies that the contribution to the noise integrated over a small (≈ 100 Hz) bandwidth is lower than 5 μV/(100 Hz)$^{1/2}$ and thus cannot be resolved.

In an effort to detect the vortex fluctuations at higher frequency, as is suggested by the work of Brandt [40], the apparatus was modified in the manner described in section (8.2) to allow the propagation of 1-300 MHz signals. Because the HF amplifiers only produce a net gain of around 250, which is an order of magnitude lower than the LF amplfiers, the sensitivity of the HP in this experiment was enhanced by increasing the Hall current. The main panel of Fig. 8.5 shows difference spectra, i.e., spectra captured at a given current with the background zero-current spectrum subtracted, for the HP driven by different Hall currents. The peak in the NSPD increases with increasing Hall current below around 10 μA and then reaches a plateau, as can be seen from the plot in the inset of Fig. 8.5. This result is reminiscent of microwave oscillations induced by driving a d.c. current through a semiconductor, although here the frequency is much lower, and serves to confirm that the noise spectra at these frequencies is still dominated by noise from the Hall probe itself, rather than external sources. This is supported further by the fact that the greatest increase of the NSPD occurs in the range

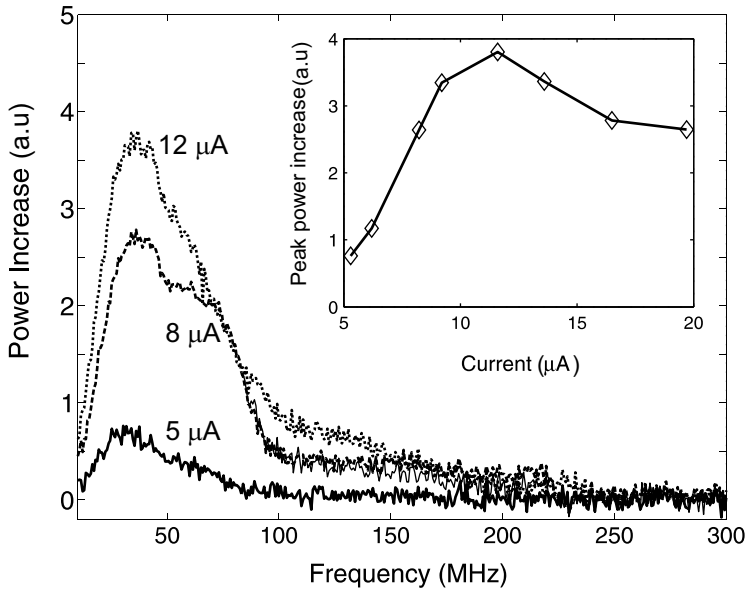

Figure 8.5: Plot showing the increase in the NSPD arising from the Hall current for three currents ($T = 77$ K, $H_z = 0$.) The plot in inset shows the power increase at the 50 MHz peak as a function of the Hall current.

between 10 MHz and 100 MHz, where the impedance transformer operation is optimal. However, this effect possibly compromises the ability to detect small fluctuations in the Hall voltage due to changes in the field, and was not investigated in further detail. The NSPD diminishes rapidly beyond 100 MHz due to the roll off of the gain of the amplifiers. Based on these results, the Hall current was set to 5 μA and the crystal was cooled to $T = 82$ K. NSPD spectra were captured between 10 and 100 MHz where the operating bandwidths of the amplifiers coincides with the transformer. Figure 8.6 shows the measured frequency spectra for several fields above and below the melting field. In this experiment, the field was increased in steps of 2 Oe up to 40 Oe and frequency spectra captured and averaged 1000 times at each field. The magnitude of the NSPD is $\approx$ 1 μV/Hz$^{1/2}$, which is an order of magnitude smaller than the lower frequency value, as is expected from the lower gain of the amplifiers. The Johnson noise is uniformly distributed over all frequencies, and should therefore be the same at both low and high frequencies. To make an accurate comparison between our values obtained from the separate frequency ranges it would be necessary to allow for the lower gain (250) and internal noise of the HF amplifiers, the loss of power due to inserting the transformer, and the variation in the resistance of the Hall leads, since all of these will affect the NSPD. However, none of these are known in great detail, so it is only possible to make a rough comparison. This is also less important in our study because we are interested in relative changes in the

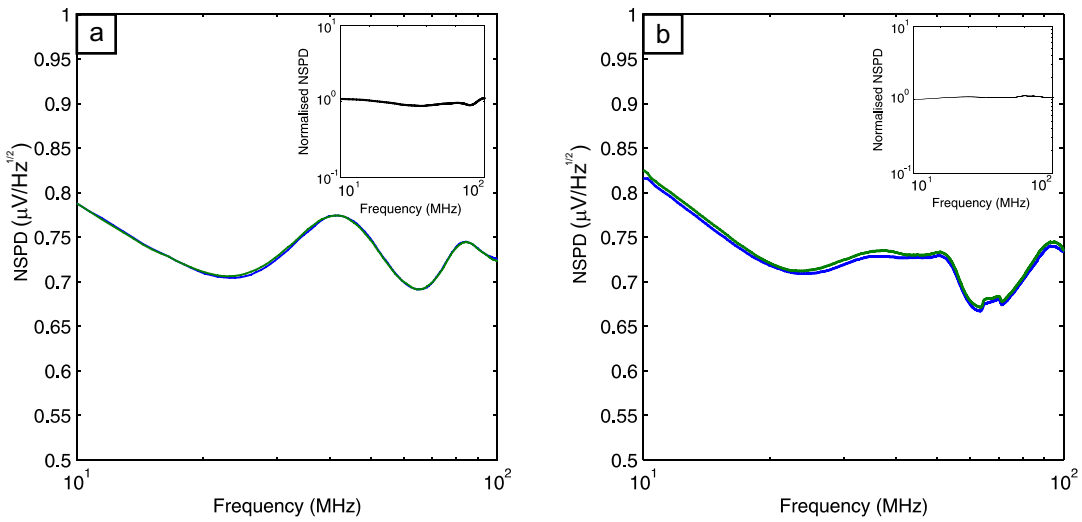

Figure 8.6: NSPD as a function of frequency between 10 and 100 MHz for a range of fields above and below the melting field. (a) $T = 81$ K ($H_m = 50$ Oe) (b) $T = 85$ K ($H_m = 30$ Oe.) The spectra shown in the insets are normalised with respect to the zero-field spectrum at each temperature.

noise spectra due to the presence of vortices.

There are several striking features of the spectra which reveal some of the complications that arise when making high frequency flux noise experiments with 2DEG HPs. The most obvious feature is the corrugation in the NSPD with frequency. This is caused by the impedance mismatch between the HP and the 50 Ω coaxial line, resulting in reflection and associated standing waves at resonant frequencies, and is an unavoidable consequence of exploring high frequency signals with intervening transmission lines. The overall decrease in the NSPD with frequency is due to the gradual roll off of the amplifier gain. In addition, the impedance of the transformer is also a function of frequency and consequently alters the impedance match between the amplifier and the HP. The average noise level is lower at 81 K than at 85 K, thus confirming that the noise floor is dominated by the thermal noise of the HP, as this is the only component of the setup which is affected by the temperature. The data taken at different fields at 85 K exhibit differences which are uncorrelated with the applied field, suggesting they arise from other sources. Upon close inspection of the normalised NSPD spectra, no systematic correlation with the applied field was found superimposed on these features at either temperature, and we can therefore make the same conclusions as were made regarding the low and intermediate frequency data.

Chapter 9

Conclusions and Future Prospects

9.1 Magneto-Optical Imaging of Flux Penetration into Arrays of BSCCO Micro-disks

Arrays of micro-disks were fabricated at the surface of BSCCO single crystals and magneto-optical imaging used to investigate how the penetration field of the disks depends on their temperature and location with respect to underlying linear disorder in the crystal. A quantitative comparison was made with the prediction for the penetration field based on the theory of thermal activation of pancake vortices over the Bean-Livingston barrier, yielding a value for the characteristic temperature T_0 = 19 - 25 K, which is in good agreement with previous studies. The penetration field was found to be higher for the smaller diameter disks, showing that demagnetising fields are still important in these structures and the estimated field enhancement at the edge is closest to that for a disk with a rectangular cross-section, $R = \sqrt{d/2W}$. The penetration field was shown to be lower at the edge of linear defects, suggesting that the BLB is suppressed by this form of quenched microscopic crystalline disorder. We conclude that Magneto-optical imaging is a powerful tool for exploring the interaction between surface barriers and correlated disorder in superconductors, and offers a promising way of systematically investigating the effect of different types of defects in a wide

range of microfabricated superconducting shapes.

9.2 Anisotropic Pancake Vortex Transport in BSCCO Crystals

Micro-Hall probe magnetometry was used to investigate how the local c-axis magnetisation of a BSCCO single crystal is influenced by the strength and direction of an in-plane field. With the in-plane field along the crystalline b-axis of the crystal, the irreversibility falls linearly as $\sqrt{H_{||}}$, suggesting that it is simply proportional to the lateral JV stack density. In contrast an increase in the out-of-plane irreversible magnetisation is observed as the in-plane field is increased along the a-axis up to $\approx$ 15 Oe. This result is surprising, since the presence of JVs is usually assumed to suppress the irreversible magnetisation, and is explained within the crossing lattices picture by considering the dynamics of PVs along JVs which are indirectly pinned on linear defects. The maximum in irreversibility near $H_{||}$ =15 Oe suggests that the JV stack spacing is quasi-commensurate with the mean lateral spacing of linear defects at this field, leading to an estimate for the average LD spacing of $\approx$ 20 μm, in good agreement with other measurements. When the angle between the in-plane field and the a-axis is increased in a positive sense we find that the irreversibility exhibits distinct shoulders around 55° and 235° which, in combination with SHPM images of the vortex structure under similar experimental conditions, leads us to conclude that these angles are connected to the critical accommodation angle predicted by vortex trapping theory. The out-of-plane magnetisation depends on the history of the prepared in-plane field state, indicating that there is irreversibility associated with the trapping process which makes it depend on the sense of rotation. The suppression of the irreversibility is a fairly weak function of angle at low temperatures, when the interaction between the crossing sub-lattices is weak in comparison to bulk PV pinning forces, but can lead to a reduction of ΔM_z by a factor of four at high temperatures when the system is dominated by channelling along JVs. We conclude that the out-of-plane irreversibility of BSCCO single crystals is a sensitive measure of correlated anisotropic disorder over a wide range of temperatures in the crossing lattices regime.

9.3 Continuum Versus Discrete Flux Behaviour in BSCCO Micro-disks

SHPM was used to measure the distribution of flux at the surface of individual BSCCO micro-disks. The growth of the flux dome in disks of 20 μm diameter was measured and its observed expansion was fitted using analytic continuum models. The latter models failed however to describe flux penetration in 10 μm disks, in which the compression of small vortex clusters was observed in increasing fields. Even at higher fields where the continuum model regains validity, the system continues to exhibit discreteness through characteristic features on the magnetisation curves. These measurements, in combination with numerical simulations, allow us to identify the magnetic signatures of individual vortices penetrating the centre of the disk, the assembly process of vortices into different shell formations, and the collective locking of flux lines into configurations which are simultaneously triangular and concentric. Finally, the competing effects between Abrikosov lattice and shell-like ordering have allowed us to develop an analytic criterion which places the "large mesoscopic" regime for superconducting disks at radii between 10λ and 20λ. This is the first experimental study which is able to demonstrate both macro- and mesoscopic behaviour of large mesoscopic high-T_c superconducting disks, showing that SHPM combined with local Hall magnetometry is a valuable technique for investigating vortex configurations in large mesoscopic superconductors.

There are a number of natural extensions of this work. In the BSCCO system, for instance, the size and shape of the mesostructures could be systematically varied to establish the effect of shape on the meso-to-macro crossover point, and whether different types of ordering are also visible in local magnetisation curves. A particularly rich source of new physics is expected from BSCCO mesostructures in tilted fields, where the attraction between out-of-plane pancake vortices and in-plane Josephson vortices competes with the effects of topological confinement. Through a simple modification of the fabrication procedure it would also be possible to invert the structure to produce arrays of "anti-pillars" (i.e. holes), in which in-plane effects would be particularly prominent. Finally, the SHPM could be used to gain valuable insight into large mesoscopic structures fabricated from other single crystal and thin film superconductors.

9.4 Thermal Fluctuations of Vortex Positions in BSCCO Single Crystals

Micro-Hall probe magnetometry was used to measure the time dependence of the surface field of a BSCCO single crystal over a range of temperatures close to T_c and out-of-plane fields above and below the vortex lattice melting field. The melting field was measured as a function of temperature and showed an approximately linear variation which is in good agreement with other studies. The noise from the Hall probe at intermediate frequencies is close to the noise floor produced by thermal Johnson noise in the 2DEG, and no correlation has been found between the frequency spectra and the applied magnetic field over the range of both low, intermediate, and high frequency bands. The standard apparatus for obtaining d.c. magnetisation curves using a Hall probe was modified to measure a.c. Hall voltages up to 100 MHz and the impact of these modifications on the measured data have been identified. The null result reported in this work is attributed to a combination of factors. These include, for instance, the spacing between the HP and the sample, the field resolution of our apparatus, the noise from external sources, and finally the possibility that the characteristic vortex frequency is beyond 100 MHz.

Several directions are recommended for future research. Since the high resistance of the HP represents a fundamental limit to the detection of HF signals with high signal-to-noise ratio, it is unlikely that the high frequency performance of the apparatus can be improved through further structural modifications. A lower resistance HP could be used to improve impedance matching, but in practice this means increasing the active area of the HP and would consequently reduce the sensitivity to individual vortex motion. Hence it is recommended that the lower frequency regime should be examined again and ways developed to reduce the sample to sensor separation. This would most easily be accomplished by approaching the sample surface using SHPM.

Appendix A

Disk Fabrication

An optimally doped BSCCO single crystal grown using the travelling solvent floating zone technique[1] in the form of a large (5 mm $\times$ 5 mm $\times$ 100 μm) rectangular platelet was cleaved and divided into four pieces using a diamond impregnated wire saw. A thin coating of epoxy was made at one end of a Si chip (5 mm $\times$ 5 mm) over an area slightly smaller than a piece of the crystal. The crystal was blown gently from above to make it lie flat on the epoxy and set in place by baking the sample for 20 minutes at 100°C. Higher temperatures were avoided because annealing alters the oxygen content, and hence the critical temperature, of BSCCO crystals. The Si chip was then stuck to a glass coverslip, which was used to manipulate the chip during subsequent lithography steps, and the surface of the crystal gently cleaved using adhesive tape to leave a clean flat surface ready for processing.

Fig. A.1 shows the main stages (A-E) used to cleave and prepare a thin flake from the crystal for patterning. A small bead of SU8-50 photoresist was dropped onto the crystal and spun at 1250 r.p.m. to achieve a 100 μm layer. The sample was then placed at the centre of the spinner so that the dome of photoresist was directly over the crystal (stage A.) After spinning, the photoresist solvent was evaporated by baking on a hotplate for 10 minutes at 65°C and 95°C for 30 minutes. A block of photoresist was exposed over the crystal using a window mask made from a glass plate and black adhesive tape (B). The window was slightly smaller than the crystal to compensate for diffraction at the edges. A relatively

[1]Courtesy of Prof. T. Tamegai (University of Tokyo.)

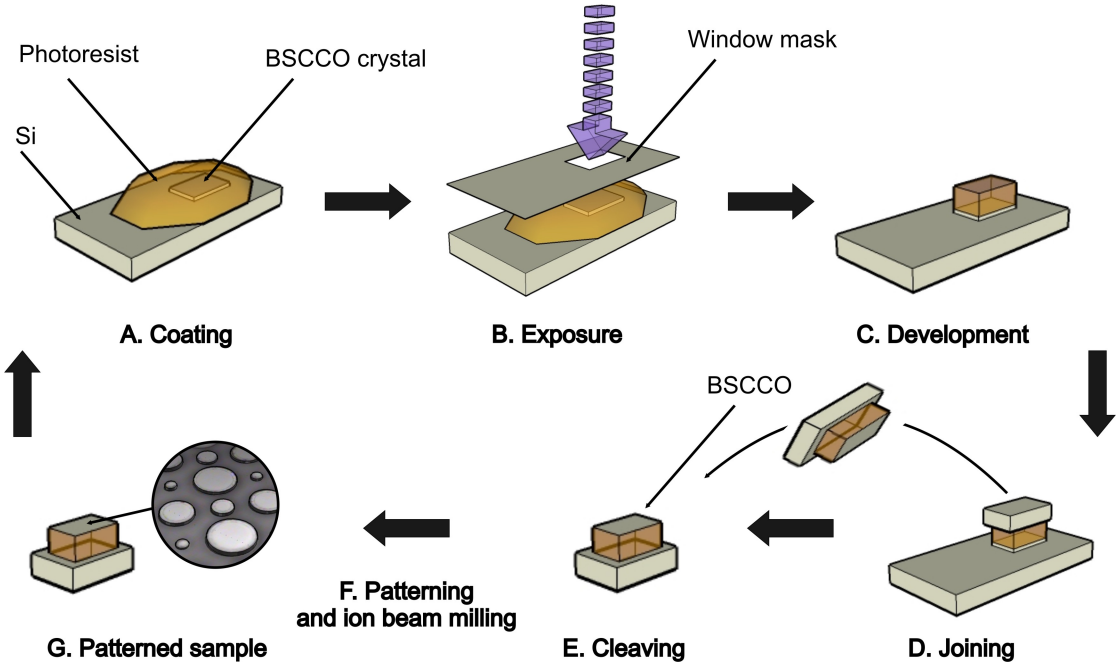

Figure A.1: Stages of patterning disks in a BSCCO single crystal. The first "cleave and pattern" method starts at stage A and ends at stage G, while the "pattern and cleave" method begins at F and ends at E (via A).

long exposure ($\approx$ 3 min) time was used to render the photoresist completely insoluble. After a post exposure bake of 1 minute at 65°C and 10 minutes at 95°C, the (unexposed) soluble regions of photoresist were removed in EC solvent for approximately 6 minutes, leaving the block of photoresist that was exposed over the crystal ready for cleaving (C).

To cleave a flake from the crystal, a small drop of epoxy was placed on the block of SU8-50 using a scalpel blade. As little epoxy as possible was used in order to avoid any running over the edge of the block. A piece of Si was then gently dropped on to the block and set by baking at 100°C for 20 minutes (D). The small piece of Si was then levered from the surface, cleaving with it a flake of BSCCO (E). If the remaining crystal was sufficiently thick, it can be processed repeatedly using this method to obtain several samples.

To pattern the disks into the flake, it was coated with photoresist, patterned using photolithography, and etched using Argon ion milling (F), as is illustrated in Fig. A.2(b). The choice of photoresist was determined by the desired thickness of the disks. Thicker disks needed to be etched longer, thus requiring a thicker or harder photoresist to survive for the duration of the etching process. The three

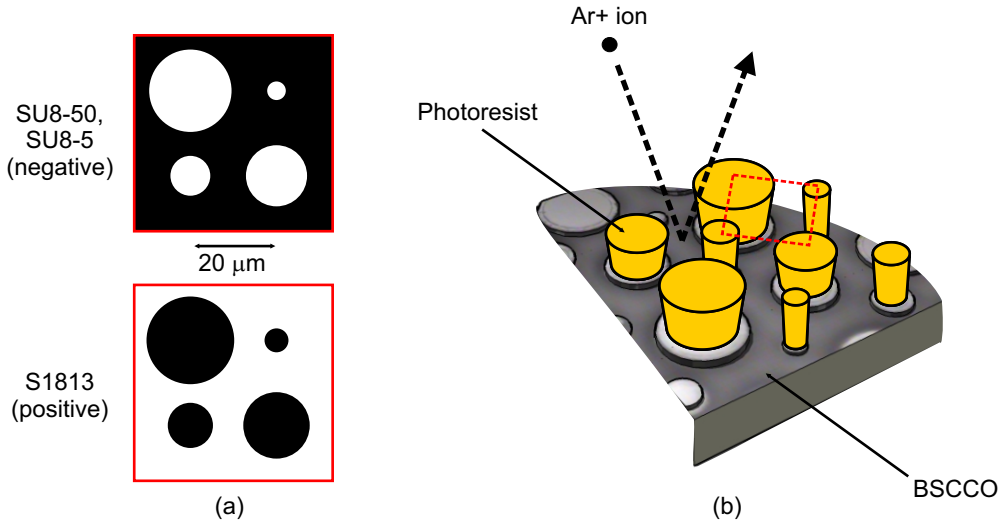

Figure A.2: (a) Optical mask design for the disk array consisting of 5/10/15/20 μm diameter structures arranged in a square unit cell. The thicker SU8 series of photoresist is negative, which requires windows in the mask where the disks will be exposed, whereas the S1813 is positive and requires the disks to be covered.(b) Illustration showing the Ar+ milling process. The slight tapering of the photoresist pillars leads to the redeposition of material around the base visible at the edge of the disks in Fig.5.1

types of resist used in this work were SU8-50, SU8-5, and S1813. SU8-50 was spun at 5000 r.p.m. to produce a 18 μm layer (baked at 1 minute at 65°C and 95°C for 10 minutes.) Later samples were made using SU8-5 spun at 3500 r.p.m. to produce a 10 μm layer (baked at 2 minute at 65°C and 95°C for 5 minutes.) For the thin disks investigated in this work, S1813 spun at 3500 r.p.m. yielded a 1 μm thick layer, which just sufficed for milling to around 300 nm.

In all cases, an optical mask, consisting of a periodic array of 5/10/15/20 μm disks arranged in a square unit cell, was brought into contact with the photoresist using a mask aligner. The SU8 series of resists are negative, which means they are rendered insoluble on exposure, whereas S1813 is a positive resist and behaves in the opposite manner. The positive and negative masks are shown in Fig. A.2(a). Good contact between the mask and the photoresist is essential to avoid exposing the photoresist between the disks to UV radiation. This risk was reduced by using shorter exposure times, but if the exposure time was too short the pillars can become tapered during development, leading to the redeposition of material at the edge of the disks. After coating and exposure, the SU8 series of photoresists require a two step post exposure bake (PEB) in order to harden the exposed regions. For SU8-50, a PEB of 1 minute at 65°C and 95°C for 5 minutes was used; for SU8-5, a PEB time of 2 minutes at 70°C is sufficient. The regions

of SU8 photoresist were then removed by vigorously stirring the sample in EC solvent for approximately 10 s, or for around 30 s in standard developer for S1813.

The disks were dry etched using Ar+ ion beam milling (Ar-IBM). Ar-IBM involves extracting Argon ions from a plasma and accelerating them towards the sample, where they impact and erode the sample surface by momentum transfer [see A.2(b).] It was discovered during preliminary experiments using Si and graphite that several factors control the quality of the etch. The two main ones are beam shadowing by the photoresist pillars, which leads to tapering of the disk side walls, and the redeposition of etched material, which leads to a lower quality surface at the edges. Efforts were made to minimise these effects by mounting the sample on a rotating holder whose axis was tilted at around 10° from the incident beam. The etch rate for BSCCO using Ar-IBM with a beam voltage of 500 V and a beam current of 20 mA is 15 nm/min. In practice the temperature of the sample was kept low by allowing the miller to cool for 10 minutes after 5 minutes of milling.

Appendix B

Vortex Resolved SHPM Images

Due to the surface debris on the disks analysed in chapter (7), it was not possible to approach close enough to the surface to resolve individual vortices. As a result, the evidence for the formation of vortex structures was largely indirect. In this Appendix, we briefly discuss the results obtained using SHPM to investigate a second type of disk sample in which vortices were directly imaged. This second disk sample was fabricated using a "pattern and cleave" technique (in contrast to the "cleave and pattern" technique used to fabricate the first type,) which begins by directly patterning the crystal in stage F and goes through stages A to E of Fig. A.1, thereby ending in disks on the underside of the flake. This second fabrication method has the advantage of producing a freshly cleaved surface, which is ideal for scanning with SHPM. However, the Hall probe is sensitive to the stray fields from the material between the disks, making the images more difficult to interpret.

The disk array was patterned using thicker photoresist pillars of SU8-50 in the same cell design and then etched to a depth of $\approx$ 750 nm. A typical region of the sample is shown in the optical micrograph of Fig. B.1(a) together with a depiction of its structure in Fig. B.1(b) In our first experiment the surface was approached and images captured at the surface at $T=$ 77 K. In SHPM images, vortices appear as micron sized concentrations of magnetic flux, as shown in the inset image of Fig. B.2. Due to the high spatial and field resolution of the SHPM it is possible to make a quantitative comparison with theoretical estimates for the field profile by taking a radial line scan of the vortex. Since the size of the

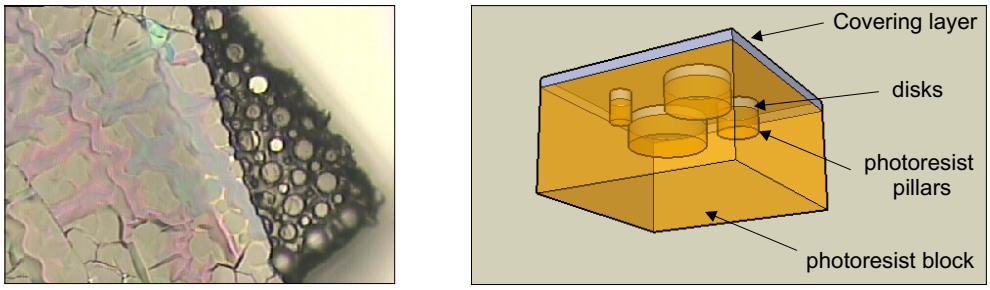

Figure B.1: (a) Micrograph of the surface of a sample fabricated using the second method. The removal of the covering layer at the corner as the block of photoresist was stripped from the patterned crystal allows us to see the disks embedded in the photoresist. (b) Illustration of the cell of the second sample. It was not possible to control the thickness or uniformity of the covering layer, but it likely to be < 1 μm thick.

HP is of the same order of the vortex, the simple theoretical expression for the field distribution around an isolated vortex given by the solution to the London equation (see, for example, Ref. [21]) must be modified to account for the response function of the HP and the height at which it scans over the vortex [54]. It can be shown that the radial field distribution of a vortex detected by a HP at a height z above the centre of a film with thickness d is given by

$$B(r,\lambda,z) = \frac{\phi_0}{2\pi\lambda^2}\int_0^\infty \frac{J_0(\gamma r)\exp\gamma(|z|-d/2))d\gamma}{k_\gamma(\coth(k_\gamma d/2)+k_\gamma/\gamma)}, \tag{B.1}$$

where λ is the bulk penetration depth and $k_\gamma = (\gamma^2 + 1/\lambda^2)^{1/2}$. This equation was numerically solved and the parameters were manually adjusted to determine the best fit to the data. The solution with z=1.1 μm, λ=350 nm, and d=1 μm is plotted as a dashed line in Fig. B.2. Since none of these parameters are known in detail and vary from experiment to experiment, we are unable to make a detailed quantitative comparison. However, the solution yields a good qualitative reproduction of the measured data with parameters which are of the correct order of magnitude, thus establishing that the object is a flux quantised vortex.

It was possible to resolve the penetration of individual vortices into a 20 μm diameter disk and thus analyse directly the effect of the free surfaces of the disks on the vortex lattice. Fig. B.3 shows the evolution of the vortex lattice inside the disk with increasing applied field at 77 K. Although debris in the lower half restricted us to the top half of the scan window, a number of vortices are clearly

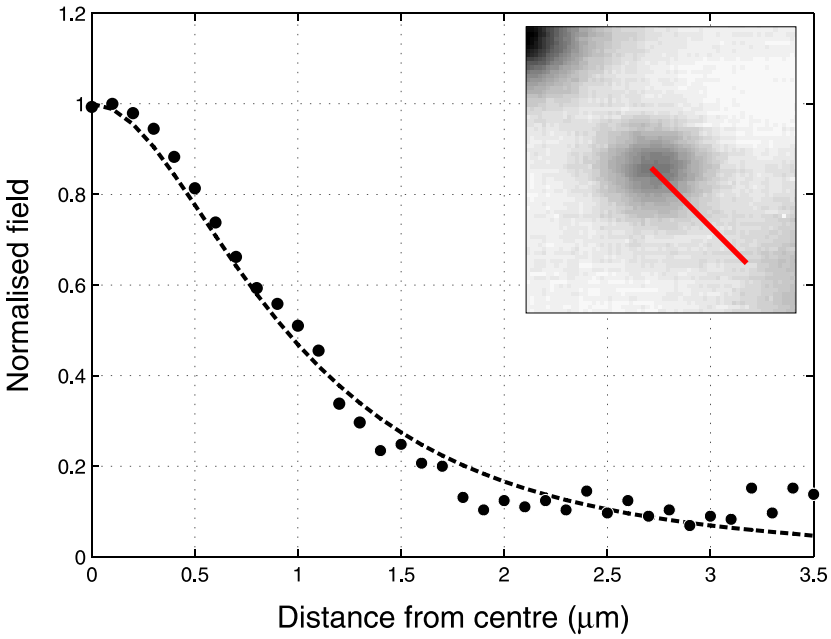

Figure B.2: Field profile along the line shown in the inset image (6 μm × 6 μm) of a single isolated vortex. The filled circles are the measured data and the dashed line is a fit based on equation B.1

recognisable in the central region of the image. The nucleation site for the vortices is along the right hand edge of the image, where a strong concentration of the applied field is also visible. At low fields, when the inter-vortex spacing is large, the vortices begin to form a disordered lattice whose orientation changes with the addition of each vortex. The change in field required to introduce each vortex is $\Delta H \approx 0.2$ Oe, which corresponds to the field expected for vortex nucleation in a 20 μm disk, and there appears to be no surface barrier to vortex entrance. It is highly likely that the surface barrier in this disk is destroyed by a defect and that vortices are consequently able to enter even at low fields. Because the vortices enter gradually, they form a lattice distributed throughout the disk rather than the central vortex dome that was seen in the previous sample.

By $H_z = 3$ Oe, a definite orientation of the vortex lattice has emerged, with one of the lattice vectors following the curvature of the edge of the disk. Towards higher fields the proximity of vortices means that their field distributions begin to overlap and we are unable to distinguish between neighbouring vortices. The images in $H_z = 5.1$ Oe and $H_z = 5.7$ Oe do seem to show a change to a different structure along the right hand edge. These observations are in good agreement with theoretical studies which predict a shell-triangular structure of vortices near

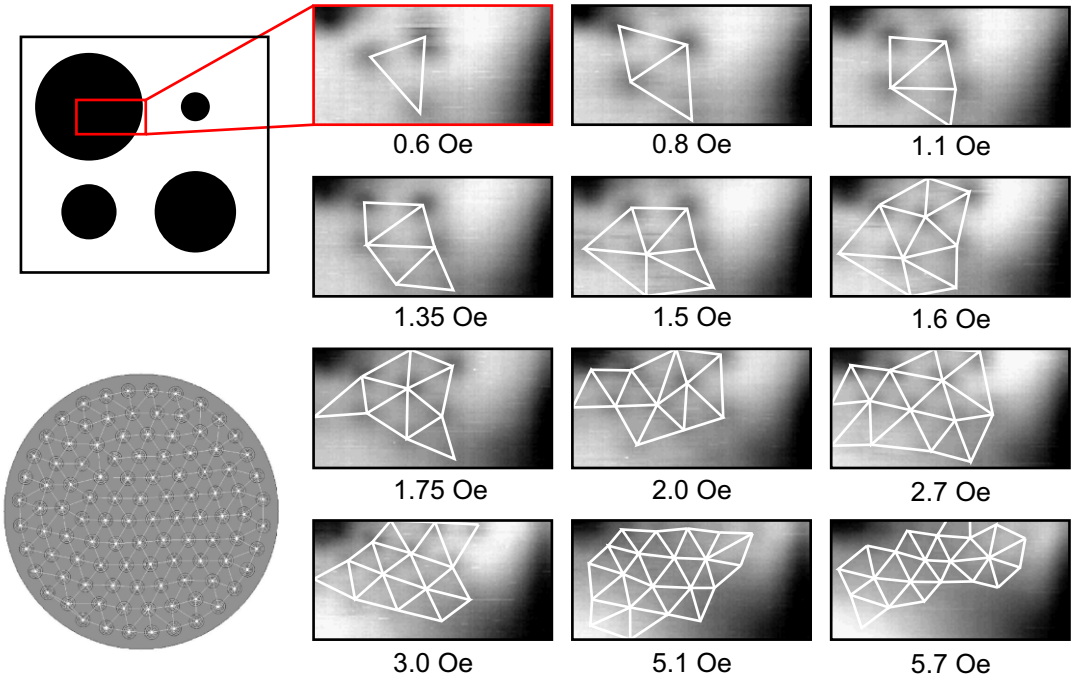

Figure B.3: Raw single scans (13 μm × 6.5 μm) of the edge of a 20 μm disk captured in increasing applied field. The approximate location of the scan in relation to the disk is indicated in the upper right diagram. The white lines join the positions of each vortex to its nearest six neighbours. Vortices enter from the edge of the disk on the right and gradually form a mixture of an Abrikosov lattice at the centre of the disk and rings or shells at the edge. The lower left image shows the solution to the GL simulation with 44 vortices [reproduced from [6]]

the edge, where the currents strongly interact with the vortex currents [6]. The image on the lower left depicts the solution to the GL equation that was obtained by Cabral *et al.* for a large thin disk ($W = 50\xi$) with 44 vortices. Our images confirm the key features of the simulation. However, the lattice in our images seems to follow the edge of the disk, even away from the edge, whereas the simulation suggests a sharper boundary between the shell structures at the edge and the Abrikosov lattice at the centre. Finally, the absence of any surface barrier to vortex penetration allows us to image the vortex lattice and hence determine the lattice constant even at small fields. For an infinite triangular lattice in a thin film, the relation between the lattice constant a and the flux density is theoretically given by [17]

$$B = \frac{2}{\sqrt{3}} \frac{\Phi_0}{a^2} \tag{B.2}$$

where a is the lattice constant. In Fig. B.4, the inverse square of the inter-vortex spacing is plotted as a function of the flux density (numerically equal to the applied field.) Also shown is the theoretical fit given by Eq. (B.2). The value

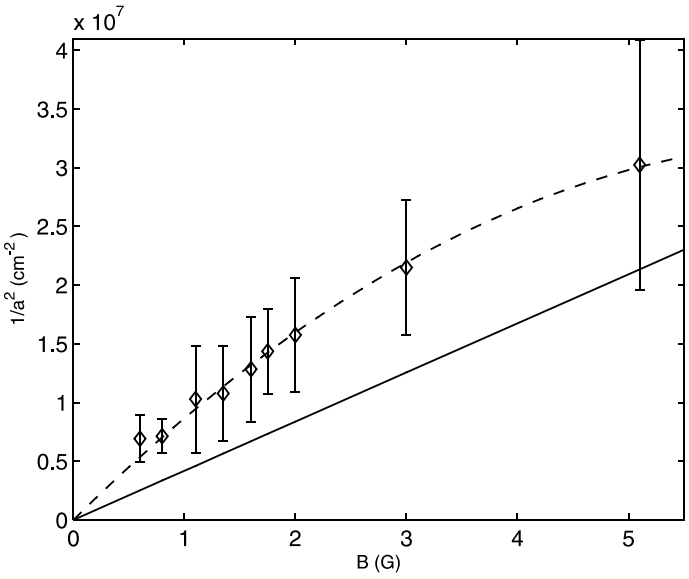

Figure B.4: Plot showing the linear relation between the inverse square of the lattice constant and the flux density. The dashed line is a line of best fit and the error bars are equivalent to one standard deviation from the mean. To deduce the standard deviation $\Delta(1/a^2)$, we calculate Δa from the distribution of values for the side lengths and then use $\Delta(\frac{1}{a}\frac{1}{a}) = -\frac{2}{a^3}\Delta a$. The continuous line is given by equation (B.2)

of the lattice vector is consistently smaller than expected. This is a surprising result, since at low fields, when the intervortex repulsion is less, one would expect the lattice constant to be greater than for an infinite lattice. Hence we conclude that the edge is compressing the lattice, in good agreement with the results of chapter (7).

Appendix C

List of Publications

The work described in this thesis has led to the following publications:

M. R. Connolly, M. V. Milošević, S. J. Bending, J. R. Clem, and T. Tamegai, Continuum versus discrete flux behaviour in large mesoscopic $Bi_2Sr_2CaCu_2O_{8+\delta}$ disks. (submitted to *Europhys. Letts.*)

M. R. Connolly, M. V. Milošević, S. J. Bending, and T. Tamegai, Magneto-optical imaging of flux penetration into arrays of $Bi_2Sr_2CaCu_2O_{8+\delta}$ micro-disks. (submitted to *Phys. Rev. B.*)

M. R. Connolly, S. J. Bending, A. N. Grigorenko, and T. Tamegai, Anisotropic pancake vortex transport in the crossing lattices regime of $Bi_2Sr_2CaCu_2O_{8+\delta}$ single crystals. *Phys. Rev. B* 72:224504, 2005.

References

[1] N. Nakamura, G. D. Gu, and N. Koshizuka. Field Induced 3D to 2D Crossover of Shielding Current Path in $Bi_2Sr_2CaCu_2O_x$. *Phys. Rev. Lett.*, 71(6):915, 1993.

[2] E. Zeldov, A. I. Larkin, V. B. Geshkenbein, D. Majer M. Konczykowski, B. Khaykovich, V. M. Vinokur, and H. Shtrikman. Geometrical Barriers in High-Temperature Superconductors. *Phys. Rev. Lett.*, 73:1428, 1994.

[3] J. A. Aguiar L. R. E. Cabral, C. C. de Souza Silva and E. H. Brandt. Geometric barrier in $Bi_2Sr_2CaCu_2O_{7+\delta}$ single crystals. *Phys. Rev. B*, 65:134514, 2002.

[4] A. V. Kuznetsov, D. V. Eremenko, and V. N. Trofimov. Onset of flux penetration into a type-II superconductor disk. *Phys. Rev. B*, 56(14):9064–9070, 1997.

[5] N. Morozov, E. Zeldov, M. Konczykowski, and R. A. Doyle. Geometrical and distributed surface barriers in $Bi_2Sr_2CaCu_2O_8$. *Physica C*, 291:113, 1997.

[6] L. R. E. Cabral, B. J. Baelus, and F. M. Peeters. From Vortex Molecules to the Abrikosov lattice in thin mesoscopic superconducting disks. *Phys. Rev. B*, 70(14):144523, 2004.

[7] L. Burlachkov. Magnetic relaxation over the Bean-Livingston surface barrier. *Phys. Rev. B*, 47(13):8056–8064, 1993.

[8] N. Chikumoto, M.Konczykowski, N. Motohira, and A. P. Malozemoff. Flux-creep crossover and relaxation over surface barriers in $Bi_2Sr_2CaCu_2O_8$ crystals. *Phys. Rev. Lett*, 69:1260–1263, 1992.

[9] Y. M. Wang, A. Zettl, S. Ooi, and T. Tamegai. Vortex penetration into micron-sized $Bi_2Sr_2CaCu_2O_{\delta+8}$. *Phys. Rev. B*, 65:184506, 2002.

[10] R. A. Doyle, S. F. W. R. Rycroft, C. D. Dewhurst, E. Zeldov, I. Tsabba, S. Reich, T. B. Doyle, T. Tamegai, and S. Ooi. The effect of sample shape on the magnetisation in $Bi_2Sr_2CaCu_2O_{8+\delta}$ crystals. *Physica C*, 308:123, 1998.

[11] V. A. Schweigert, F. M. Peeters, and P. Singha Deo. Vortex Phase Diagram for Mesoscopic Superconducting Disks. *Phys. Rev. Lett*, 81(13):2783, 1998.

[12] I.V. Grigorieva, W.Escoffier, J. Richardson, S.Dubonos L.Y. Vinnikov, and J. Oboznov. Direct Observation of Vortex Shells and Magic Numbers in Mesoscopic Superconducting Disks. *Phys. Rev. Lett.*, 96:077005, 2006.

[13] T. Nishio, S. Okayasu, J. Suzuki, and K. Kadowaki. Penetration of vortices into microsuperconductors observed with a scanning SQUID microscope. *Physica C*, 379-384:412–414, 2004.

[14] T. Nishio, Q. Chen, W. Gillijns, K. De Keyser, K. Vervaeke, and V. V. Moshchalkov. Scanning Hall probe microscopy of vortex patterns in a superconducting microsquare. *Phys. Rev. B*, 77:012502, 2008.

[15] H. K. Onnes. Investigations into the properties of substances at low temperatures, which have led, amongst other things, to the preparation of liquid helium. *Nobel lecture*, 1913.

[16] W. Meissner and R. Ochsenfeld. A new effect concerning the onset of superconductivity. *Die Naturwissenschaften*, 21:787, 1933.

[17] M. Tinkham. *Introduction to Superconductivity*. McGraw Hall, 1996.

[18] P. F. Dahl. *Superconductivity*. AIP, 1992.

[19] F. London. *Superfluids*. Dover publications, 1950.

[20] L. D. Landau. *Collected papers of L. D. Landau*. Pergamon Press, 1965.

[21] J. Annett. *Superconductivity, Superfluids and Condensates*. Oxford University Press, 2004.

[22] R. P. Huebener. *Magnetic Flux Structures in Superconductors*. Springer, 1979.

[23] C. Kittel. *Introduction to Solid State Physics*. John Wiley and sons, 1996.

[24] A. A. Abrikosov. On the Magnetic Properties of Superconductors of the Second Group. *JETP*, 5(6), 1957.

[25] A. Grigorenko, S. J. Bending, T. Tamegai, S. Ooi, and M. Henini. A one-dimensional chain state of vortex matter. *Nature*, 414:728, 2001.

[26] U. Essmann and H. Trauble. The direct observation of individual flux lines in type II superconductors. *Physics Letters*, 24A:526, 1967.

[27] H. F. Hess, R. B. Robinson, R. C. Dynes, J. M. Valles Jr., and J. V. Waszczak. Scanning-Tunneling-Microscope Observation of the Abrikosov Flux Lattice and the Density of States near and inside a Fluxoid. *Phys. Rev. Lett.*, 62:214–216, 1989.

[28] P. E. Goa, H. Hauglin, M. Baziljevich, E. Il'yashenko, P. L. Gammel, and T. H. Johansen. Real-time magneto-optical imaging of vortices in superconducting $NbSe_2$. *Supercond. Sci. Technol*, 14:729–731, 2001.

[29] A. M. Suvarna C. S. Sunandana. An ESR study of penetration depth in high-T_c Bi-Sr-Ca-Cu-O superconductors. *Solid State Comm.*, 95(1):11, 1995.

[30] M. Nideröst, R. Frassanito, P. Visani, A. C. Mota, and G. Blatter. Temperature dependence of the lower critical field H_{c1} in $Bi_2Sr_2CaCu_2O_{\delta+8}$ single crystals. *Physica C*, 282:1301–1302, 1997.

[31] H. Pan, E. W. Hudson, J. Ma, , and J. C. Davis. Imaging and identification of atomic planes of cleaved $Bi_2Sr_2CaCu_2O_{8+\delta}$ by high resolution scanning tunneling microscopy. *App. Phys. Lett.*, 73(1):58, 1998.

[32] A. E. Koshelev. Crossing Lattices, Vortex Chains, and Angular Dependence of Melting Line in Layered Superconductors. *Phys. Rev. Lett.*, 38:187, 1999.

[33] V. K. Vlasko-Vlasov, A. Koshelev, U. Welp, G. W. Crabtree, and K. Kadowaki. Decoration of Josehpson vortices by pancake vortices in $Bi_2Sr_2CaCu_2O_{\delta+8}$. *Phys. Rev. B*, 66:014523, 2002.

[34] M. Tokunaga, M. Kobayashi, Y. Tokunaga, and T. Tamegai. Visualization of vortex chains in $Bi_2Sr_2CaCu_2O_{8+\delta}$ by magneto-optical imaging. *Phys. Rev. B*, 66:060507(R), 2002.

[35] A. N.Grigorenko, S. J. Bending, I. V. Grigorieva, A. E. Koshelev, T. Tamegai, and S. Ooi. Tilt of Pancake Vortex Stacks in Layered Superconductors in the Crossing Lattice Regime. *Phys. Rev. Lett.*, 94:067001, 2005.

[36] D. A. Huse. Magnetic-flux patterns on the surface of a type-II superconductor. *Phys. Rev. B*, 46:8621, 1992.

[37] C. P. Bean and J. D. Livingston. Surface Barrier in Type II Superconductors. *Phys. Rev. Lett.*, 12(1):14–16, 1964.

[38] L. Burlachkov, V. B. Geshkenbein, A. E. Koshelev, A. I. Larkin, and V. M. Vinokur. Giant flux creep through surface barriers and the irreversibility line in high-temperature superconductors. *Phys. Rev. B*, 50:R16770, 1994.

[39] V. N. Kopylov, A. E. Koshelev, and I. F. Schegolev. The role of surface effects in magnetization of high-T_c superconductors. *Physica C*, 170:291–297, 1990.

[40] E. H. Brandt. Thermal fluctuations of the vortex positions in high-T_c superconductors. *Physica C*, 162:1167–1168, 1989.

[41] L. Landau and E. M. Lifshitz. *Theoretical Physics, Vol.8, Electrodynamics of Continuous Media*. Pergamon Press, 1984.

[42] A. Shadowitz. *The electromagnetic field*. Dover publications, 1975.

[43] E. R. Andrew and J. M. Lock. The Magnetization of Superconducting Plates in Transverse Magnetic Fields. *Proc. Phys. Soc.*, A63:13–25, 1950.

[44] R. Olafsson and J. F. Allen. Field penetration into type I superconducting cylinders. *J. Phys. F: Metal Phys.*, 2:123–132, 1972.

[45] J. Provost, E. Paumier, and A. Fortini. Shape effects of the magnetisation of superconducting lead at 4.2 K. *J. Phys. F: Metal Phys.*, 4:439–448, 1974.

[46] Ali A. Babaei Brojeny and J. R. Clem. Magnetic-field and current-density distributions in thin-film superconducting rings and disks. *Phys. Rev. B*, 68:174514, 2003.

[47] M. Benkraouda and J. R. Clem. Magnetic hysteresis from the geometrical barrier in type-II superconducting strips. *Phys. Rev. B*, 53:5716, 1996.

[48] A. Fortini, A. Hairie, and E. Paumier. Magnetization of a type-I superconducting slab in the thermodynamic and the metastable phases. *Phys. Rev. B*, 21(11):5065, 1980.

[49] A.K. Geim, S.V. Dubonos, J.G.S. Lok, M. Henini, and J.C. Maan. Paramagnetic Meissner effect in small superconductors. *Nature*, 396:144, 1998.

[50] J. J. Palacios. Vortex matter in superconducting mesoscopic disks: Structure, magnetization, and phase transitions. *Phys. Rev. B*, 58:R5948, 1998.

[51] B. J. Baelus, L. R. E. Cabral, and F. M. Peeters. Vortex shells in mesoscopic superconducting disks. *Phys. Rev. B*, 69(6):064506, 2004.

[52] V. R. Misko, B. Xu, and F. M. Peeters. Formation and size dependence of vortex shells in mesoscopic superconducting niobium disks. *Phys. Rev. B*, 76(2):024516, 2007.

[53] M. J. Stephen and J. Bardeen. Theory of the Motion of Vortices in Superconductors. *Phys. Rev.*, 140(4A):1197, 1965.

[54] S. J. Bending. Local magnetic probes of superconductors. *Advance in Physics*, 48(4):449–535, 1998.

[55] E. H. Hall. On a New Action of the Magnet on Electric Currents. *American Journal of Mathematics*, 2(3):287, 1879.

[56] R. F. Broom and E. H. Rhoderick. Studies of the Intermediate State in Thin Superconducting Films. *Proc. Phys. Soc*, 79, 1962.

[57] T. Tamegai, L. Krusin-Elbaum, P. Santhanam, M. J. Brady, W. T. Masselink, C. Feild, and F. Holtzberg. Spatially resolved magnetic hysteresis in a $YBa_2Cu_3O_{7-y}$ crystal measured by a Hall-probe array. *Phys. Rev. B*, 45(5):2589, 1992.

[58] A. C. Gossard R. Dingle, H. L. Störmer and W. Wiegmann. Electron mobilities in modulation-doped semiconductor heterojunction superlattices. *Appl. Phys. Lett.*, 33(7), 1978.

[59] J. S. Neal. *Superconducting and ferromagnetic micro-systems and hybrid structures studied by scanning Hall probe microscopy.* PhD thesis, Department of Physics, University of Bath, 2007.

[60] R. B. Dinner, M. R. Beasley, and K. A. Moler. Cryogenic scanning Hall-probe microscope with centimeter scan range and submicron resolution. *Rev. Sci. Inst.*, 76:103702, 2005.

[61] Michael Faraday. Experimental Researches in Electricity. Nineteenth Series. *Philosophical Transactions of the Royal Society of London*, 136:1–20, 1846.

[62] E. Hecht. *Optics*. Addison Wesley Longman, Inc., 2002.

[63] P. B. Alers. Structure of the Intermediate State in Superconducting Lead. *Phys. Rev.*, 105(1):104–108, 1957.

[64] J. C. Suits and B. E. Argyle. Magnetic Birefringence of EuSe. *Phys. Rev. Lett.*, 14(17):687, 1965.

[65] D. Majer, E. Zeldov, and M. Konczykowski. Separation of the Irreversibility and Melting Lines in $Bi_2Sr_2CaCu_2O_8$ Crystals. *Phys. Rev. Lett.*, 75(6):1166, 1995.

[66] I-Fei Tsu, Jyh-Lih Wang, S. E. Babcock, D. C. Larbalestier A. A. Polyanskii, and K. E. Sickafus. Structure and properties of an intragranular weak link in $Bi_2Sr_2CaCu_2O_{8+x}$. *Physica C*, 8:349, 2001.

[67] G. Yang, J. S. Abell, and C. E. Gough. Magnetic flux penetration and distribution in $Bi_2Sr_2CaCu_2O_y$ single crystals by magneto-optical measurements. *Physica C*, 1091:341–348, 2000.

[68] Y. Fasano, M. Menghini, F. de la Cruz, and G. Nieva. Weak interaction and matching conditions for replicas of vortex lattices. *Phys.Rev. B*, 62:15183, 2000.

[69] M. R. Koblischka, R. J. Wijngaarden, D.G. de Groot, R. Griessen, A.A. Menovsky, and T.W. Li. Study of flux behaviour in $Bi_2Sr_2CaCu_2O_8$ single crystal in external magnetic fields up to 1 T. *Physica C*, 249:339, 1995.

[70] M. Yasugaki, M. Tokunaga, N. Kameda, and T. Tamegai. Magneto-optical imaging of crossing-lattices state in $Bi_2Sr_2CaCu_2O_y$ single crystals. *Phys. Rev. B*, 67:104504, 2003.

[71] M. Li, P. H. Kes, S. F. W. R. Rycroft, C. J. van der Beek, and M. Konczykowski. Origin of linear extended defects in single crystalline $Bi_2Sr_2CaCu_2O_8$. *Physica C*, 408:25, 2004.

[72] J. R. Clem (unpublished).

[73] M. S. James, S. T. Stoddart, S. J. Bending, S. Aukkaravittayapun, P. J. King, and M. Henini. Field penetration and surface barriers in superconducting $Bi_2Sr_2CaCu_2O_{\delta+8}$ whiskers. *Phys. Rev. B*, page R5771, 1997.

[74] M. V. Indenbom, C. J. van der Beek, V. Berseth, T. Wolf, H. Berger, and W. Benoit. Magneto-optical observation of twisted vortices in type II superconductors. *J. Low. Temp. Phys.*, 105:1529, 1996.

[75] J. A. Herbsommer, V. F. Correa, G. Nieva, H. Pastoriza, and J. Luzuriaga. Vortex dynamics in $Bi_2Sr_2CaCu_2O_{\delta+8}$ single crystals with planar defects. *Solid State Comm.*, 59:120, 2001.

[76] A. Oral, J. C. Barnard, S. J. Bending, S. Ooi, H. Taoka, T. Tamegai, and M. Henini. Disorder-driven intermediate state in the lattice melting transition of $Bi_2Sr_2CaCu_2O_{8+\delta}$ single crystals. *Phys. Rev. B*, 56(22):R14295, 1997.

[77] M. Tokunaga, T. Tamegai, Y. Fasano, and F. de la Cruz. Direct observations of the vortex chain state in $Bi_2Sr_2CaCu_2O_{8+\delta}$ by Bitter decoration. *Phys. Rev. B*, 67:134501, 2003.

[78] S. J. Bending, A. N. Grigorenko, I. A. Crisan, A. E. Koshelev D. Cole, J. R. Clem, T. Tamegai, and S. Ooi. Interacting crossing vortex lattices in the presence of quenched disorder. *Physica C*, 412:372, 2004.

[79] A. N. Grigorenko, S.J.Bending, A.E.Koshelev, J.R.Clem, T.Tamegai, and S.Ooi. Interacting crossing vortex lattices in the presence of quenched disorder. *Phys. Rev. Lett*, 89:217003, 2002.

[80] V. Hardy, A.Wahl, S. Hebert, A. Ruyter, J. Provost, D. Groult, and Ch. Simon. Accomodation of vortices to tilted line defects in high-T_c superconductors with various electronic anisotropies. *Phys. Rev. B*, 54:656, 1996.

[81] L. M. Paulius, J. A. Fendrich, W. K. Kwok, A. E. Koshelev, V. M. Vinokur, G. W. Crabtree, and B. G. Glagola. Effects of 1-GeV uranium ion irradiation on vortex pinning in single crystals of the high temperature superconductor $YBa_2Cu_3O_{7-\delta}$. *Phys. Rev. B*, 56:913, 1997.

[82] A. E. Koshelev (unpublished).

[83] M. Yasugaki, K. Itaka, M. Tokunaga, N. Kameda, and T. Tamegai. Magneto-optical characterizations of inhomogeneities in $Bi_2Sr_2CaCu_2O_{8+\delta}$ single crystals grown by floating-zone method. *Phys. Rev. B*, 65:212502, 2002.

[84] A. Kanda, B. J. Baelus, F. M. Peeters, K. Kadowaki, and Y. Ootuka. Experimental Evidence for Giant Vortex States in a Mesoscopic Superconducting Disk. *Phys. Rev. Lett*, 93:257002, 2004.

[85] Mighui Kong, B. Partoens, and F. M. Peeters. Topological defects and nonhomogeneous melting of large two-dimensional Coulomb clusters. *Phys. Rev. E*, 67, 2003.

[86] Y. Hata, J. Suzuki, I. Kakeya, K. Kadowaki, A. Odawara, A. Nagata, S. Nakayama, and K. Chinone. Flux quantization in a superconducting microdisk. *Physica C*, 388:719, 2003.

[87] E. H. Brandt. Irreversible magnetization of pin-free type-II superconductors. *Phys. Rev. B*, 60(17):11939, 1999.

[88] J. Pearl. Current distribution in superconducting films carrying quantized fluxoids. *App. Phys. Lett.*, 5:65, 1964.

[89] Y. Q. Song, W. P. Halperin, L. Tonge, T. J. Marks, M. Ledvij, V. G. Kogan, and L. N. Bulaevskii. Low Temperature Fluctuations of Vortices in Layered Superconductors. *Phys. Rev. Lett.*, 70(20):3127, 1993.

[90] J. E. Sonier, J. H. Brewer, and R. F. Kie. Vortex Fluctuations in Underdoped $Bi_2Sr_2CaCu_2O_{8+\delta}$ Crystals. *Reviews of Modern Physics*, 72:769, 2000.

[91] S. Colson, Y. Matsuda P. Gierlowski M. Li P. H. Kes M. Konczykowski, M. B. Gaifullin, and C. J. van der Beek. Vortex Fluctuations in Underdoped $Bi_2Sr_2CaCu_2O_{8+\delta}$ Crystals. *Phys. Rev. Lett.*, 90(13):137002, 2003.

[92] D. E. Farrell, E. Johnston-Halperin, L. Klein, P. Fournier, A. Kapitulnik, E.M. Forgan, A.I.M. Rae, T.W. Li, M. L. Trawick, R. Sasik, and J.C. Garland. Magnetization jumps and irreversibility in $Bi_2Sr_2CaCu_2O_8$. *Phys. Rev. B*, 53(17):11807, 1996.

[93] A. Soibel, E. Zeldov, M. Rappaport, Y. Myasoedov, T. Tamegai, S. Ooi, M. Konczykowski, and V. B. Geshkenbein. Imaging the vortex-lattice melting process in the presence of disorder. *Nature*, 406:282, 2000.

[94] G. Jung, M. Ocio, Y. Paltiel, H. Shtrikman, and E. Zeldov. Magnetic noise measurements using cross-correlated Hall sensor arrays. *App. Phys. Lett.*, 78(3):359, 2001.

[95] T. S. Lee *et al.* Correlation of Vortex Motion in High-T_c Superconductors. *Phys. Rev. Lett.*, 74(14):2796, 1995.

[96] H. Nyquist. Thermal Agitation of Electric Charge in Conductors. *Physical Review*, 32:110, 1928.

[97] J. B. Johnson. Thermal Agitation of Electricity in Conductors. *Physical Review*, 32:97, 1928.